Setup and commissioning of a test stand for detailed investigations of quantum efficiency characteristics of photomultiplier tubes, and initial studies for IceCube-Gen2

Dem Institut für Kernphysik an der
Westfälischen Wilhelms-Universität Münster
zur Erlangung des Grades Master of Science

vorgelegt von

Raffaela Solveig Busse

März 2017

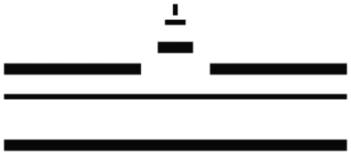

Westfälische
Wilhelms-Universität
Münster

IceCube
GEN2

Themensteller: Prof. Dr. A. Kappes
Korreferent: Prof. Dr. C. Weinheimer

Contents

"There is a way out of every box, a solution to every puzzle. It's just a matter of finding it."

Jean-Luc Picard

1 Introduction

After photons, neutrinos are the second most abundant particles in our universe. Their origins are diverse: From terrestrial sources over atmospheric decays, to solar radiation, supernovae, galactic and even extra-galactic objects. Here on Earth, over seventy billion pass through an area the size of a thumbnail every second.

And yet one can not tell they're even there.

The reason lies in the fact that the most valuable quality of neutrinos is also their biggest flaw. They can travel incredibly large distances directly from their origin to Earth without being influenced or deflected by cosmic dust, magnetic fields or radiation of any kind, which makes them ideal astronomical messengers. Neutrinos can help us to look inside cosmic objects like no other particle could. This awards them an inestimable value for astronomy.

But, on the other hand, this quality obviously makes them hard to catch - and all the precious information they may carry with them.

Yet with large-volume detectors around the world, researchers managed to actually measure neutrinos, even galactic and extra-galactic ones. The IceCube [1] experiment with its $1\,\mathrm{km}^3$ detector volume and over 5000 optical sensors deep in the antarctic icecap is currently by far the biggest of these experiments. But due to a lack of statistics, even IceCube has not been able to achieve one of the major goals of neutrino astronomy: To locate the sources of these neutrinos.

This provides the motivation for a 'next-generation'-IceCube: The future project IceCube-Gen2 [2], which includes an up to ten-times larger instrumented volume and more sensitive optical sensors, is supposed to put neutrino astronomy to the next level by finding point sources of high energy neutrinos.

The IceCube group in Münster is working on an upgraded optical sensor for IceCube-Gen2: The Multi-PMT digital optical module, or short mDOM [3, 4]. The mDOM includes 24 photomultiplier tubes (PMTs) which will be the 'eyes' of the detector: They are capable of detecting even the smallest amounts of light the neutrinos produce in the ice. That means having a full understanding of the PMTs and their optical and physical properties is crucial for the mDOM project and thus for the whole IceCube-Gen2 experiment. This thesis contributes to the understanding of these highly sensitive devices by developing a test stand to investigate the PMT's optical properties with a focus on quantum efficiency. The detailed description of the test stand design, setup, and commissioning, as well as initial quantum efficiency measurements, is the content of this thesis.

2 Neutrinos

This chapter will give an introduction to neutrinos, their historical background in research, their place in the Standard Model of particle physics and a description of the ways they interact with matter. More information on these topics can be found in [5], which the explanations in this chapter are based upon.

2.1 Fundamentals and historical background

All matter - the one that we can see and feel, but also the one that is concealed from our direct perception - is composed of elementary particles, which are specified in the Standard Model of particle physics. The quarks, drawn in purple in figure 2.1, are the building blocks of neutrons and protons. Together with electrons, these form the elements we and our surroundings are made of. Electrons belong to the family of leptons (green in the picture), which they share with muons and taus. These three leptons are electrically charged, but they each have a neutral counterpart - the neutrinos. The neutrinos come in three different so-called flavours which are named after their corresponding counterpart in the lepton-family: The electron neutrino ν_e, the muon neutrino ν_μ and the tau neutrino ν_τ. For every quark and lepton there is an antiparticle of identical mass but with opposite electrical charge.

There is another group of particles in the Standard Model, the gauge bosons. These are the force carriers of the four fundamental interactions that 'keep everything together': The

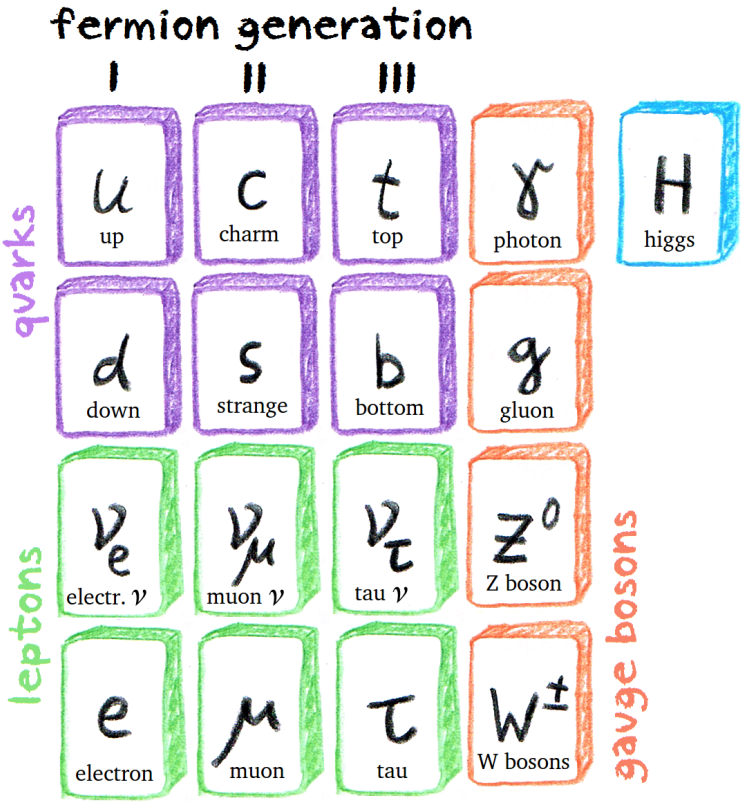

Figure 2.1: The Standard Model of particle physics with all elementary particles that form matter (fermion generations), the gauge bosons of the four fundamental interactions and the Higgs boson.

massless photon for the electromagnetic force, the massless gluons (there are eight of them) for the strong force and the massive Z^0 and $W^{\pm}$ bosons for the weak force. The also massive Higgs boson, which is associated with the mass of other elementary particles via the Higgs mechanism, is drawn in blue.[1]

Let us have a closer look at neutrinos. They were postulated in 1930 by Wolfgang Pauli[2] after physicists had been puzzled by the continuous spectrum of the beta minus decay, which meant that there had to be a third, so far unknown, very light (or massless) neutral particle that took away some energy from the otherwise discrete spectrum. These particles were named neutrinos. According to the Standard Model, the neutrinos are massless. However, nowadays the scientific consensus considers them massive, though the exact masses are yet unknown. The Nobel Prize in physics was recently awarded to Takaaki Kajita and Arthur B. McDonald for the discovery of neutrino oscillation, which proves that the neutrinos are massive [8]. One attempt to measure the actual neutrino mass of the $\bar{\nu}_e$ is the KATRIN experiment in Karlsruhe [9]. Its model-independent measurement technique investigates the very end point of the above mentioned beta minus decay spectrum to determine or further improve the limit of the neutrino mass.

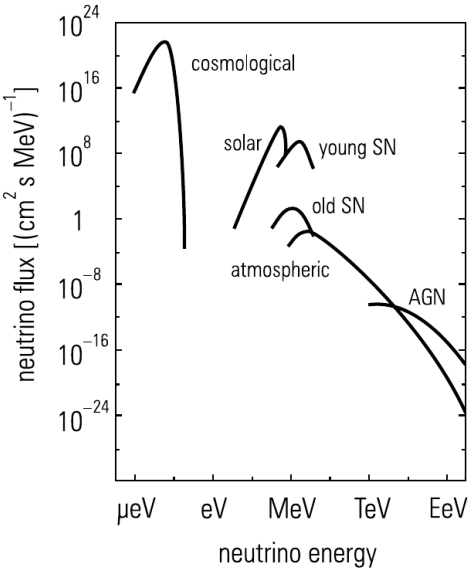

Figure 2.2: Neutrino fluxes originating from the cosmological background radiation, the sun, super novae (SN), the Earth atmosphere and active galactic nuclei (AGN) for different neutrino energies [5] (p. 104).

2.2 Neutrino interaction and detection principle

Cosmic neutrinos are produced in a variety of different sources and processes, so they come with very different energies. An overview of the neutrino fluxes for different energies is given by figure 2.2. Supernovae occasionally bombard the Earth with neutrinos, the nucleosynthesis reactions in the Sun are responsible for the solar neutrino flux, and cosmic particles that hit the atmosphere generate particle showers which produce atmospheric neutrinos, and still others can be found in the cosmological background radiation. The neutrinos with by far the highest energy, however, are produced by special galactic and extra-galactic sources.

These latter neutrinos are the objects of interest for high-energy neutrino astronomy. Their sources can be objects like super massive black holes or active galactic centres, which thrust extremely powerful cosmic jets into the space around them. Inside these jets, the high-energy neutrinos are generated in particle acceleration processes illustrated in figure 2.3.

Charged particles like protons or electrons generated in such objects are deflected by cosmic magnetic fields, so they can not be traced back to their origins once they reached Earth, which disqualifies them as tools to find their sources. So photons are the obvious choice for finding them - but they can be absorbed or scattered in interstellar media. They can not provide information about the inside of their source and their generating process is

[1] The theoretical discovery of the Higgs boson was awarded the Nobel Prize in physics in 2013 [6].
[2] Not published until 1934 [7].

not unambiguous, since they can be produced in leptonic *and* hadronic acceleration [10]. The neutrinos, however, are ideal astronomical messengers: Carrying no charge, they hardly interact with matter, and are not influenced by magnetic fields, cosmic dust or radiation of any kind, that could distract them from their course. They are pervasive enough to allow us to 'look inside' the astronomical objects they originate from. Furthermore, they are 'smoking guns' for hadronic accelerations as the only processes capable of producing such neutrinos [11]. This is the reason for their present-day astrophysical significance. [5, 10]

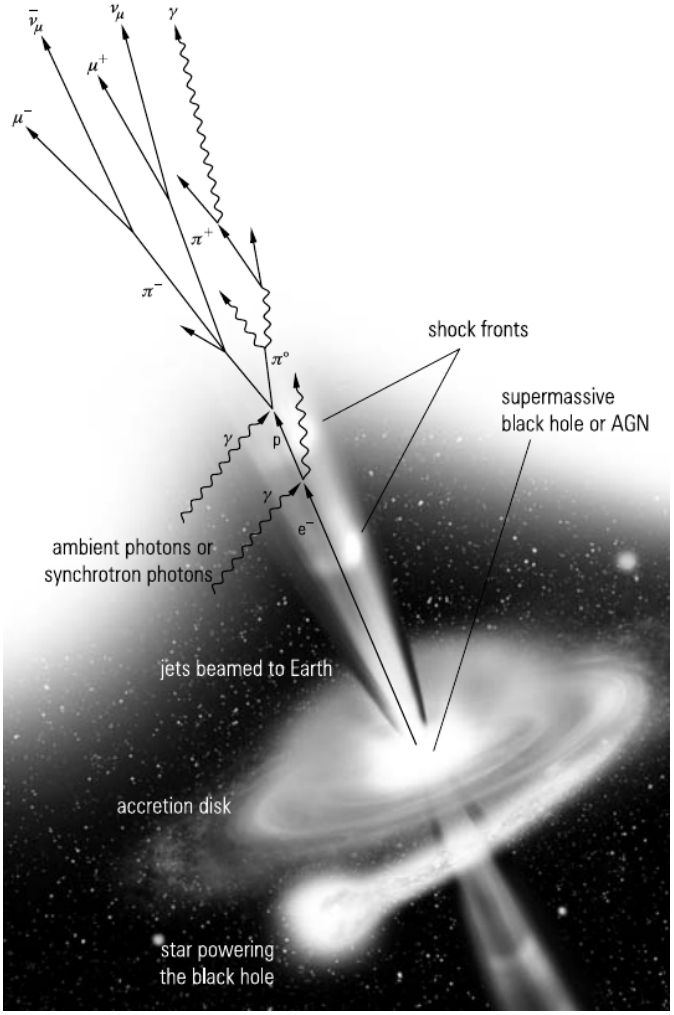

Figure 2.3: Neutrino generation in cosmic jets, thrust from astronomical objects like supermassive black holes or active galactic nuclei (AGN) [5] (p. 74).

This unfortunately also means that neutrinos are very hard to measure. Although the cross section of a neutrino interacting with matter increases with neutrino energy [11], the neutrino flux decreases, as can be seen in figure 2.2. This is why high-energy neutrino astronomy needs huge detector volumes.

So how are neutrinos measured after all? As mentioned before, they carry neither electrical nor colour charge, which means they can only interact gravitationally or weakly. Since gravitation can be neglected as the weakest of all the forces, the only way to 'find' a neutrino is if it produces charged secondary particles in weak interaction channels. The gauge bosons of the weak interaction are the W^+, the W^- and the Z^0 bosons. As the superscripts indicate, the W bosons are electrically charged and the Z boson is neutral. Therefore the weak interactions are distinguished as charged current (CC) or neutral current (NC) interactions, respectively.

The neutrinos of interest for high-energy neutrino astronomy usually have energies from some GeV to several PeV. In this energy ranges, the main interaction channel for neutrinos with matter is deep inelastic scattering with nucleons. It can occur in a charged or neutral current interaction [10]:

$$\nu_l + N \to \nu_l + X \quad \text{(NC)}, \qquad \nu_l + N \to l + X \quad \text{(CC)} \tag{2.1}$$

where the ν_l represents a neutrino (or anti-neutrino) with flavour l. N can be a proton or neutron. On the right-hand side of the reaction stands either a neutrino (or anti-neutrino) with the same flavour (NC) or the corresponding charged lepton (CC) plus X, which can be several hadronic particles or even a hadronic cascade. Examples for the reactions in (2.1) are shown in figure 2.4.

Neutrinos can not be measured directly. What *can* be measured, however, are the secondary leptons produced either directly in CC reactions or indirectly in NC reactions due to hadronic showers.

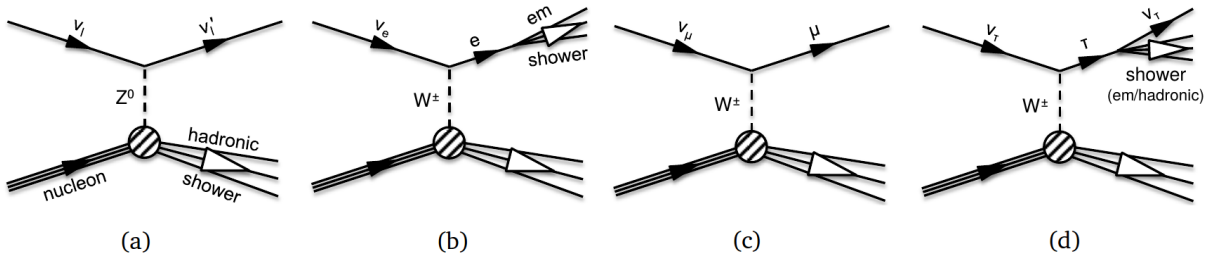

Figure 2.4: Schematic diagrams of reactions describing deep inelastic scattering of high-energy neutrinos with nucleons. (a) shows an NC reaction where a neutrino of flavour l scatters off a nucleon exchanging a Z^0 boson. (b) - (d) show CC reactions for the flavours e, μ and τ separately. In all three CC reactions the exchanged charged $W^{\pm}$ boson causes a transformation of the scattered neutrino into its corresponding lepton. All reactions are valid for the respective anti-neutrinos. Taken from [10] and modified.

These charged particles are measurable due to the **Cherenkov effect**[3]**,** which is explained in the following:

In a vacuum, no particle can move faster than light. In a medium with a refractive index of n however, a particle's velocity v can in fact exceed the light velocity c_n inside the material (where c is the speed of light in vacuum) [5] (p. 56):

$$v \geq c_n = \frac{c}{n}$$

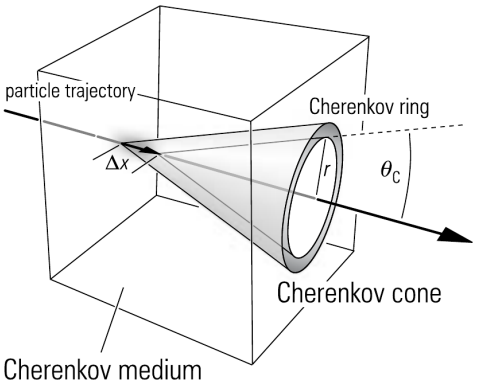

Figure 2.5: Cherenkov cone along the trajectory of a fast moving charged particle in a medium [5] (p. 56).

If this is the case for a charged particle, it emits Cherenkov radiation. To be exact, it is not the particle itself that generates the radiation but the induced electric dipole that is moving along with it: Every charged particle that moves through a medium polarises the surrounding material. This polarisation is usually symmetric, so that the radiation emitted by the resulting moving dipole disappears in destructive interference. If however, the polarisation is not fast enough to 'follow' the fast particle anymore, it is asymmetric and the radiation becomes measurable. The Cherenkov radiation is emitted in the direction of travel with an angle of

$$\phi_c = \arccos\left(\frac{1}{n\beta}\right),$$

with $\beta = v/c$. This angle is about 1.4° in air [5] (p. 55) and about 40° in ice (for a refractive index $n_{ice} = 1.3$ [13] (p. E-377) and $\beta \approx 1$). The relativistic charged particle therefore generates a so-called Cherenkov cone (which can be roughly compared to a Mach cone), that results in a Cherenkov ring in the detector plane, see figure 2.5. Since the produced photons move relative to the particle trajectory, the original particle direction or the location of the particle source can be reconstructed measuring the Cherenkov light.

[3] Discovered by the then PhD student P. A. Cherenkov in 1934 [12].

3 The IceCube and IceCube-Gen2 neutrino telescopes

The IceCube experiment [1] is a neutrino telescope at the Amundsen-Scott South Pole Station. With its 1 km^3 instrumented detector volume, it is currently the largest neutrino detector on Earth. As you can see in figure 3.2, the detector consists of over 86 stings that are almost 2500 m long, with a total of over 5000 optical sensors (digital optical modules, short DOMs) attached. All the strings together form the IceCube Array. The instrumented volume is located about 1500 m beneath the surface.

The purpose of the IceCube Array is the detection of high-energy neutrinos. Although IceCube is not designed as an high-energy detector exclusively: The sub-experiment DeepCore consists of 8 strings with a DOM- and string spacing optimised to detect neutrinos of lower energy. A further sub-experiment of IceCube is the IceTop experiment located at the surface, consisting of 81 ice tanks designed for detecting high-energy events while simultaneously functioning as a veto system against atmospheric muons [14, 15, 10].

The Cherenkov light coming from the interaction of a neutrino with the ice in the detector is measured with the DOMs; one of them is shown in figure 3.3. Each module consists of a glass pressure sphere with 13 inch in diameter. Inside each sphere the 'heart' of the module is placed: The 10 inch PMT, caged inside a shielding against magnetic fields. The upper half of the sphere is taken up by the PMT electronics. The metal harness and three steel cables attaches the module to the string, featuring a vertical inter-DOM spacing of 17 m.

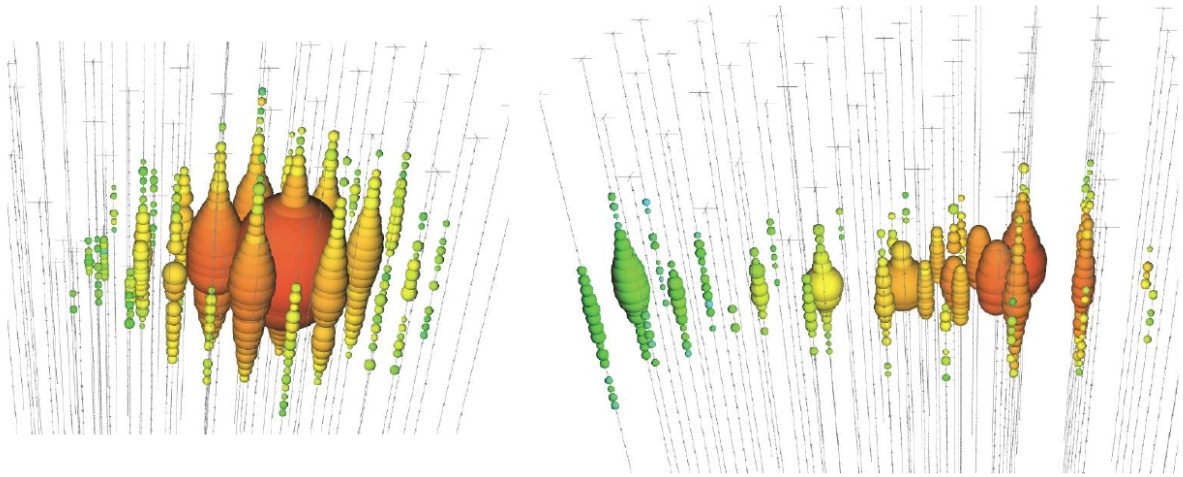

Figure 3.1: Energy deposition signatures caused by (anti-)electron neutrinos (left) and by (anti-) muon neutrinos (right) in the IceCube detector. The DOMs are drawn as dots, where the size is proportional to the amount of detected light. The colour code stands for time of detection (red: early detection, blue: later detection). Pictures courtesy of the IceCube collaboration.

The different leptons generated in the neutrino reactions described in section 2.2 produce different characteristic signals in the detector, which allows for the identification of the neutrino flavour. Electron or anti-electron neutrinos following the reaction shown in figure 2.4 (b) induce shower signatures due to high interaction cross sections of the electron or positron, where the energy is deposited almost at once resulting in a spherical signal[4]. Muon neutrinos, on the other hand, travel long distances through the detector emitting Cherenkov

[4]The hadronic debris produced in the deep inelastic scattering reactions in figure 2.4 can also induce shower-like signatures.

light, which results in a track signature, ideal for direction-reconstruction of the responsible muon neutrino. Examples of these two characteristic signatures are shown in figure 3.1. For more information see reference [10].

Finding point sources of high-energy neutrinos is the major goal of neutrino telescopes. So far no experiment has achieved this. Figure 3.4 shows what IceCube has measured within four years, where the number of events are plotted against the neutrino energy. The measured high-energy neutrino events to the right of the plot lie beyond any energy the atmospheric background would cover, which is indicated by coloured and shaded areas. This diffuse high-energy flux proves the existence of the powerful galactic and extra-galactic sources, but is not sufficient to locate them.

A 'next-generation' IceCube is hoped to fulfil this purpose: The IceCube-Gen2 neutrino telescope [2]. It will be build around the current IceCube detector, including a new high-energy array up to 10 times the volume of the IceCube Array, as well as further low energy extensions. A picture of a possible configuration of the IceCube-Gen2 experiment is shown in figure 3.5.

Additional to the upgrade in terms of size, IceCube-Gen2 will also be equipped with more sophisticated detector modules. The new high-energy array will contain about 15000 new optical sensors that outclass the IceCube DOMs in many ways. Several approaches for such new modules have been made so far, and it is not decided yet which will be implemented in IceCube-Gen2. A promising candidate, however, is the Multi-PMT Digital Optical Module that the Münster IceCube group is working on, in cooperation with other institutes. This new sensor module is described in the next chapter [4].

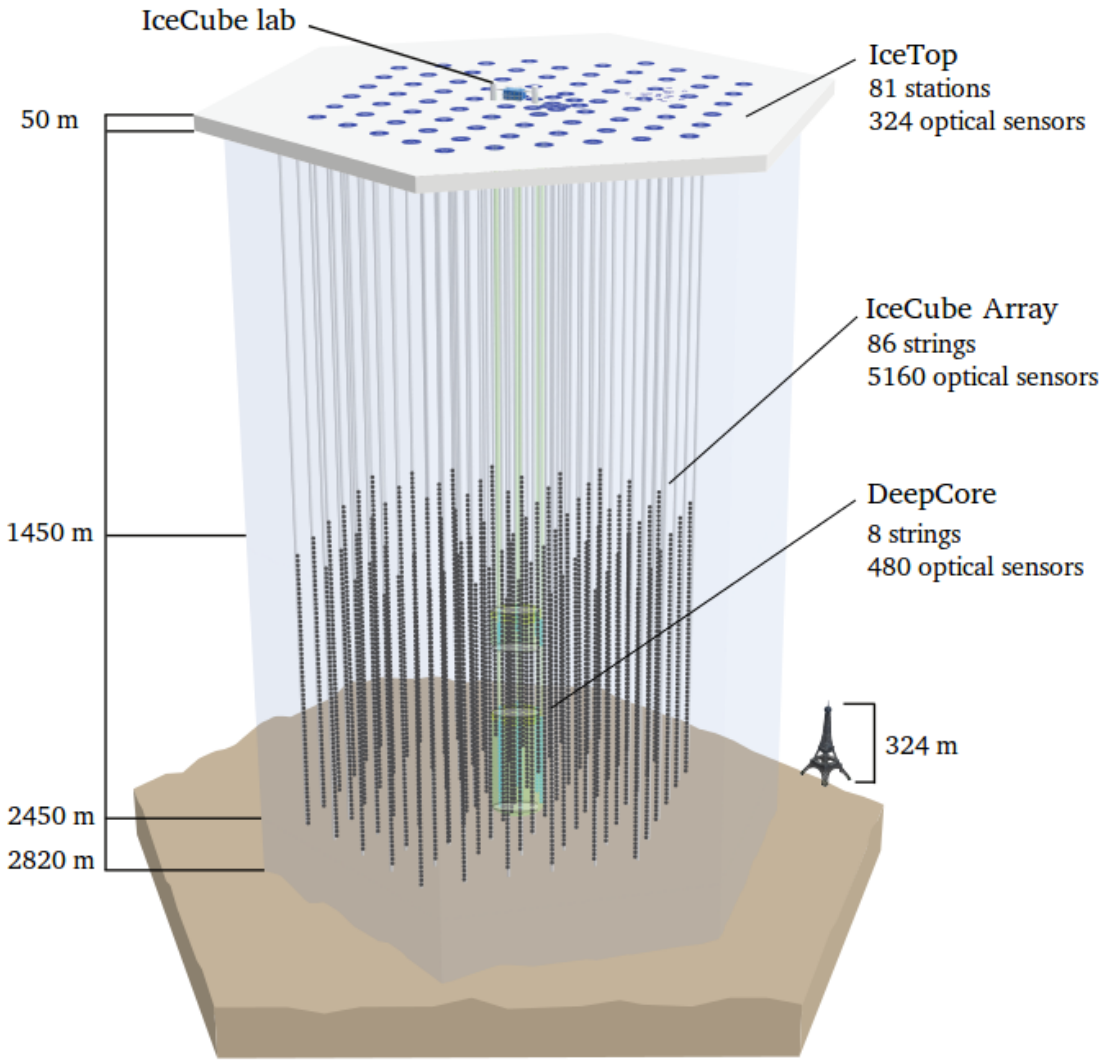

Figure 3.2: Rendered image of the IceCube experiment. The 1 km^3 of instrumented detector volume include the high-energy IceCube Array, the low-energy extension DeepCore (green) and IceTop on the surface. A total of over 5000 optical sensors (shown below) at 86 strings are deployed in the detector. Picture courtesy of the IceCube collaboration (modified).

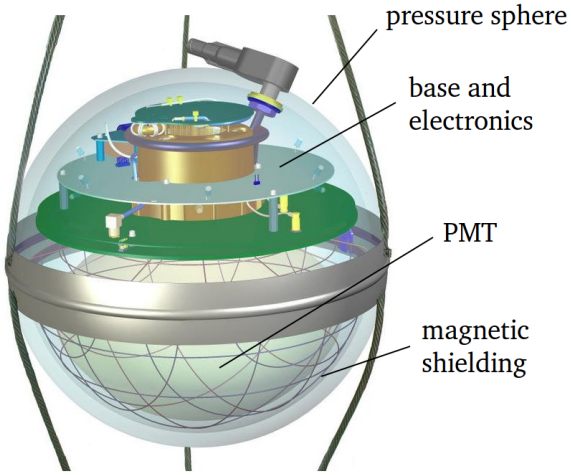

Figure 3.3: Rendered image of The IceCube DOM. It consists of a glass pressure sphere with a 10 inch PMT in the lower half. The upper half contains readout electronics. Steel cables attach the module to the string. Picture courtesy of the IceCube collaboration (modified).

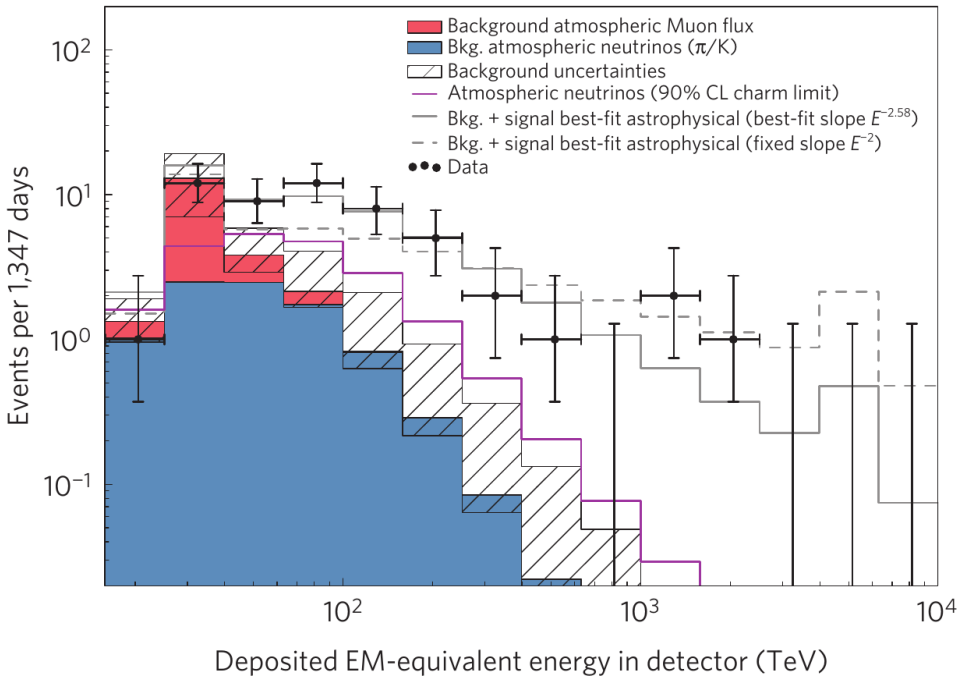

Figure 3.4: Four years of IceCube data. The number of measured events is plotted against their energies. High-energy events are to the right of the plot. The grey and dashed-grey lines indicate two different fits to the data. [16]

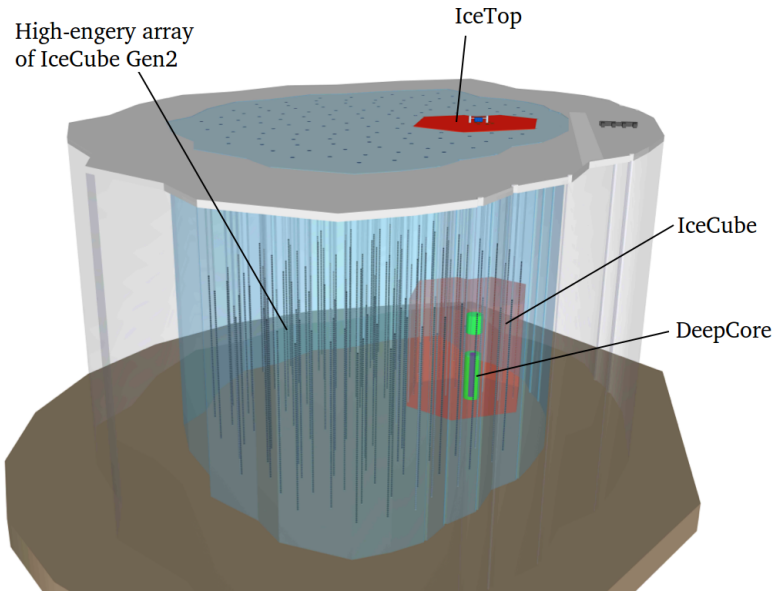

Figure 3.5: Rendered image of a possible configuration of the IceCube-Gen2 experiment. It will cover the IceCube Array (red), the DeepCore extension (green) as well as IceTop (red) with its ten-times bigger detector volume. Picture courtesy of the IceCube collaboration (modified).

4 The Multi-PMT digital optical module

In contrast to the original IceCube DOM which is shown in figure 3.3, the Multi-PMT DOM or short mDOM contains not only one but 24 PMTs, as can be seen in figure 4.2 [3, 4].

The glass pressure sphere with 14 inch in diameter is slightly larger than the IceCube DOM. The 24 PMTs are mounted in a 3D-printed plastic holding structure where a reflective cone is attached around each PMT to increase the photosensitive area of the module. An optical gel between the holding structure and the glass sphere reduces the refractive index difference, acting as an optical bridge to prevent total reflection. The PMT bases and electronics are located on the equatorial plain and in the centre, beneath the PMTs. As you can see in figure 4.2, very little space is left for wiring and other electronics, so all parts of the module have to be coordinated with each other very carefully. To gain some vertical space, the pressure sphere of the mDOM is therefore not completely spherical but slightly cylindrical. Making the mDOM a little wider in radius is not possible, because drilling wider holes in the ice would involve an extreme increase of costs.

The mDOM outclasses single-PMT DOMs in two major aspects. One of these aspects is the effective area, which is defined in [10] and can be interpreted as the equivalent geometric area of the device assuming 100 % efficiency. For up-going light (the bottom of the module is illuminated), the original IceCube DOM or the PDOM[5] have a high effective area since this is the direction the PMT is facing. For different illumination angles though, the effective area rapidly decreases, towards almost zero for down-going light. The new mDOM on the other hand has a homogeneous effective area for all incident angles, due to its 24 PMTs that are facing all directions. Reflective cones around all PMTs further increase the mDOM's effective area. Figure 4.1 shows a visualisation of the effective area of the mDOM and the PDOM. For a detailed investigation see [10].

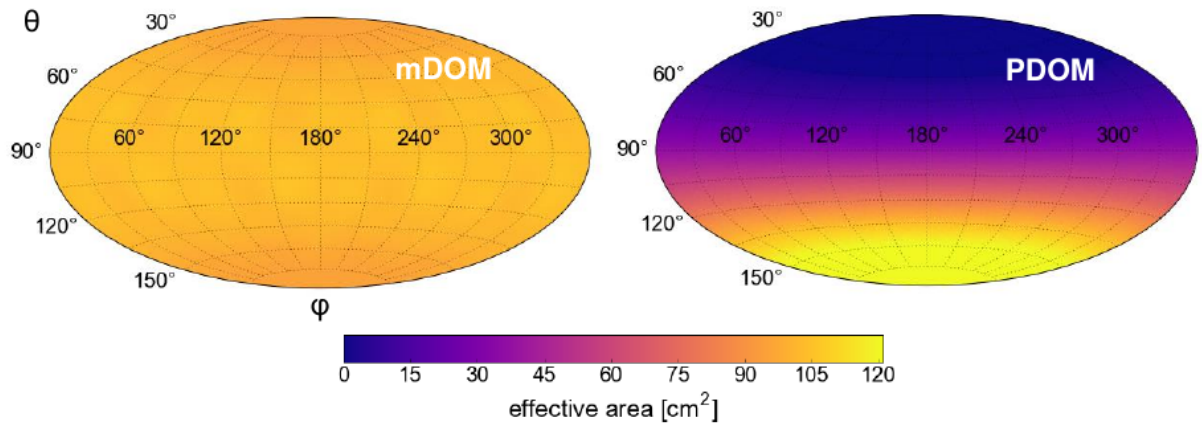

Figure 4.1: The effective area of the mDOM vs the PDOM [10].

The other aspect where the mDOM is superior to the single-PMT DOMs is in terms of directional information. When the mDOM is hit by light, it is most likely that not only one but several of its PMTs detect photons. By analysing the signals in terms of time and amplitude, the direction from which the light most probably came can be determined, with just one detector module. The Multi-PMT design theoretically allows for a rough directional recon-

[5] The PDOM is another IceCube-Gen2 optical sensor candidate which is very similar in design to the IceCube DOM, featuring one single 10 inch-PMT looking downwards [17].

struction of even single photons. With single-PMT modules, the precision of any directional information is limited to the large field of view of the PMT.

Being the detector's 'eyes', it is important for the IceCube-Gen2 experiment to have a complete understanding of its optical sensors. Therefore an in-depth study of the PMTs is crucial. The next chapter will give a detailed introduction to PMTs and their features and properties.

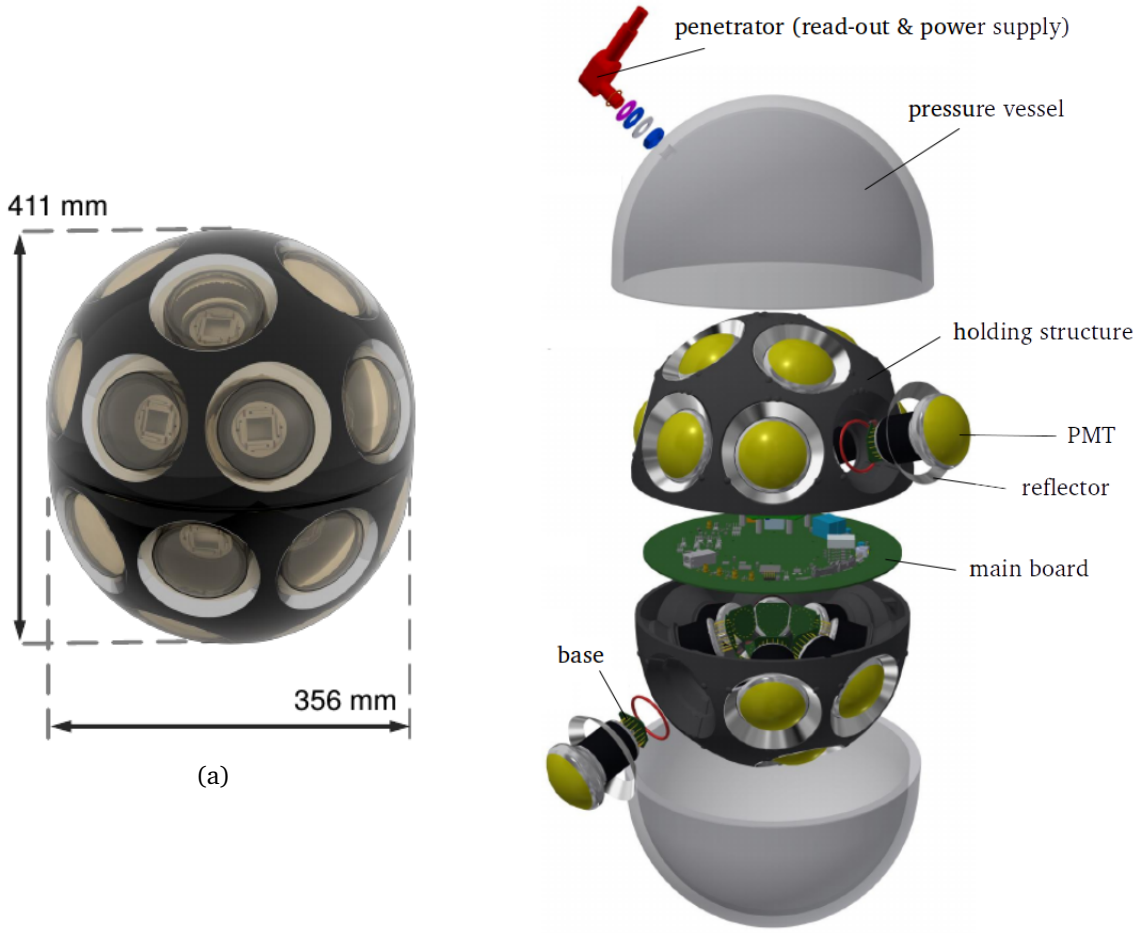

(a) (b)

Figure 4.2: **(a)** Rendered image of the mDOM with 24 PMTs inside an almost-spherical pressure vessel. **(b)** Exploded view of the mDOM. The PMTs are mounted in a plastic holding structure. All electronics is located on the main board and beneath the PMTs. The reflectors are for increasing the effective area (explanation in the text). Pictures courtesy of the Münster IceCube group.

5 Photomultiplier tubes

This chapter provides an overview over the most important PMT components and their functionalities, based upon references [18, 19]

5.1 Setup and operating principle

In principle, one may think of a PMT as a light bulb shaped device[6] that collects light and transforms and amplifies it into a measurable electrical signal. The essentials of a PMT are the photocathode which transforms light into electrons, a structure of staggered electrodes called dynode system, and the anode where the signal is picked up; all housed inside an evacuated glass tube. Figure 5.1 shows a scheme and a photograph of a PMT that will be used in the mDOM. The components mentioned in the picture will be explained in the following.

For this work, the most important PMT component is the photocathode. It is located on

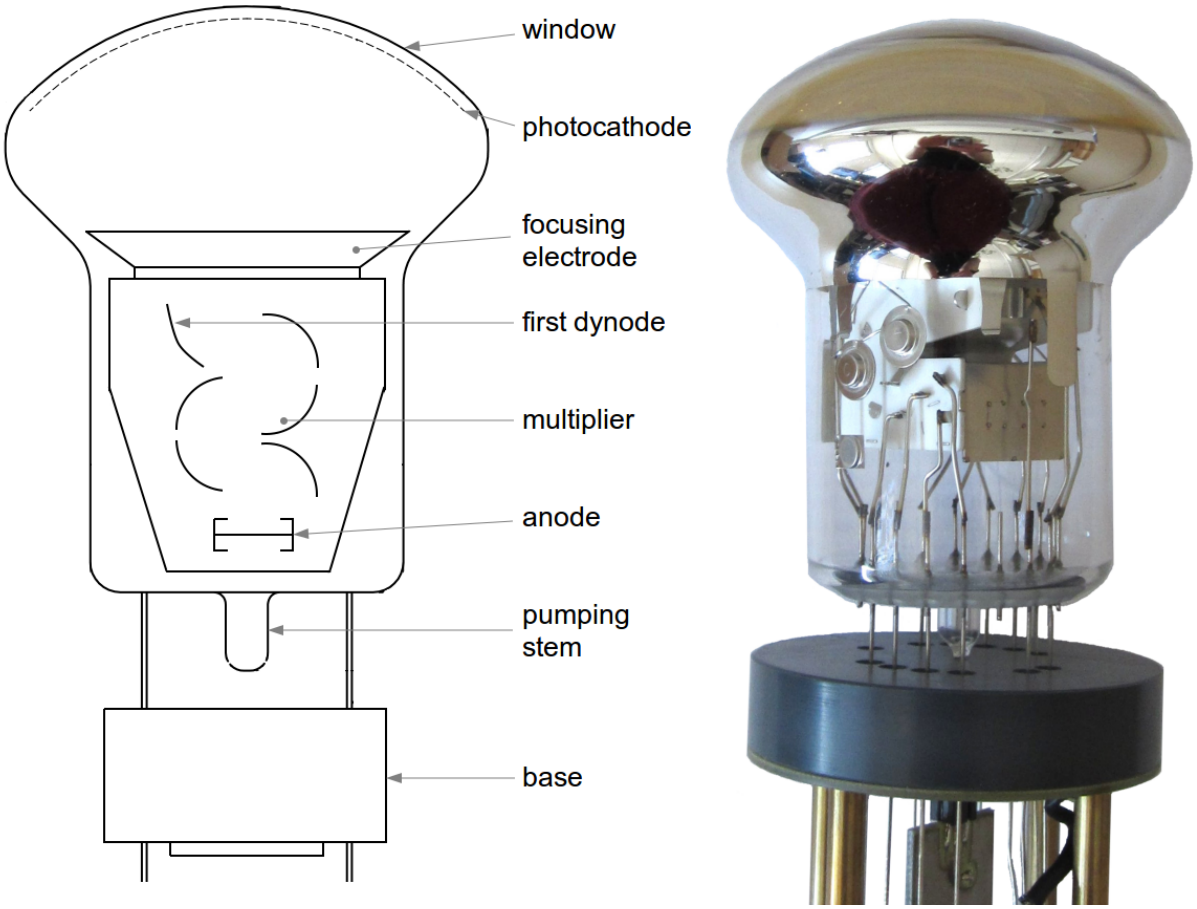

Figure 5.1: Scheme and photograph of a photomultiplier tube from Hamamatsu, model R12199-02, that is used in our experiments. The inner structures of the PMT are enlarged and modified in the scheme for better visibility. An accurate technical drawing of the Hamamatsu R12199-02 can be found in section 8.4.

[6] There is a great variety in shape and size of PMTs actually, but in further sections it will be focused on the type used in our experiments.

the inside surface of the glass window at the very top of the tube. The window material limits the wavelength range of the PMT on the ultraviolet site of the spectrum. Here, it is borosilicate glass with a cutoff-wavelength at about 300 nm. Figure 5.2 gives an overview of the spectral transmittance of different window glass materials. A photon that enters through the window can be reflected, transmitted or absorbed in the window or photocathode. If it is absorbed in the latter, it deposits its energy in the cathode material and releases a primary electron due to photo-emission. The cathode material limits the wavelength range of the PMT on the red site of the spectrum. For the blue-sensitive standard bialkali (KCsSb) photocathode in the PMTs used in our experiments, this limit is at about 700 nm, as is investigated in section 8.2. The optical properties of the glass window and the photocathode as well as its quantum efficiency as a main characteristic are discussed in detail in chapter 6.

Photoelectrons from the photocathode get accelerated towards the focusing electrode and first dynode. The purpose of the electrode is to shape the electric field so that all primary photocathode electrons are focused onto the first dynode, independent of their starting point and velocity.

From here, the primary electron(s) reach the multiplier system. The multiplier consists of several staggered electrodes - the dynodes. They can be arranged in several different ways. The PMTs used in our experiments have a combination of the *box-and-grid* and *linear* dynode configuration. For detailed information on multiplier geometries see reference [19]. The photocathode, the focusing electrode and the anode as well as the dynodes are supplied by a voltage divider. Between the cathode and the anode an acceleration voltage is applied, which is divided in the multiplier system so that from one dynode to the next there is a respective potential increase that accelerates the electrons onto the following dynode, as visualised in figure 5.3. As the name implies, the multiplier does not only accelerate the electrons, it also multiplies them. Each dynode both 'collects' and 'produces' electrons: When the primary electron hits the first dynode, it releases several secondary electrons due to secondary emission whose number depends on the initial energy of the primary electron. This goes on for each dynode in the system.

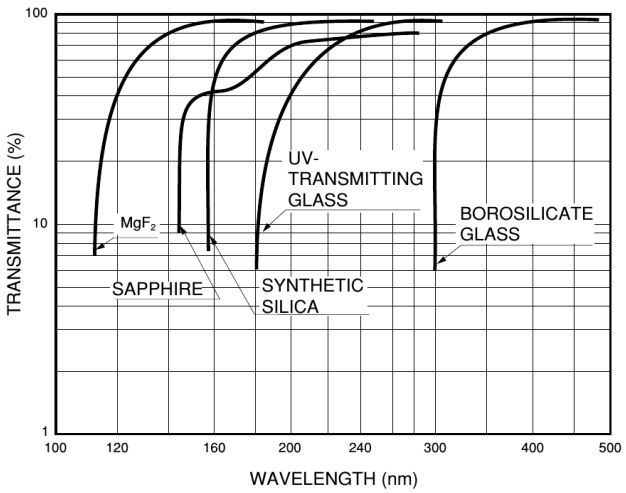

Figure 5.2: Different window glass materials and their spectral transmittance. Taken from [18] (p. 37).

The electrical signal of the electrons that reaches the anode, can be read out with the base of the PMT. The design of the base determines whether this signal is a voltage pulse or a photocurrent (see next section). The signal amplitude is proportional to the light intensity of the incident light.

5.2 Operation modes

As mentioned in the last section, the charge in form of electrons that arrives at the PMT anode can be read out either as a current or as a voltage signal. Therefore PMTs have two operation modes called the current mode and the pulse mode.

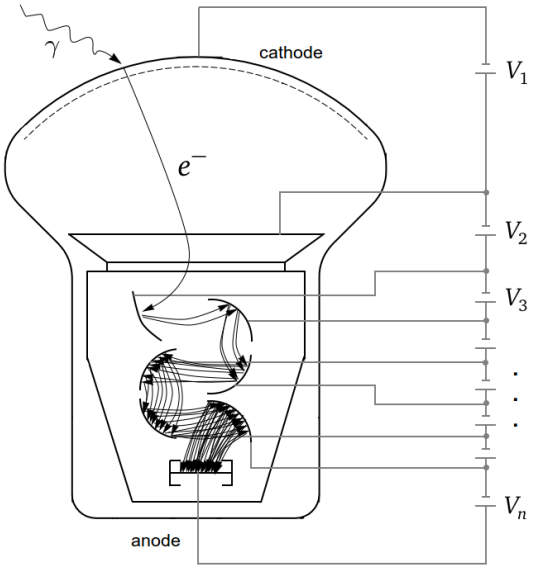

Figure 5.3: Scheme of the dynode system and voltage dividing in a PMT. A primary electron is released from the photocathode (top), is focused to the first dynode by the focusing electrode and produces secondary electrons. Each secondary electron is multiplied due to secondary emission as it travels from dynode to dynode, where the voltage divider supplies an acceleration potential (V_1, V_2, ..., V_n) between each two dynodes. The secondary electrons then finally reach the anode (bottom), where the electric signal can be measured.

When operated in current mode, the charge that reaches the anode is measured by an ampere meter. This is done by integrating over all charge signals that arrive within a certain time window, which results in a current value. This mode is useful for very high-frequency signals or when knowledge about the single pulses is not necessary, as in the case of quantum efficiency measurements.

In pulse mode, the charge is measured by an oscilloscope, where it is applied to an internal resistor which results in a voltage value. This mode is used for analysing single pulses, for counting single photons or when a very low-frequency signal is expected.

These above described methods are for measurements with single PMT in test environments; for PMTs installed in the actual mDOM, the data acquisition is more complex.

5.3 Gain and collection efficiency

The multiplier system provides a well-defined gain to the photocurrent. This gain can be expressed by the product of the coefficient of secondary emission δ of the dynodes, which depends on the dynode material, and the collection efficiency κ of the interdynode spaces, which is affected by the multiplier geometry [19] (p. 1-12, adjusted in terminology):

$$G = \prod_{i=1}^{N} \delta_i \kappa_i$$

Where N is the total number of dynodes in the multiplier. The collection efficiency is a characteristic of the first dynode (in combination with a potential focusing electrode) and each interdynode space in the multiplier system, and is defined by the ratio of the total number of electrons and the number of electrons that are collected. For the focusing electrode that would be the ratio of the number of primary electrons released at the photocathode and the electrons that reach the first dynode; for an interdynode space between the two dynodes d_{i-1} and d_i in the multiplier system that is the ratio of the number of electrons that are released at d_{i-1} and the ones that reach d_i.

5.4 Dark current

Every PMT has a certain signal output even in absolute darkness. This signal is called dark current (when operating in current mode) or dark rate (when operating in pulse mode). It contains discrete as well as continuous parts. A continuous contribution is caused by the so-called leakage current which is an ohmic charge flow at the anode or the pins. Discrete contributions come from thermic or field emission of electrons inside the PMT, or from

radioactive decays inside the glass tube. For other dark current related phenomena and a detailed description see reference [10].

The dark current or rate further depends on a number of environmental factors like temperature, humidity and dust, but also light exposure of the PMT prior to the measurement. The latter component decreases with time, so it is necessary to let the PMT 'settle' in a dark environment before conducting a measurement. For quantum efficiency measurements, it is sufficient to assume the other dark current components to be relatively constant since these factors do not change significantly within measurement time. That means the dark current can be seen as a constant background that simply has to be subtracted from the signal.

6 Quantum efficiency of photomultiplier tubes

Not every photon that hits the PMT necessarily produces a photoelectron that may lead to a measurable PMT signal. The ratio of the number of electrons emitted from the photocathode n_e to the number of incident photons n_i is termed quantum efficiency or short QE:

$$QE = \frac{n_e}{n_i}$$

This ratio is influenced by several factors, like

- the composition of the photocathode material,
- the photocathode thickness,
- the shape and optical features of the glass window,
- and even the inner structures of the PMT, which are not directly connected to the PMT front but contribute via light back-reflection.[7]

To get a deeper understanding of the QE, it is useful to determine the degree of contribution of each individual component of the list above. The theoretical investigation to this approach can be found in section 6.2.

So set aside the possibility that the photon gets reflected or absorbed in the glass window, but reaches the photocathode. Here, three processes have to occur in order to convert the incident photon into a photoelectron:

- **Absorption** of the photon in the photocathode where it produces an electron,
- **diffusion** of the electron through the material, where it looses energy,
- **emission** of the electron from the photocathode surface, which is only possible if the electron has enough surplus energy left to escape. [10]

These three processes are visualised in figure 6.1.

The QE is affected by the wavelength and therefore is usually defined for monochromatic light. For PMTs with a standard bialkali KCsSb photocathode used in our experiments, the quantum efficiency for central illumination with normal incidence usually lies around 25 % for the peak wavelength of about 390 nm. It further depends on properties of the photocathode, like thickness and material. Therefore it may be useful to express the QE in terms of the three processes listed above[20]:

$$QE(\lambda, \theta) = A(\lambda, \theta) \cdot P_{\text{conv}}(\lambda) \tag{6.1}$$

The coefficient $A(\lambda, \theta)$ is termed the absorption coefficient of the photocathode and represents the first process. It depends on the wavelengths and incident angle of the light. $P_{\text{conv}}(\lambda)$ is the conversion coefficient and includes the second and third process; its wavelength dependence issues from different surplus electron energies that may or may not be sufficient for escaping the photocathode.

The focus of the initial measurements in this thesis are the wavelength-, angular- and position dependence of the QE.

[7] Note that for the QE it does not matter whether an electron that escapes the photocathode actually leads to an avalanche in the multiplier system or gets 'lost' on its way. These cases are covered by the collection efficiency, see section 5.3.

6.1 Measurement principle

The photocathode is evaporated to the inside of the glass window of the PMT. It would vaporise instantly as soon as the vacuum inside the PMT is damaged, so it is not possible to access the photocathode material directly. This makes it a lot more complicated to examine features like thickness, uniformity or quantum efficiency.

The only way to examine the photocathode features is with light. In terms of the QE, this is done by illuminating the photocathode through the glass window with a narrow and stable beam of light. The output photocurrent of the PMT can then be compared to the current the light produces in a reference device like a calibrated photodiode (PHD). The ratio of the PMT current I_{PMT} and the PHD current I_{PHD}, subtracted with the respective dark currents $I_{\mathrm{dark,PMT}}$ and $I_{\mathrm{dark,PHD}}$, correspond to the QE. The PHD current has then further to be divided by the PHD QE, which itself is wavelength dependent. These relations are described by the following formula:

$$\mathrm{QE}(\lambda) = \mathrm{QE}_{\mathrm{PHD}}(\lambda) \cdot \frac{I_{\mathrm{PMT}} - I_{\mathrm{dark,PMT}}}{I_{\mathrm{PHD}} - I_{\mathrm{dark,PHD}}} \tag{6.2}$$

To make sure the result of this process represents the 'pure' QE and does not contain losses from collection efficiencies inside the PMT, there is a special operation mode for QE measurements. A high voltage (HV) potential is applied between the photocathode and the first dynode of the multiplier, which is visualised in figure 6.2. Though in this mode, the multiplier system is shorted out, i.e. the focus electrode, the dynodes and the anode all lie on the same potential. This has the effect that every electron that escapes the photocathode can hit the inner structure anywhere inside the PMT to contribute to the output. This obviously also disables the multiplication of the signal, which is why quite strong illumination is used to get measurable signals that have to be recorded with a picoampere meter.

The QE operation mode of the PMT works in both HV polarisations. For negative operation, the photocathode is connected to negative HV and the multiplier system is on ground. For positive operation, the photocathode is on ground and a positive HV is applied to the first dynode. Theoretically, it is favourable to measure 'how many electrons leave the photocathode' with positive operation instead of 'how many electrons reach the dynode system' with negative operation, since in the latter one would have to account for potential losses of electrons on their trajectories through the PMT. This hypothesis was tested in section 8.1.

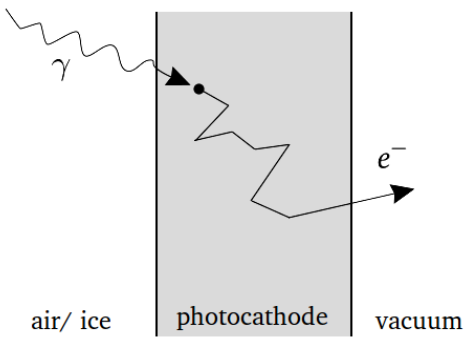

Figure 6.1: Visualisation of a photon being converted into an electron inside the photocathode of a PMT (grey). The three important processes for conversion are the absorption of the photon (left), the diffusion of the electron inside the cathode (middle) and its emission from the surface (right). The glass window between photocathode and surrounding medium is left out in this figure for simplification.

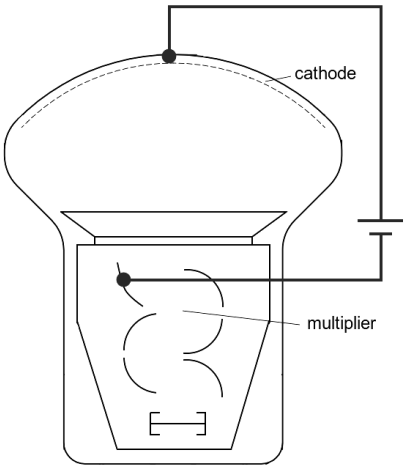

Figure 6.2: The QE operation mode of the PMT requires a shorted-out multiplier system. The potential that is applied to the first dynode is the same as for the rest of the multiplier system.

6.2 Quantum efficiency calculations

Before making predictions about the QE, it is useful to recapitulate the basic principles of light propagation in media. The knowledge of the basic optic laws and principles that are content of the next section is very important for understanding PMTs and photocathodes especially, which is why they are described here in some detail.

6.2.1 Light propagation in media

Many optical properties of the PMT components are described in terms of reflection and transmission. There is a wide range of differing terminology used in literature, so at first some terms have to be defined as they are used in this thesis, to avoid confusion. If not denoted otherwise, all formulae are taken from reference [21] (some are adjusted in terminology to better fit into the context of this section).

- The amplitude reflection and transmission coefficients (or short just reflection and transmission coefficients) of a bounding surface of two media are defined for parallel (index p) and perpendicular (index s) polarised light, with respect to the plane of incidence, as the ratio of the reflected (transmitted) wave E_r (E_t) to the incident wave E_0, respectively [21, 22] (pp. 40-41, p. 51):

$$r_\mathrm{p,s} = \left(\frac{E_\mathrm{r}}{E_0}\right)_\mathrm{p,s} \qquad t_\mathrm{p,s} = \left(\frac{E_\mathrm{t}}{E_0}\right)_\mathrm{p,s}$$

  Both r and t can be calculated with the Fresnel equations, which are introduced later in this section.

- The reflectance and transmittance are, in contrast to the reflection and transmission coefficients, denoted with capital letters R and T, and defined by [21] (p. 60):

$$R_\mathrm{p,s} = \left|\left(\frac{E_\mathrm{r}}{E_0}\right)_\mathrm{p,s}\right|^2 = \left|r_\mathrm{p,s}\right|^2 \tag{6.3}$$

$$T_\mathrm{p,s} = \frac{N_j \cos\theta_j}{N_i \cos\theta_i}\left|\left(\frac{E_\mathrm{t}}{E_0}\right)_\mathrm{p,s}\right|^2 = \frac{N_j \cos\theta_j}{N_i \cos\theta_i}\left|t_\mathrm{p,s}\right|^2 \tag{6.4}$$

  Where $N_{i,j}$ are the refractive indices of the media i and j, and $\theta_{i,j}$ the angle of incidence/ the angle of refraction, respectively, relative to the normal. Like r and t, R and T hold for each polarisation of light separately. They are directly measurable entities which makes them useful tools for characterising optical components. Together with the absorbance A, they will later be referred to as 'optical functions'.

Every medium is characterised by its complex refractive index [21, 22] (p. 613, p.49)

$$N = n + i\kappa\,,$$

where the real part n stands for the refraction of light in the medium, and κ, also called the extinction coefficient, is proportional to the material's absorption of light. Both n and κ are wavelength-dependent. For materials that are transparent and therefore nonabsorbent in the considered wavelength range, like air or vacuum, the refractive index is real and $N = n$ applies; those are called dielectric media. For most materials, it is rather complicated if

not impossible to predict the behaviour of $N(\lambda)$. In most cases N has to be investigated experimentally (e.g. with a process called ellipsometry[8]) for each wavelength. However, for some media such as glasses, at least the real part n of the refractive index can be defined by a function called the Sellmeier equation [23] (p. 10)

$$n^2(\lambda) = 1 + \sum_m \frac{B_m \lambda^2}{\lambda^2 - C_m} \tag{6.5}$$

where the material-specific coefficients B_m are dimensionless and C_m are usually given in units of μm^2.

In the picture of ray optics, light that impinges on the bounding surface of two different media i and j is refracted following Snell's law [21, 24] (p. 6, p. 38)

$$\frac{\sin(\theta_i)}{\sin(\theta_j)} = \frac{N_j}{N_i} \tag{6.6}$$

where θ_i is the angle of incidence in the first medium and θ_j the angle of propagation in the second medium; both with respect to the normal. N_i and N_j are the refractive indices of the first and second medium, respectively.[9]

The reflection and transmission coefficients of a bounding surface, as they are defined above, can also be described by the Fresnel equations [21] (p. 40)

$$r_{ij_\mathrm{p}} = \frac{N_j \cos(\theta_i) - N_i \cos(\theta_j)}{N_j \cos(\theta_i) + N_i \cos(\theta_j)}, \quad r_{ij_\mathrm{s}} = \frac{N_i \cos(\theta_i) - N_j \cos(\theta_j)}{N_i \cos(\theta_i) + N_j \cos(\theta_j)} \tag{6.7}$$

$$t_{ij_\mathrm{p}} = \frac{2N_i \cos(\theta_i)}{N_j \cos(\theta_i) + N_i \cos(\theta_j)}, \quad t_{ij_\mathrm{s}} = \frac{2N_i \cos(\theta_i)}{N_i \cos(\theta_i) + N_j \cos(\theta_j)} \tag{6.8}$$

for parallel (index p) and perpendicular (index s) polarised light with respect to the plane of incidence. The corresponding reflectance $R_{ij_{\mathrm{p,s}}}$ and transmittance $T_{ij_{\mathrm{p,s}}}$ are defined by (6.3) and (6.4). For bounding surfaces of at least one absorbent material one has

$$R + T + A = 1\,. \tag{6.9}$$

with the absorbance A. For two transparent materials, (6.9) simplifies to [21] (p. 41)

$$R + T = 1\,. \tag{6.10}$$

At an optical interface where light propagates from a medium N_i into a medium N_j, total reflection can occur if the angle of incidence θ_i is larger than a certain critical angle θ_c. For $N_j > N_i$, this critical angle is always 90 °. For $N_j < N_i$ however, θ_c can be much smaller, as visualised in figure 6.3, where the reflectance is plotted against the incident angle of the light with respect to the normal. The critical angle can be calculated with the formula

$$\theta_\mathrm{c} = \arcsin\left(\frac{N_j}{N_i}\right)$$

according to Snell's law. Total reflection plays an important role in investigating optical

[8] Ellipsometry is a procedure for optical investigations of thin layers by means of light polarisation [20].

[9] In an optical setup consisting of m parallel layers of media with different refractive indices, the angle of propagation θ_m in the last medium only depends on the original angle of incidence θ_1 in the first medium and the refractive indices of the first and last medium N_1 and N_m, as can be verified with a simple calculation. This phenomenon is important for understanding PMTs, where light has to cross several different layers including glass, photoemissive material and vacuum (see figure 6.5a).

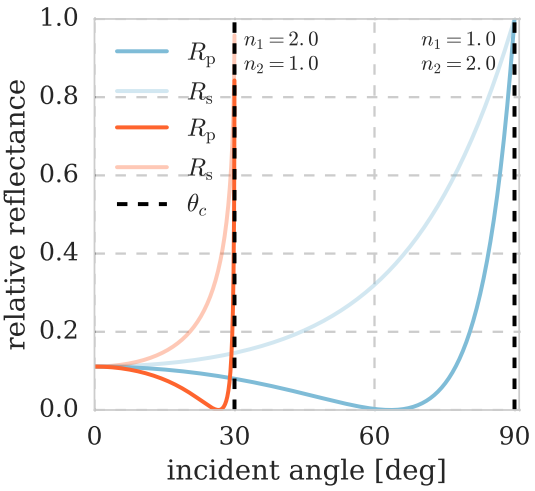

Figure 6.3: Reflectance at a bounding surface of two materials with real refractive indices $n_{1,2}$. The plot shows the two situations $n_1 > n_2$ (orange) and $n_1 < n_2$ (blue) for parallel and perpendicular polarised light with respect to the plane of incidence. The critical angles of total reflection for both situations are marked with dashed lines.

properties of PMTs, especially if $N > 1$ holds for the surrounding medium (like in ice or water). Furthermore, some of the experiment components like optical fibres are based upon this principle.

For two dielectric media, there is an incident angle at which the reflectance of the parallel polarised wave with respect to the plane of incidence drops to zero and only the perpendicularly polarised wave gets reflected, as can be seen in the plot. This angle is called Brewster-angle. [24] (p. 231). For media with attenuation ($\kappa \neq 0$), the p-wave reflectance has a minimum at this angle but is different from zero, so that the light only gets polarised partly [21] (pp. 41-43).

6.2.2 Optical properties of a PMT

All considerations made in this section, including its subsections, are based upon the works of [21] (pp. 61-62, 324-325, 615-616, 629-633), [25] (pp. 12-16), [22, 20, 26]. They will also be denoted as such in the following.

The QE mainly is a photocathode property. However, the photocathode is included in a system of four material layers (listed below), and light that hits the PMT interacts with all of them. Most importantly, it has to pass the glass window in order to reach the photocathode. So to get an idea of how the QE may behave concerning different parameters like wavelength and incident angle of the light, we first need a way to differentiate the optical behaviour of the photocathode from the optical behaviour of the glass window. The three interesting optical functions for these investigations are the reflectance R, the transmittance T and the absorbance A of the two components [20]. All three functions are depending on the wavelength and the incidence angle of the light, where the ranges of interest are $300 - 700\,\text{nm}$ and $0 - 90\,°$. The relevant media and PMT components for the investigations are:

1. The surrounding medium (in the following denoted with medium 1), which is air in my measurements and will later be ice when deployed in the actual detector[10],
2. the glass window (medium 2) which in the following is the borosilicate glass BK7 by SCHOTT[11],
3. the photocathode (medium 3) which is a thin film[12] of a potassium (K), caesium (Cs) and antimony (Sb) alloy evaporated onto the glass window,
4. the vacuum (medium 4) inside the PMT.

[10] At least indirectly; the PMTs will be housed inside a pressure sphere which separates them from the ice. Additionally they are surrounded by an optical gel to reduce refractive index differences.

[11] Different PMTs are manufactured with different kinds of borosilicate glasses. All borosilicate glasses have very similar optical properties though, so it is justifiable to use the most common one for the calculations.

[12] For a definition of thin films see 'Optical functions of the photocathode' later in this section.

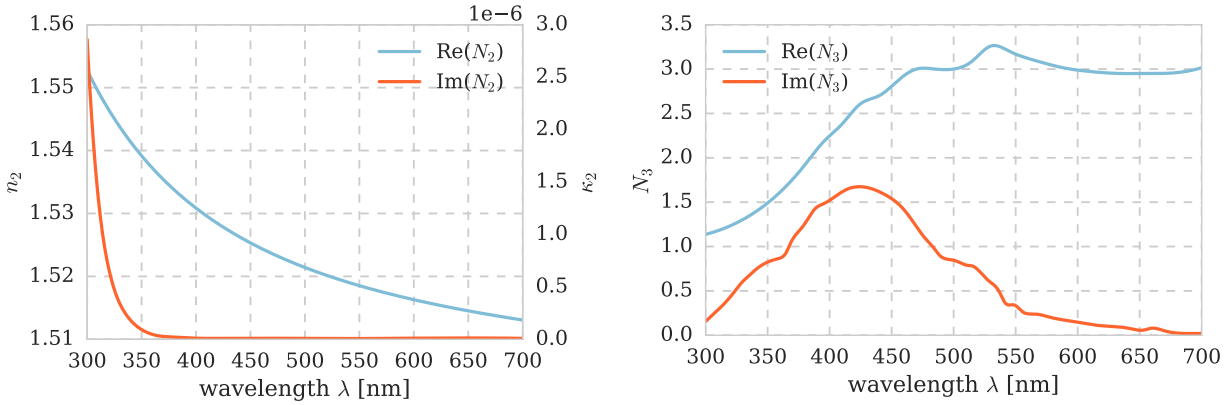

(a) (b)

Figure 6.4: **(a)** Refractive index $N_2 = n_2 + i\kappa_2$ of the glass window plotted against the wavelength. The blue curve shows the real part n_2 as calculated with the Sellmeier equation (6.5). The orange curve shows the imaginary part κ_2. Values taken from [27]. **(b)** Refractive index $N_3 = n_3 + i\kappa_3$ of the KCsSb photocathode plotted against the wavelength. The blue curve shows the real part n_3, the orange curve the imaginary part κ_3. Values taken from [28].

This optical system of four materials is visualised in figure 6.5b. Note that the theoretical investigations of the optical PMT properties are made for an hypothetical PMT with an ideally clean, flat entrance window and a perfectly homogeneously distributed photocathode, as well as a completely flat and homogeneous inner structure.

Refractive indices

To investigate the optical functions, one has to know the refractive indices N of each medium. For air and vacuum, no absorption occurs in the wavelength range of interest, and we have $N_{1,4} = n_{1,4} = 1.0$ [13] (p. E-381). The same is true for the glass window, although technically, glass is absorbent, but not to a noticeable degree except in the UV range. For our wavelengths range of $300-700\,\text{nm}$, the extinction coefficient κ_2 is effectively zero even for the smallest relevant wavelengths, which is why $N_2 = n_2$ can be assumed. This is visualised in figure 6.4a, where both n_2 and κ_2 are plotted against the wavelength. The real part n_2 can be calculated according to the Sellmeier equation (6.5) with the Sellmeier coefficients taken from reference [27]. As can be seen, n_2 changes very little over the whole wavelength range. The data for κ_2 was also taken from [27] and interpolated. Values for both indices can be found in table 10.1 in the appendix.

In the photocathode, the absorption plays a key role for the PMT functionality, and is obviously not negligible. Neither the real nor the imaginary part of $N_3 = n_3 + i\kappa_3$ were as easily accessible as for the other components. Luckily, for our photocathode material KCsSb it has been measured before[13] in reference [20] and corrected by reference [28]. The values were taken from [28] and interpolated, the result is shown in figure 6.4b. Both n_3 as well as κ_3 show large variations with λ. Values for N_3 are also listed in table 10.1.

[13]The knowledge of the composition and characteristics of commercially produced photocathodes is not readily given away by the manufacturers, and usually has to be obtained with complex experiments like ellipsometry [20], see footnote 8.

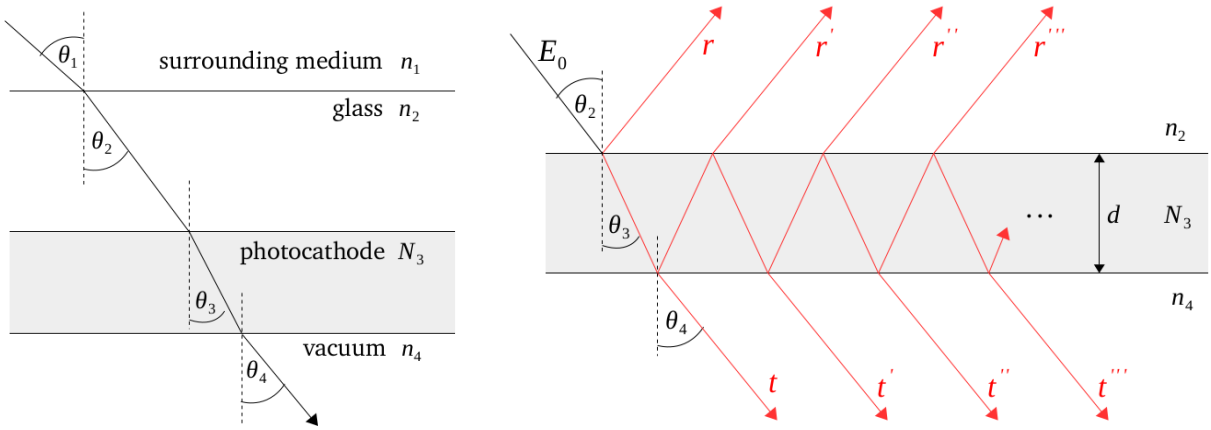

Figure 6.5: **(a)** Scheme of the four layers of the PMT with light incident under an angle θ_1. **(b)** Infinite internal reflection in a conductive layer (N_3) between two dielectric media (n_2, n_4), which represents the photocathode between glass and vacuum. The r, r', ... and t, t', ... are the components of the reflection and transmission coefficient of the layer, respectively.

Optical functions of the photocathode

The photocathode can be described as a thin conductive layer (CL) which is located between two dielectric materials, glass and vacuum. A thin layer or film is a material coating with a thickness of some nm up to several µm which is evaporated onto a substrate [29] (p.117). For such thin films, calculating the optical functions is not trivial, especially if the material is not dielectric as it is the case for photocathodes. So this section will provide a detailed derivation based upon [21, 22, 20].

Inside the conductive layer, theoretically an infinite number of reflections can occur, which leads to an infinite number of reflected and transmitted light components, as indicated by figure 6.5b. All the components that are reflected from the layer taken together are described by the reflection coefficient r_{CL}, all components that are transmitted through the layer (i.e. that come out on the other side) taken together are described by the transmission coefficient t_{CL}. Three considerations have been made for the calculation of r_{CL} and t_{CL}[14]:

1. The individual terms r, r', r'', ..., t, t', t'', ... of r_{CL} and t_{CL} are the products of the r_{ij} and t_{ij} which are the reflection and transmission coefficients at the bounding surface of material i and j, that are calculated with the Fresnel equations (6.7) and (6.8). The following relations are true for r_{ij} and t_{ij} in both absorbent and nonabsorbent media [21] (p. 324):
$$r_{ij} = -r_{ji}\,, \quad t_{ij}t_{ji} = 1 - r_{ij}^2 \tag{6.11}$$
From this it follows for the reflectance:
$$R_{ij} = R_{ji} = \left|r_{ij}\right|^2 = \left|r_{ji}\right|^2 \tag{6.12}$$

2. The angles of refraction that are necessary to get r_{ij} and t_{ij} can be calculated from medium to medium with Snell's law, starting with the angle of incidence $\theta_1 \equiv \theta$ as a variable.

[14] For a definition of r and t as well as R and T see section 6.2.1.

3. Every traverse through the conductive layer results in a factor of $e^{i\rho}$ with the phase difference [21] (p. 630)

$$\rho = \frac{2\pi d}{\lambda} N_3 \cos(\theta_3),$$

where λ is the wavelength of the incident light in vacuum and d is the thickness of the layer. The exponent ρ also includes the attenuation with N_3.

Assuming that the materials are numbered according to the figure 6.5b, the above considerations yield for the components of $r_{\mathrm{CL}} = r + r^{'} + r^{''} + ...$:

$$r = r_{23}, \quad r^{'} = t_{23} r_{34} e^{2i\rho} t_{32}, \quad r^{''} = t_{23} r_{34}^2 e^{4i\rho} r_{32} t_{32}, \quad ...$$

So r_{CL} becomes

$$r_{\mathrm{CL}} = r_{23} + t_{23} t_{32} r_{34} e^{2i\rho} \cdot \sum_{n=0}^{\infty} r_{34}^n r_{32}^n e^{2ni\rho} = r_{23} + \frac{t_{23} t_{32} r_{34} e^{2i\rho}}{1 - r_{32} r_{34} e^{2i\rho}} = \frac{r_{23} + r_{34} e^{2i\rho}}{1 + r_{23} r_{34} e^{2i\rho}} \tag{6.13}$$

with usage of the simple geometric series [25]

$$a \cdot \sum_{n=0}^{\infty} x^n = \frac{a}{1-x}, \quad x < 1$$

in the first step, and the relations (6.11) in the second step. Analogous for the transmission coefficient:

$$t_{\mathrm{CL}} = \frac{t_{23} t_{34} e^{i\rho}}{1 + r_{23} r_{34} e^{2i\rho}} \tag{6.14}$$

The reflectance and transmittance of the conductive layer are then obtained with formulas (6.3) and (6.4) to

$$R_{\mathrm{CL}} = |r_{\mathrm{CL}}|^2, \quad T_{\mathrm{CL}} = \frac{n_4 \cos(\theta_4)}{n_2 \cos(\theta_2)} |t_{\mathrm{CL}}|^2. \tag{6.15}$$

Since the r_{ij}, t_{ij} and ρ are theoretically directly accessible, we are done with the prediction of the optical functions of the photocathode with equations (6.15).

Nevertheless it might be interesting to have a closer look at R_{CL} and T_{CL}. Further studies including the dependence on the photocathode thickness d are discussed in section 10.2 in the appendix, which might also be helpful to understand the adaption of R_{CL} and T_{CL} to the optical functions of the glass window investigated in the following section.

Optical functions of the glass window

The glass window, like the photocathode, can be described as a layer between two media (air and the photocathode), which for now are both assumed to be dielectric. The absorption in the glass is negligible, which is why

$$\rho = \frac{2\pi d}{\lambda} n_2 \cos\theta_2 \tag{6.16}$$

is real and positive. With the glass as medium 2 between media 1 and 3 we then get:

$$\begin{aligned} r_{\text{win}} &= r_{12} + t_{12}t_{21}r_{23}e^{2i\rho} \cdot \sum_{n=0}^{\infty} r_{23}^n r_{21}^n e^{2ni\rho} \\ &= r_{12} + \frac{t_{12}t_{21}r_{23}e^{2i\rho}}{1 - r_{21}r_{23}e^{2i\rho}} = \frac{r_{12} + r_{23}e^{2i\rho}}{1 + r_{12}r_{23}e^{2i\rho}} \end{aligned} \tag{6.17}$$

If R_{win} is calculated analogous to R_{CL} in the previous section though, the resulting equation does not represent the reflectance of the glass window correctly. We rather have to account for the fact that the glass window is about 2 mm thick and thin layer optics does not apply anymore [25]. In thin layers, the light waves travel distances that are of the order of λ. On these scales the waves can be assumed to be monochromatic and coherent plane waves, which make them interfere with one another. On larger scales this is not possible anymore, because the light we use in the experiments is never ideally monochromatic and therefore has a very limited coherence length. This can be accounted for by not obtaining the reflectance with $R_{\text{win}} = |r_{\text{win}}|^2$ as it was done before, but by integrating $|r_{\text{win}}|^2$ as in (6.17) over the bandwidth $\Delta\lambda$ of the light source (following reference [25]). This bandwidth is assumed to be in the order of a few nm.

$$\begin{aligned} R_{\text{win}} &= \int_{\Delta\lambda} \left| r_{12} + t_{12}t_{21}r_{23}e^{2i\rho} \cdot \sum_{n=0}^{\infty} r_{21}^n r_{23}^n e^{2ni\rho} \right|^2 \frac{d\lambda}{\Delta\lambda} \\ &= \int_{\Delta\lambda} \Bigg\{ |r_{12}|^2 + |t_{12}t_{21}|^2 |r_{23}|^2 \sum_{n=0}^{\infty}\sum_{m=0}^{\infty} (r_{21}r_{23})^n (r_{21}^* r_{23}^*)^m e^{2i\rho(n-m)} \\ &\quad + r_{12}^* t_{12}t_{21}r_{23}e^{2i\rho} \sum_{l=0}^{\infty} (r_{21}r_{23})^l e^{2li\rho} + r_{12}t_{12}^* t_{21}^* r_{23}^* e^{-2i\rho} \sum_{k=0}^{\infty} (r_{21}^* r_{23}^*)^k e^{-2ki\rho} \Bigg\} \frac{d\lambda}{\Delta\lambda} \end{aligned}$$

It is now convenient to resolve this rather complicated looking equation piece by piece. The first term $|r_{12}|^2$ is independent of λ. In the second term the $e^{2i\rho(n-m)}$ oscillate very rapidly over the course of $\Delta\lambda$, and therefore average to zero for $n \neq m$. Only the factors with $n = m$ remain, which makes the exponent zero. The last two terms both average to zero for the same reason. Then we have

$$\begin{aligned} R_{\text{win}} &= |r_{12}|^2 + |t_{12}t_{21}|^2 |r_{23}|^2 \sum_{n=0}^{\infty} |r_{21}r_{23}|^{2n} = |r_{12}|^2 + \frac{|t_{12}t_{21}|^2 |r_{23}|^2}{1 - |r_{21}r_{23}|^2} \\ &= R_{12} + \frac{R_{23}(1 - R_{12})^2}{1 - R_{12}R_{23}} \end{aligned} \tag{6.18}$$

where in the last step the relations (6.11) and (6.12) have been used. Analogous for the transmission:

$$t_{\text{win}} = t_{12}t_{23}e^{i\rho} \cdot \sum_{n=0}^{\infty} r_{21}^n r_{23}^n e^{2ni\rho}$$

$$
\begin{aligned}
T_{\text{win}} &= \int_{\Delta\lambda} \left| t_{12} t_{23} e^{i\rho} \sum_{n=0}^{\infty} r_{21}^n r_{23}^n e^{2ni\rho} \right|^2 \frac{d\lambda}{\Delta\lambda} \\
&= \int_{\Delta\lambda} |t_{12} t_{23}|^2 \sum_{n=0}^{\infty} \sum_{m=0}^{\infty} (r_{21} r_{23})^n (r_{21}^* r_{23}^*)^m e^{2i\rho(n-m)} \frac{d\lambda}{\Delta\lambda} \\
&= |t_{12} t_{23}|^2 \sum_{n=0}^{\infty} |r_{21} r_{23}|^{2n} = \frac{|t_{12} t_{23}|^2}{1 - |r_{21} r_{23}|^2} \\
&= \frac{T_{23}(1 - R_{12})}{1 - R_{12} R_{23}}
\end{aligned} \tag{6.19}
$$

Optical functions of the PMT

To get the optical functions of the PMT as a whole, we have to combine the optical functions of the glass window with the ones of the photocathode. This is simply done by replacing the R_{23} and T_{23} in (6.18) and (6.19) with R_{CL} and T_{CL}:

$$R_{\text{PMT}} = R_{12} + \frac{R_{\text{CL}}(1 - R_{12})^2}{1 - R_{12} R_{\text{CL}}} \tag{6.20}$$

$$T_{\text{PMT}} = \frac{T_{\text{CL}}(1 - R_{12})}{1 - R_{12} R_{\text{CL}}} \tag{6.21}$$

The absorption can then be obtained with (6.9) to

$$A_{\text{PMT}} = 1 - R_{\text{PMT}} - T_{\text{PMT}} \,. \tag{6.22}$$

Equations (6.20), (6.21) and (6.22) are the optical functions of the PMT we have been looking for. If we now want to compare the optical functions of the PMT as a whole to the optical functions of the photocathode, it is useful to make a further alteration, though. Because for plotting the optical functions of the photocathode, R_{CL} and T_{CL} are rather unsuitable representations. It makes sense to only consider the amount of light that is transmitted through the glass window and actually reaches the photocathode. This can simply be achieved by multiplying R_{CL}, T_{CL} and A_{CL} with the transmittance $T_{12} = (1 - R_{12})$, which is the percentage of incident light that passes the first bounding surface of air and glass:

$$
\begin{aligned}
R_{\text{PHC}} &= (1 - R_{12}) R_{\text{CL}} \\
T_{\text{PHC}} &= (1 - R_{12}) T_{\text{CL}} \\
A_{\text{PHC}} &= (1 - R_{12}) A_{\text{CL}}
\end{aligned}
$$

This has the effect that all three functions drop to zero when drawn against the incident angle of light θ for $\theta = 90\,^\circ$, because $R_{12}(90\,^\circ) = 100\,\%$.

The wavelength dependence of the optical functions of the photocathode and the PMT are shown in figure 6.6. The PMT optical functions do not differ much from the ones of the photocathode, which indicates that the photocathode is the optically dominant element of the PMT. Furthermore, the optical functions follow more or less the curve (or inverse curve in case of the transmission) of the refractive index of the photocathode, as can be seen when comparing them to figure 6.4b. The reflectance resembles the real part n_3 of the refractive index, whereas the absorption resembles the imaginary part κ_3, which also makes perfect

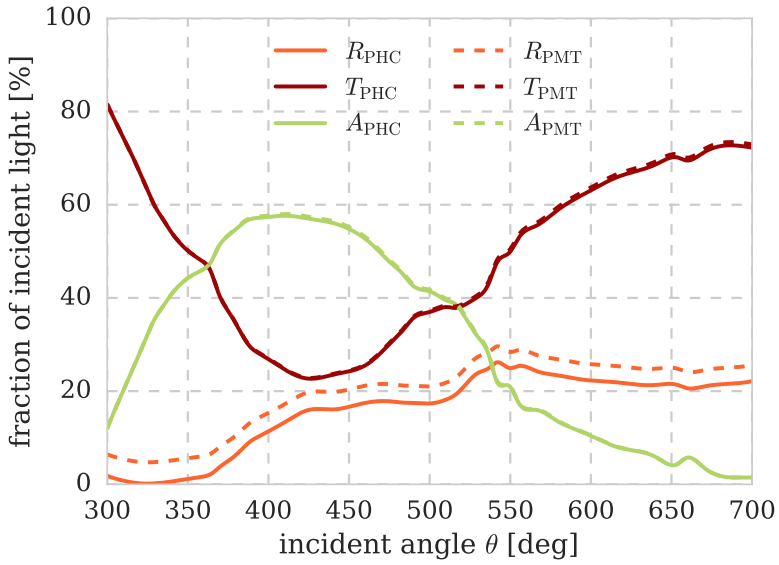

Figure 6.6: The reflectance R, transmittance T and absorbance A of the photocathode (solid lines) and the PMT as a whole (dashed lines) plotted against the wavelength λ, with $n_{1,4} = 1.0$, $n_2 = n_2(\lambda)$, $N_3 = N_3(\lambda)$, $\theta = 0°$, $d = 20\,\text{nm}$. The optical functions of the photocathode have been corrected for the losses at the glass window as explained in the text.

sense because n_3 causes refraction and κ_3 causes attenuation. The optical functions against the wavelength for several different incident angles can be found in figures 6.8a-c.

The angular dependence of the optical functions of the photocathode as well as the PMT are shown in figure 6.7. The optical functions follow expected plateau-like curves. For the PMT (dashed lines) at about 50 °, the Fresnel reflection at the glass window comes into play, which results in a steep rise in R_{PMT} and a decrease towards zero for the other functions. The optical functions of the photocathode (solid lines) are corrected for these losses at the window and therefore drop to zero, too, as explained earlier. By comparing the PMT and the photocathode, it can be seen that the optical functions look almost the same for smaller angles, which means that the photocathode dominates the optical functions of the PMT as already indicated by figure 6.6, until the Fresnel reflection of the glass window takes over. For small angles altogether, the plot reveals a 'reflection loss' of 3.96 % caused by the glass.

The absorption of the PMT A_{PMT} is about 0.3 % higher than the absorption of the photocathode A_{PHC} alone. This may seem puzzling at first, because the photocathode is the only component of the PMT that is assumed to be absorbent. The reason is, however, that the glass window gives the light that is first reflected at the glass-photocathode interface (R_{12}) another chance to be absorbed in the photocathode by reflecting it back any number of times. This effect is considered in A_{PMT} but not in A_{PHC}.

The optical functions of the photocathode and the PMT against the incident angle are shown again in figures 6.8a-c, this time for several different wavelengths. Some remarkable features can be seen especially in the reflectance plots. Some of the curves show a peak at large angles right before dropping to zero, instead of the expected plateau-like shape. This effect is noticeable especially for the smallest and largest wavelengths. It might arise from the wavelength-dependent phenomenon of an in-part-polarisation at the Brewster-angle (see section 6.2.1), but could not be investigated further in the scope of this thesis. The absorbance curve mirrors this effect for $\lambda = 300\,\text{nm}$, which simply results from the large

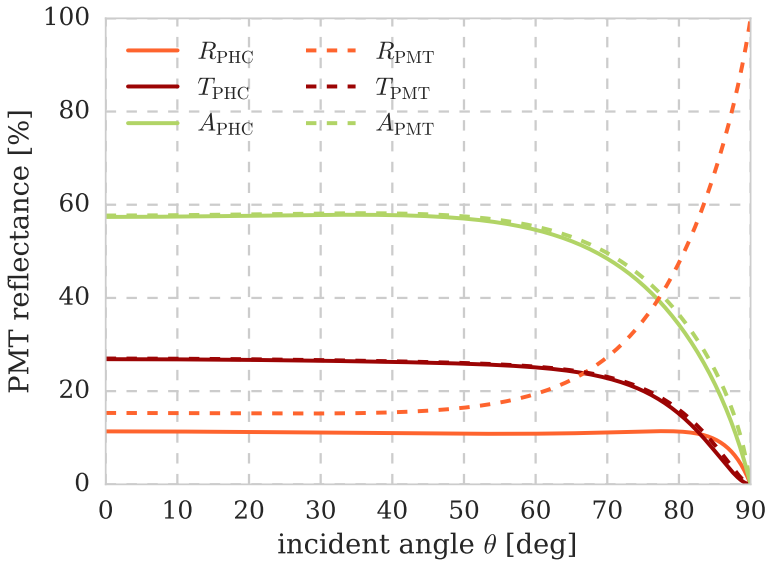

Figure 6.7: The reflectance R, transmittance T and absorbance A of the photocathode (solid lines) and the PMT as a whole (dashed lines) plotted against the incident angle of light θ, with $n_{1,4} = 1.0$, $n_2 = 1.53$, $N_3 = 2.25 + 1.52i$, $\lambda = 400\,\text{nm}$, $d = 20\,\text{nm}$. The optical functions of the photocathode have been corrected for the losses at the glass window, which is why they drop to zero for $\theta = 90°$ as explained in the text.

difference of R and T for this wavelengths though. By having a close look at the plot and recalling formula $A = 1 - R - T$, the shape of A can easily be comprehended from the shapes of R and T. Later in the measurement of the angular dependence of the QE (see section 8.3), similar shapes will occur. However, they are assumed to mostly arise from other effects (as will be explained there) and should not be confused with this phenomenon, which only occurs for wavelengths not being investigated in the measurements[15].

6.2.3 Wavelength dependence of the quantum efficiency

The QE is determined by the absorption in the photocathode which can be seen by recalling formula (6.1):

$$QE(\lambda, \theta) = A(\lambda, \theta) \cdot P_{\text{conv}}(\lambda)\,.$$

The conversion coefficient remains unknown for now, but A should at least provide a rough prediction of the shape of the wavelength dependence of the QE. It is not enough though to just take the absorption from figure 6.6. The measurement (see section 8.2) is assumed to yield slightly higher values for the QE than shown in the figure (where we are ignoring P_{conv} for a while). This is due to the effect of photons being transmitted through the PMT layers including the photocathode and then being back-reflected from the inside metal structure of the PMT. These photons get another chance of being absorbed in the photocathode. The absorbance A_{back} seen by these photons can be calculated the same way as for the incident

[15] Measurements in wavelength ranges around 300 nm and 700 nm could not be further investigated due to setup constraints, mostly a lack of statistics caused by unsuitable optical components as discussed in chapter 8.

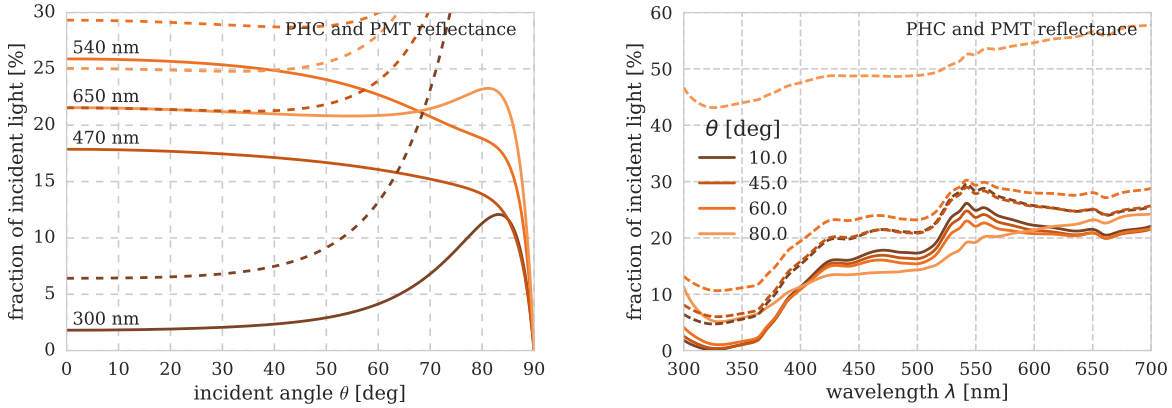

(a)

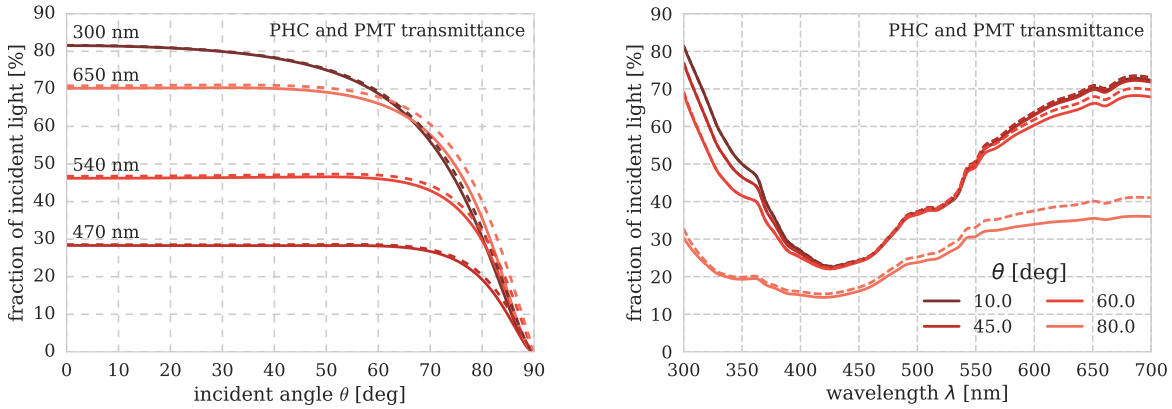

(b)

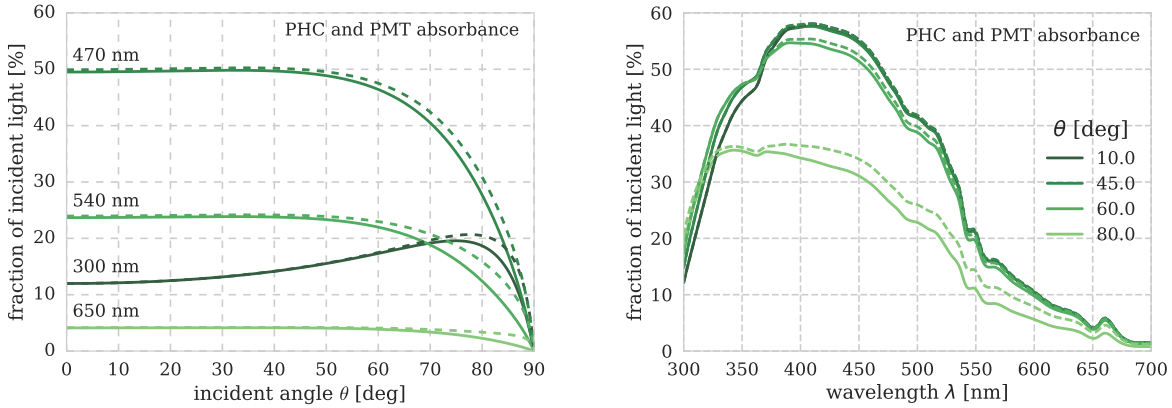

(c)

Figure 6.8: Prediction of the **(a)** reflectance, **(b)** transmittance and **(c)** absorbance against the incident angle θ for several wavelengths on the left, and against the wavelength λ for several incident angles on the right. Shown are the predictions for the photocathode alone (solid lines) as well as for the PMT as a whole (dashed lines), where in each plot same colours indicate same wavelengths/ same incident angles. With $n_{1,4} = 1.0$, $n_2 = n_2(\lambda)$, $N_3 = N_3(\lambda)$, $d = 20\,\text{nm}$.

photons, but obviously with the reverse order of materials[16]. The total percentage of absorbed light of the whole PMT is then given by the sum of A_{PMT} and A_{back} multiplied with the fraction of light that gets back-reflected, which is $\sim 70\,\%$ of the light that gets transmitted into the PMT according to reference [20]:

$$A_{\text{eff}} \;=\; A_{\text{PMT}} + A_{\text{back}} \cdot 0.7 \cdot T_{\text{PMT}}$$

A_{eff}, which is shown in figure 6.9 next to A_{PMT} and A_{back}, is the provisional prediction for the shape of $QE(\lambda)$. The amount of back-reflected light probably deviates from 70 % for different wavelengths. An even larger deviation will arise from the inhomogeneous inner structure in 'real' PMTs in contrast to the ideal PMT on which base this prediction is made, which is why the assumption of $\sim 70\,\%$ for simplification is justified.

The result for $QE(\lambda)$ is shown in figure 6.9. The shape of A_{back} is relatively flat, so A_{eff} mainly follows the shape of A_{PMT} with a maximum value of $\sim 65\,\%$ at $\sim 380\,\text{nm}$. Of course A_{eff} is an 'incomplete' prediction of the shape for the wavelength dependence of the QE, since the conversion coefficient $P_{\text{conv}}(\lambda)$ is still not included. $P_{\text{conv}}(\lambda)$ can be found by measuring $QE(\lambda)$ and comparing it to its prediction A_{eff} with formula (6.1):

$$P_{\text{conv}}(\lambda) = \frac{QE(\lambda,\theta)}{A_{\text{eff}}(\lambda,\theta)}\,. \tag{6.23}$$

The measurement to investigate $QE(\lambda)$ and $P_{\text{conv}}(\lambda)$ can be found in section 8.2.

6.2.4 Angular dependence of the quantum efficiency

For the prediction of the angular dependence of the QE, it is, like in the previous section, not enough to just take the absorption from figure 6.7. The back-reflection of photons from the inside of the PMT has to be taken into account here as well. The result is shown in figure 6.10. As can be seen with A_{back}, about 8 % of the incident light gets absorbed again. A_{eff} as the sum of A_{PMT} and A_{back} is the prediction for the shape of $QE(\theta)$. Its maximum value is $\sim 65\,\%$ for small angles. Again, A_{eff} is an 'incomplete' prediction, because P_{conv} is not included here as well. But since P_{conv} is independent of θ, A_{eff} has to be simply multiplied with a constant factor for the respective wavelength, according to formula (6.1). When $P_{\text{conv}}(\lambda)$ has been obtained in the wavelength dependence measurement in section 8.2, A_{eff} can be corrected to provide an absolute $QE(\theta)$ prediction. The measurements of $QE(\theta)$ can be found in section 8.3.

[16] The inside metal structure is here assumed to be flat, so that the 'incident angle' with which the photons hit the photocathode from the inside equals the refraction angle in the vacuum which can be calculated with Snell's law (6.6).

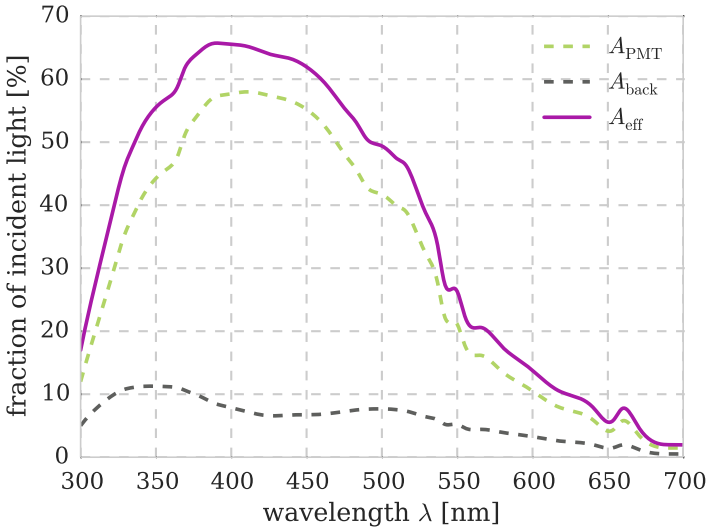

Figure 6.9: The effective absorption of the PMT (purple) against the wavelength λ. It consists of the PMT initial absorption (dashed green) plus the absorption of the back-reflected light from the inside metal structure of the PMT (dashed grey). A_{eff} roughly predicts the shape of the wavelength dependence of the QE. The following parametrisation was used: $n_{1,4} = 1.0$, $n_2 = 1.53$, $N_3 = 2.25 + 1.52i$, $\theta = 0°$, $d = 20\,\text{nm}$.

Figure 6.10: The effective absorption of the PMT (purple) against the incident angle θ. It consists of the PMT initial absorption (dashed green) plus the absorption of the back-reflected light from the inside metal structure of the PMT (dashed grey). A_{eff} predicts the shape of the angular dependence of the QE. The following parametrisation was used: $n_{1,4} = 1.0$, $n_2 = 1.53$, $N_3 = 2.25 + 1.52i$, $\lambda = 400\,\text{nm}$, $d = 20\,\text{nm}$.

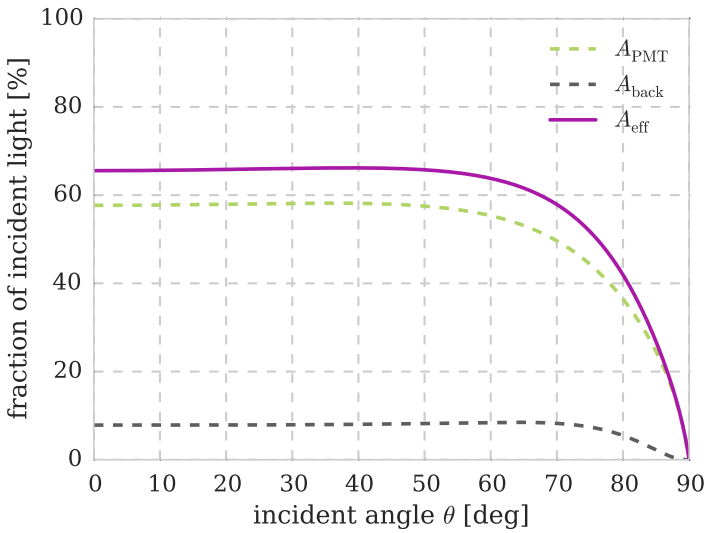

7 Setup and commissioning of the QE test stand

With the QE test stand, three different characteristics were to be investigated for the time being:

- The wavelength dependence of the QE, where a PMT is illuminated at the centre point of its photocathode. The light source is tunable, so that the output current can be acquired as a function of the wavelength.
- The angular dependence of the QE, where a PMT is illuminated at the centre point of its photocathode. While the PMT is being rotated to change the incident angle of the light, the output current is recorded as a function of this angle.
- The photocathode position dependence of the QE, where a PMT front is scanned in two dimensions with a well defined light spot, and the output current data is acquired as a function of the light spot coordinates on the PMT surface.

Several pieces of hardware had to be designed and built for these measurements, and some existing devices had to be altered. They were composed into complex setups, that together form the QE test stand. The design, functionality and commissioning of the individual devices are described in the following sections, as well as features and properties of other important measurement components and the test stand as a whole.

Most of the technical devices of the QE test stand are controlled remotely. Almost all of these controls were programmed as a part of this thesis. They were combined into a Python script that in the following is referred to as the QE test stand Python script. The basic controls of the individual hardware components consist of a set of (sometimes more, sometimes less simple) module control functions prescribed by the manufacturers, which will not be discussed in the following. The more interesting scan routines which rely on the combination of all these hardware controls are described in detail in chapter 8.

7.1 The Blackbox

PMTs are extremely light-sensitive. They are designed to detect the smallest amounts of light, even single photons. So any measurements concerning PMT characteristics have to take place in absolute darkness. This is achieved by performing the measurements inside the so-called *Blackbox* where no light can reach the setup components.

The Blackbox that was built for the QE test stand is a $2 \times 1 \times 1\,\mathrm{m}^3$ dimensioned wooden box with an especially light tight design. The contact surfaces of two panels are potential light leaks, so they are not just screwed or glued together, but have several interlocking step-like tiers. The front wall features two removable doors. Since removable parts are always a risk in terms of light tightness, the doors can be covered with a black blanket from the outside, as can be seen in figure 7.1. The box is painted black on the inside, so that light that may enter gets absorbed as soon as possible. On both sides the box is equipped with so-called photon mazes that are also shown in figure 7.1. Those are maze-shaped anodised aluminium tunnels, through which cables can be laid from the outside into the box. Cables can be bent along the maze, but light moves straight-line and gets blocked. The more bending-sensitive optical fibres are fed through an opening in one of the side panels. The monochromator (see section 7.4.2) also has a dedicated feed-through located next to

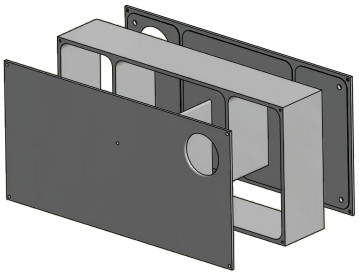

Figure 7.1: **Left:** The Blackbox of the QE test stand with the blanket that is used to cover the doors from the outside. It has plenty of room for all kinds of QE related setups. The monochromator and the xenon lamp can be seen in the very left edge of the photo. **Right:** Technical drawing of a photon maze. The Blackbox has a double version of it on each side panel, where one is installed from the inside and one from the outside, so that light would have to pass both to reach the inside of the box. One of the outer mazes can be seen on the right side panel of the box in the photograph. Picture courtesy of the Münster IceCube group (modified).

it. A large anodised breadboard is screwed to the ground panel of the box, which provides a large base for a variety of opto-mechanical setups.

The light-tightness of the box has been first tested with visual judgement[17] and longtime exposure photographs of a reflex camera, and afterwards with a PMT. For that purpose, the darkrate of the PMT was read out with an oscilloscope and compared to the darkrate the same PMT produced when inside one of the already light-tight-proven smaller black boxes. None of these tests showed any indication of light leakage. A possible weak point is considered the fibre feed-through, though. When not in use, it is well sealed, but when a fibre or another cable is deployed, it can only be closed off with black foam and tape, which can easily get out of place.

A disadvantage of the Blackbox is its material. Made of wood, it does not provide any electromagnetic shielding for extraordinarily sensitive instruments like PMTs. So smaller metal boxes have to be used inside the box during measurements, that take up unnecessary space and make setup adjustments more complicated. A shielding of the Blackbox as a whole could be a future project to further improve the QE test stand.

7.2 The 3D scanner

The 'heart' of the setup is the 3D scanner, which, like the Blackbox, was specifically designed and constructed for the QE test stand[18]. It consists of three levels of linear rails with stages than can move along these rails, as shown in figure 7.2. The top level rail is attached to the middle level stage, and the middle level rail is attached to the ground level stage. The stages are individually actuated by stepper motors which can be controlled independently

[17] Which was not very helpful, because after some time in the complete darkness of the box ones eyes start to make up light flashes (really).

[18] Final design and construction by Dipl. engineer Christian Huhmann.

from one another. Each stage can move 25 cm in its allocated direction, which results in an operating volume of 15.6 dm^3. An object that is attached to the top stage can be moved to any point in this volume. Per definition the lowest stage moves along the x-axis, the middle stage along the y-axis and the top stage along the z-axis. The system is mounted on a base of *Kanya* profiles which is equipped with four adjustable rubber pedestals to provide a level and stable experimental condition. The control of the scanner's stepper motors is part of the QE test stand Python script.

In the measurements, light from a light source[19] is coupled into an optical fibre, where the end of the fibre is attached to a collimator that is fixed to the top stage of the scanner. This way, the output point of the light can be moved freely within the operating volume without moving the actual light source around. With this opto-mechanical setup, it is possible to perform a 3D optical screening of a PMT. Originally, the PMT was supposed to be mounted gyroscopically to be rotated in all directions as a part of the scanner setup. This could not be realised in the terms of this thesis[20], so the PMT remains fixed and faces a certain direction at all times. The collimator is also fixed to the top scanner stage, so the light spot can only be pointed in x-direction. That means that effectively only 2D scans with flexible output - PMT distance are possible at the moment. The procedure of such a scan is described in detail in section 8.4.

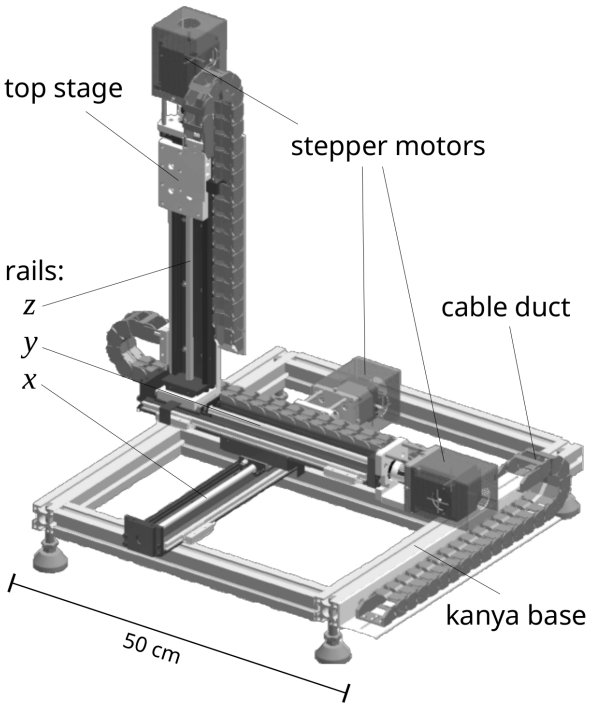

Figure 7.2: Technical drawing of the 3D scanner that was designed and built for the QE test stand. It consists of three stepper motors that power three independently movable stages on rails in three directions (denoted with x, y, z). Picture courtesy of the Münster IceCube group (modified).

Before any measurement operation, the scanner performs a reference point search. For this purpose, the control boards of the motors are equipped with a feature named *StallGuard*, which can detect changes in motor load. As soon as the load exceeds a defined threshold, e.g. by driving the stages into a hardware stop or an obstacle, the motor is stopped immediately. For the reference point search, each stage is driven against the limit, i.e. the metal frame, of its rail. When stopped by StallGuard, the current motor position is set to 0. This means that each scanner stage moves relative to the reference point of its axis, where these points do not coincide with each other due to the setup limitations. The scanner is currently not adjustable to a well defined reference coordinate $(0, 0, 0)$.

The scanner can approach a coordinate with a (conservative) accuracy below 50 µm in each direction. This has been investigated by driving the stages to several positions and compare the given distance to the respective reference point with the actual distance, which was measured with a micrometer screw. The limiting factor was the effective uncertainty[21] of the screw which lies at the above mentioned ±50 µm, but the scanner is assumed to

[19] The different light source options are described in section 7.4.
[20] The gyroscopic PMT mounting will be a followup QE test stand project.
[21] Potential imprecision in operating the screw are already included.

have a much better accuracy. Furthermore, a defined coordinate is reproducible over long measurement times. This has been tested by approaching a coordinate, then moving the scanner around to several hundred random coordinates, and then approaching the original coordinate again to test with the micrometer screw if it has still the same distance to each reference point as before. This was done for the scanner in normal and tilted orientations up to 90°. All tests showed no measurable deviations in positioning. Although the system turned out to be very stable over long operation times, the scanner performs a new reference search before any new operation 'just in case', since the motors are not equipped with encoders[22].

7.3 The rotation table

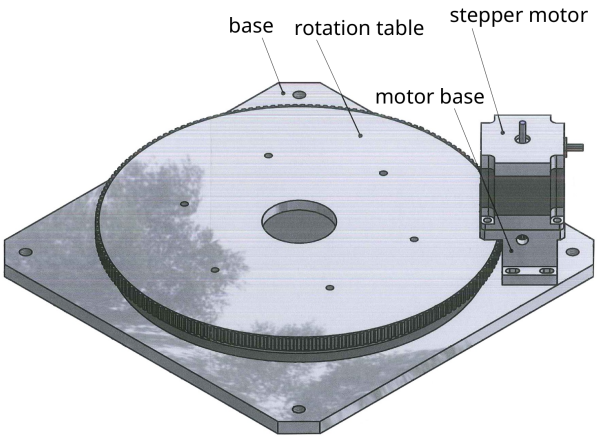

Figure 7.3: Technical drawing of the rotation table for investigating the angular dependence of the QE. The stepper motor that drives the rotation meshes a sprocket that is glued to the side of the table. Full rotations in both directions are possible. Picture courtesy of the Münster IceCube group (modified).

For the angular dependence investigations of PMT properties, it is easier to rotate the PMT instead of changing the direction of the light beam. So for such measurements the light source remains fixed and the PMT is mounted on a rotatable table[23], which is shown in figure 7.3. This table consists of two circular plastic plates with a ball bearing between them, allowing the upper plate to be moved relatively to the lower one. The upper plate has a sprocket glued to its side which meshes with a stepper motor that is fixed next to the rotation table. Any desired rotation angle in both directions can be set. A PMT can be mounted on an optical rail that is fixed to the upper plate (not shown in the picture). It can be adjusted in a way that the centre point of the photocathode coincides with the rotation axis of the plate. That means that during the whole measurement only the centre point is illuminated. The incident angle of the light can be changed in both directions by rotating the upper plate around. The rotation table control is part of the QE test stand Python script.[24]

The accuracy of the rotation table in the first place is limited by the rather unstable suspension of the two plastic plates. The upper plate has a vertical moving tolerance relatively to the lower one at the outermost area, which results in a conservative vertical positioning uncertainty of 1 mm at the edge. The sprocket has a horizontal tolerance of about 1 mm which results in a conservative angular uncertainty of 0.5°. The latter uncertainty can be evaded by keeping the motor engaged at all times in a measurement. When engaged, the motor's holding torque is large enough to prevent horizontal tolerance. The motor is equipped with an optical encoder to correct for stepping errors, which has been calibrated to 11332 steps for one full table rotation. The

[22] There are different kinds of encoding devices for stepper motors. An optical encoder is shortly explained in section 7.3.

[23] The rotation table was designed and constructed by the mechanics workshop of the Erlangen Centre of Astroparticle Physics.

[24] This basic motor control is partly adapted from a script written by Lew Classen and Jonas Reubelt at the Erlangen Centre of Astroparticle Physics.

encoder compares the movement of the motor shaft to an internal line pattern, 'counting' the actual motor steps. The stepper motor has been calibrated to 60442 steps for one full table rotation, which has been tested by driving the table several hundred full rotations to magnify possible errors in angle-to-motorstep conversion. This resulted in an angular positioning accuracy of below 0.2° per 100 full rotations. Unfortunately, this is not the case for stop-and-go operation where the table is successively driven degree-wise with holding every position for some time, like in the angular dependence measurements in section 8.3. For some reason that has yet to be investigated, the start and stop moments are susceptible to stepping errors - even when the motor is engaged at all times - that the encoder does not detect. In this operation mode, the motor gains an angular error of 0.1° per 146 steps of 1° step size (disengaging the motor after every step results in huge errors of more than 10° per 180°, depending on the step size, due to dropping out of holding torque). This error deviates for different step sizes. An error-correction routine was implemented in the rotation table control which simply rotates the table a tiny little bit in the opposite direction whenever the angular error exceeds 0.1°. Thus the angular uncertainty of the rotation table in operation is ±0.1°.

Since the software-side error correction is more of a workaround than a solution to the problem, some adjustments should be made on the hardware side. A possible improvement in positioning uncertainty could be achieved by installing a gear between motor and sprocket. Replacing the plastic plates by more stable ones with a sophisticated ball bearing would help to reduce or eliminate mechanical tolerance.

7.4 Light sources

The measurements that were part of this thesis are conducted with different light sources, which are introduced and described in the following.

7.4.1 The pulsed LED

The pulsed blue LED[25] radiates light omnidirectional with a centre wavelength of 461 nm. It is adjustable in intensity and pulse repetition frequency. Both factors influence the spectral width, which lies between 29 nm (low optical power) and 39 nm (high optical power) [30]. The LED was mostly used for setup calibration and first test measurements, because the monochromator was not operable at the beginning of the measurement phase.

7.4.2 The Xe-lamp and the monochromator

The Xe-arclamp[26] provides a very broad light spectrum ranging from 200 − 2500 nm. With condenser and lens optics inside a black tube, the light is coupled into a monochromator[27], with which any desired wavelength within a range of 200 − 900 nm (due to grating specifications) can be selected from the lamp spectrum. The spectral width of the selected wavelength is adjustable with an optical slit at the monochromator exit, with a minimal spectral width of ±2.5 nm around the selected wavelength [31]. Both hardware components are

[25] Picosecond pulsed diode laser driver PDL 800-B with PSL 450 pulsed LED by PicoQuant.
[26] LSH102 lamp housing equipped with a 75 W LSB511 Xe bulb by LOT QuantumDesign.
[27] MSH 300 with variable slits and MSG-T-1200-300 grating by LOT QuantumDesign.

mounted and fixed on a metal plate which has four height-adjustable rubber bases to ensure a level setup. At the monochromator exit, another black tube is installed to connect the monochromator to the opening at the Blackbox's side panel.

7.4.3 Fibre-optics characteristics

In all measurements, the light from the monochromator or LED output was coupled into a multimode optical fibre[28]. Since both sources provide sufficient light intensity, the coupling was simply done with an SMA adapter, leaving complex fibre coupling unnecessary. The other end of the fibre was connected to a lens collimator[29] mounted on the 3D scanner.

For QE measurements, especially fine-grided position scans, a constant spot size is necessary. But as the lens collimator is actually not designed for blue light from a multimode fibre, it produces a focusing instead of a collimation. This can be compensated by changing the light output position relatively to the PMT surface with the 3D scanner, which demands the exact knowledge of the focal distance, the spot size and the beam divergence. The most efficient way to measure this characteristics with the available equipment was to direct the beam onto the sensor of a digital reflex camera (without any objective), and take photos of it for several distances between the light output and the camera sensor. The camera was fixed on the breadboard, and the collimator was successively moved back and forth with the 3D scanner. Three of these photographs are shown in figure 7.4.

With the graphic program ImageJ, the intensity for any pixel could be extracted from the photographs, so that intensity profiles along a certain axis of the light spots could be drawn. For my purposes it was sufficient to take profiles along the horizontal and vertical axes through the centre of the spot. A plot of these profiles against the axial position and the distance from the output can be seen in figure 7.5 (since there are no significant differences visible in the horizontal and vertical profiles, only the horizontal ones are shown). As expected and already indicated by figure 7.4, the plot shows beam divergences on both sides of the focal plane. These will be denoted with negative (closer to the output) and positive (further away from the output) beam divergences Θ_{neg} and Θ_{pos} in the following.

The beam diameters d for each distance f were set to the full width of 10 % maximum[30] of the according beam profile. This was done for both the horizontal and vertical profiles. The smallest beam diameters $d_{\text{min,hor}} = 0.916\,\text{mm}$ and $d_{\text{min,ver}} = 0.904\,\text{mm}$ were found for a distance from the output, or focal distance, of

$$f_{\text{min}} = (94.45 \pm 1.00)\,\text{mm}\,,$$

where the uncertainty corresponds to half the step size of the measurement (photographs were taken every 2 mm). The mean value of the minimum beam diameter at the focal distance equals

$$d_{\text{min}} = (0.91 \pm 0.12)\,\text{mm}\,,$$

where the uncertainty corresponds to the up-rounded deviation between $d_{\text{min,hor}}$ and $d_{\text{min,ver}}$. The beam divergences $\Theta_{\text{neg,pos}}$ were obtained by fitting linear functions of the distance f to

[28] The FG050UGA custom made multimode fibre with 50 µm core diameter by Thorlabs for the wavelength dependence measurement, and the FG050LGA multimode fibre with 50 µm core diameter, also by Thorlabs, for all other measurements.

[29] 60FC-SMA-0-A7.5-01 lens collimator by Schäfter & Kirchhoff, collimated at 532 nm.

[30] In literature, the beam diameter is often referred to as the FWHM of the beam profile. But as can be seen in figure 7.4, not all beam profiles of my measurement are of the same steepness, so a rather conservative beam diameter definition of the full width at 10 % maximum seemed to be more appropriate.

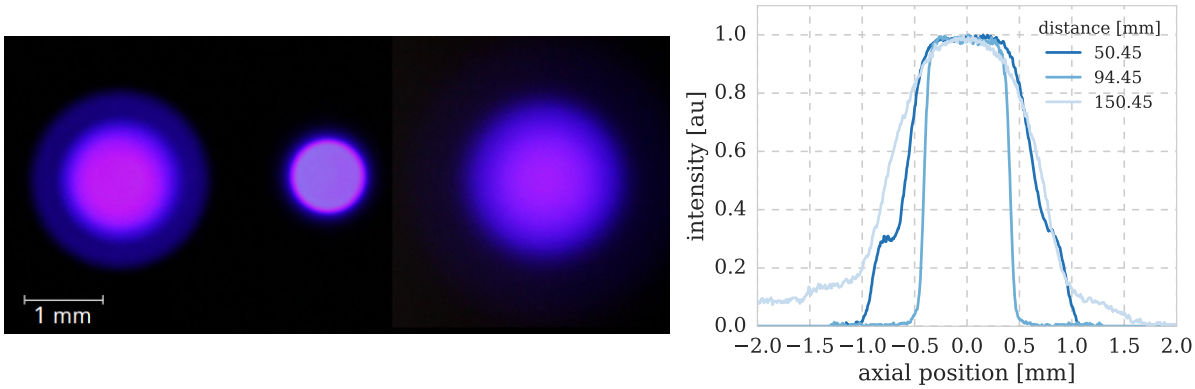

Figure 7.4: Left: Photographs of light spots produced by the lens collimator. Shown are three different pictures merged together for comparison, one taken in the focal plane (middle), one before (left) and one behind it (right). The measure in the lower left corner is not accurate but for displaying dimensions. The horizontal profiles of the displayed spots are shown in the right graph.

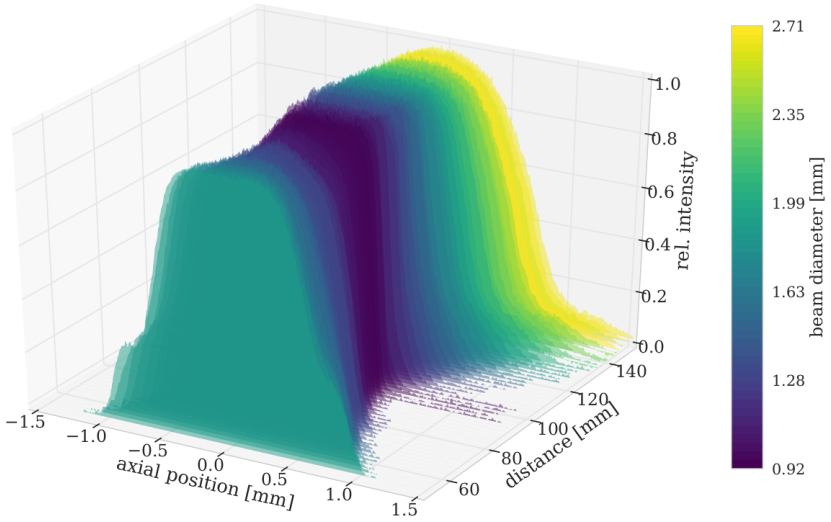

Figure 7.5: Beam profiles behind the lens collimator, plotted for distances between 50 and 150 mm from the output. Since the collimator does not perfectly meet the features of our light source and fibre, a focusing instead of a collimation occurs. The beam was directed onto the sensor of a camera and photographed for different distances between output and sensor. The beam profiles were obtained by extracting the intensity for each pixel (axial position, converted to mm) with the graphic program ImageJ. Shown are the horizontal profiles. Darker colours indicate smaller beam diameter.

the beam diameters d (where d is the average of d_{hor} and d_{ver}). With a particular slope m of the fit, the divergence is defined as[31]

$$\Theta = \arctan(m) \,.$$

With $m_{\mathrm{neg}} = 0.024$ and $m_{\mathrm{pos}} = 0.032$ was found:

$$\begin{aligned} \Theta_{\mathrm{neg}} &= 1.38\,^{\circ} \\ \Theta_{\mathrm{pos}} &= 1.85\,^{\circ} \end{aligned}$$

The uncertainties to the divergences calculated using Gaussian error propagation are less than $0.002\,^{\circ}$. By means of $\Theta_{\mathrm{neg,pos}}$ the spot size at every distance f from the light output can be calculated using

$$d_{\mathrm{spot}} = 2(f - f_{\mathrm{min}}) \cdot \tan\left(\frac{\Theta_{\mathrm{neg/pos}}}{2}\right) + d_{\mathrm{min}} \,. \tag{7.1}$$

The above investigations were conducted with the pulsed LED as a light source, which has a centre wavelength of 461 nm. The results are assumed to be the same for the monochromator with insignificant deviations at other wavelengths.

[31] Which can easily be derived from beam geometry.

8 Quantum efficiency measurements

The three different QE characteristics that were to be investigated in terms of this thesis were introduced at the beginning of chapter 7: The wavelength dependence, the angular dependence and the photocathode position dependence of the QE. This chapter provides a detailed description of the measurement setups, the working principles of the according Python controls, the actual measurement procedures and the results of all three investigations.

I conducted prior measurements in the early phase of this thesis at the Erlangen Centre for Astroparticle Physics (ECAP) which provided first insights in two of the above named QE characteristics. These measurements are presented in the first section of this chapter, to be later compared to the Münster QE test stand measurements.

8.1 Measurements at ECAP

The early phase of this thesis in winter 2015/16 was conducted at the ECAP to make some initial investigations concerning the wavelength dependence and angular dependence of the QE. These measurements were conducted with a setup shown in figure 8.1. Most devices used in the setup are similar or older versions of the devices deployed in the new QE test stand, which are described in chapter 7. Monochromatic light from the Xe lamp[32] and the monochromator[33] was fed through an opening in the black box, which was equipped with an iris to adjust the light intensity. The beam was directed onto the centre of a PMT, which was mounted on a rotation table in a way that the rotation axis coincided with the PMT centre. The incident angle of the light could thus be changed by rotating the PMT, whereas the incident point remained the same. The PMT current was recorded with a picoampere meter[34] placed outside the box next to the PMT's HV supply.

For acquiring the reference current, the box had to be opened to place a photodiode[35] in the light beam, and opened again to take it away afterwards. Since the picoampere meter had one input only, it had to be connected to the photodiode cable for the reference measurement and swapped back to the PMT cable to continue recording the PMT current. This rather complicated procedure was improved in the new QE test stand, as is described in section 8.2. A shutter inside the monochromator allowed for interrupting the illumination to acquire PMT and photodiode dark currents[36].

The QE was calculated from the data according to formula (6.2). Dark currents have been averaged and reference currents have been interpolated over the measurement time.

The wavelength dependence measurement was conducted with a Hamamatsu R12199-02 PMT by illuminating the PMT centre under normal incidence only, so no rotation was involved. The measured QE plotted against the wavelength is shown in figure 8.2. The shape of the QE in the upper plot is in good agreement with the prediction in section 6.2.3 as well as with the manufacturer's information in [32]. The little kink in the blue curve at about 640 nm is considered a measuring error.

The focus of this measurement was not only on determining the wavelength dependence

[32] Same model as in section 7.4.2.
[33] MSH301 by LOT QuantumDesign.
[34] Model 487 by Keithley.
[35] Type S6337-01 by Hamamatsu.
[36] For an explanation of the dark current see section 5.4.

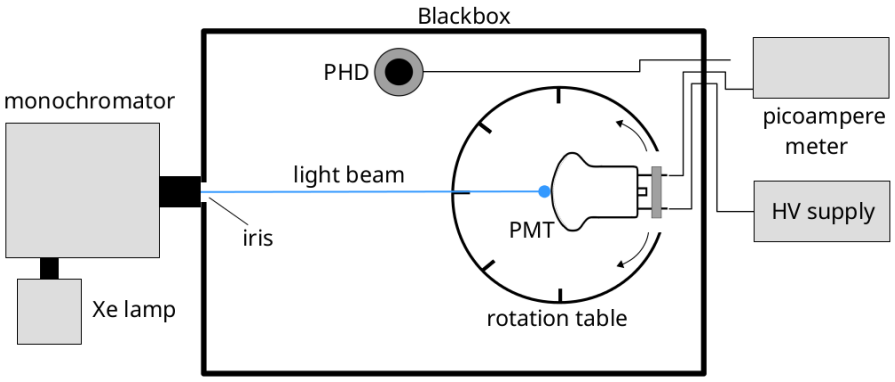

Figure 8.1: Scheme of an early version of the QE test stand at the ECAP. Light from the Xe lamp and the monochromator was fed through an opening in the black box and directed onto the PMT, which was mounted on a rotation table. An iris at the light opening could be used to adjust the light intensity. A patch panel at one side of the black box allowed for connecting the PMT to a picoampere meter and a HV supply outside the box. The photodiode is not connected in this picture which is explained in the text.

but also on the effect of different high voltage (HV) polarities on the measured QE[37]. The blue QE spectrum in figure 8.2 was measured with positive, the orange spectrum with negative HV with a value of 300 V. The measurement was conducted without taking standard deviations alongside the data points. The displayed error bars correspond to the absolute QE uncertainty of 1 % that is characteristic to the ECAP setup according to [33].

At first glance, the QE seems to be independent from the HV polarity. A closer look reveals that the positive HV QE is actually slightly higher than the negative HV QE, as the 25x zoom window in the plot indicates. To visualise this, the positive HV QE is plotted relative to the negative HV QE in the lower plot of the figure, where in fact the positive HV QE is higher for a large wavelength range. The rapid fluctuations at the very beginning and end of the spectrum result from dividing very small values by very small values and are considered insignificant.

The fact that the QE measured with positive HV is higher than the one measured with negative HV is in agreement with the assumptions made in section 6.1, although the effect is very small and would probably have no measurable impact on most PMT studies.

For measuring the angular dependence of the QE, the PMT was rotated successively to change the incident angle of the light on the PMT centre. The measured QE plotted against the incident angle is shown in figure 8.3. At first glance the curve does not seem to have any resemblance to the prediction in section 6.2.4. The lack of symmetry in the plot is caused by misalignments in the setup due to PMT mounting constraints and therefore improper positioning possibilities. By taking only the negative angular range into account, the curve actually does look similar to the prediction in figure 6.9, but with an 'ear'-like efficiency excess feature between about $-30°$ and $-60°$ that is missing in the prediction plot. Although the scan resolution is very low because the different angles had to be adjusted by hand, these 'ears' are assumed to be real QE features, probably caused by light that is back-reflected from the nonuniform inner structure of the PMT. The back-reflection that was considered in the prediction, however, is calculated under the assumption of a completely

[37] For an explanation of the positive and negative HV operation modes see section 6.1.

flat and uniform inner structure. This is probably the reason why the measured QE shows 'ears', and the theoretical absorption does not.

The reproducibility of the above observations and the investigation of their origins is to be tested in the new, more sophisticated QE test stand, which is described in the following sections.

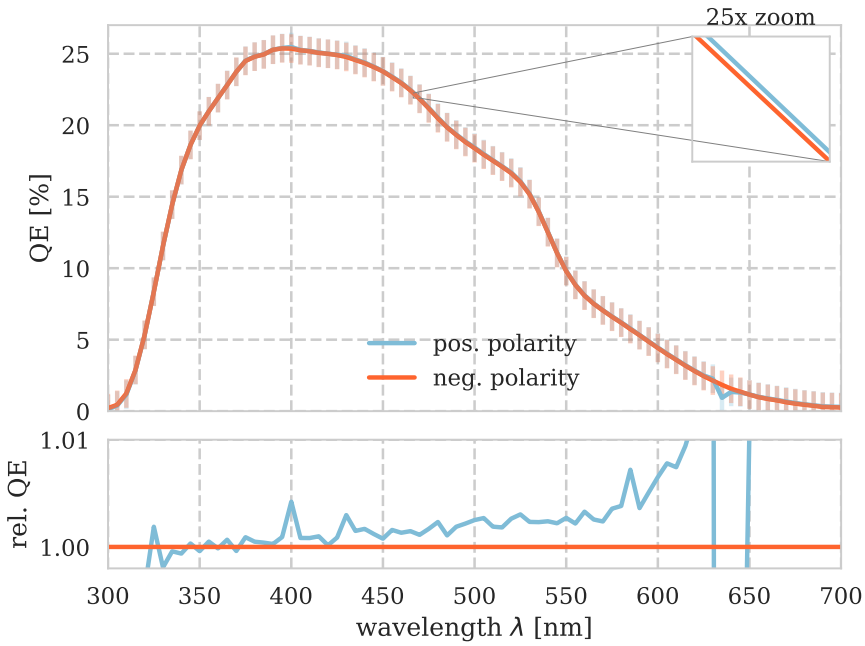

Figure 8.2: Wavelength dependence of the QE as measured with the ECAP setup in 2015, for centre illumination with $\theta = 0°$. The upper plot shows the QE spectra for positive (blue) and negative (orange) HV polarity with a value of 300 V. The small kink in the blue curve at about 640 nm is assumed to arise from a measuring error and is not a real feature of the QE. Error bars correspond to the absolute 1 % QE uncertainty characteristic to the ECAP setup [33]. The lower plot shows the QE measured with positive HV relative to the one measured with negative QE.

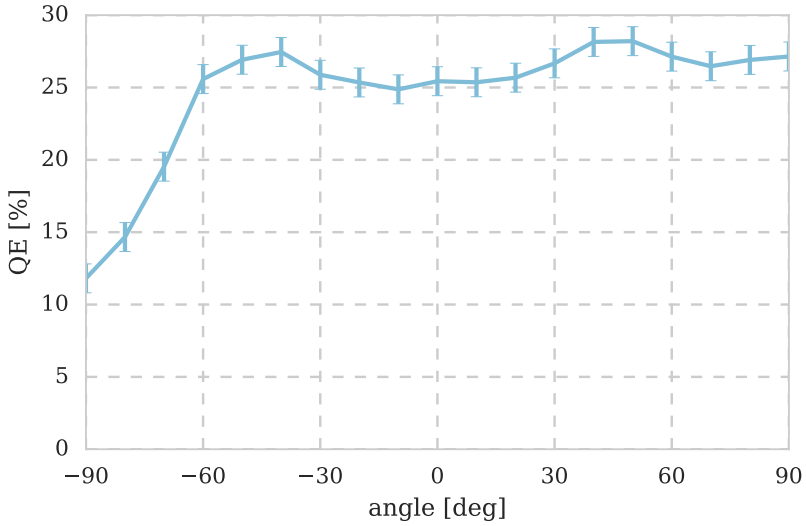

Figure 8.3: Measured angular dependence of the QE of a Hamamatsu R12199-02 PMT at a wavelength of $\lambda = 400$ nm. The measurement was conducted with the ECAP setup in 2015. Error bars correspond to the absolute 1 % QE uncertainty characteristic of the setup [33].

8.2 Wavelength dependence

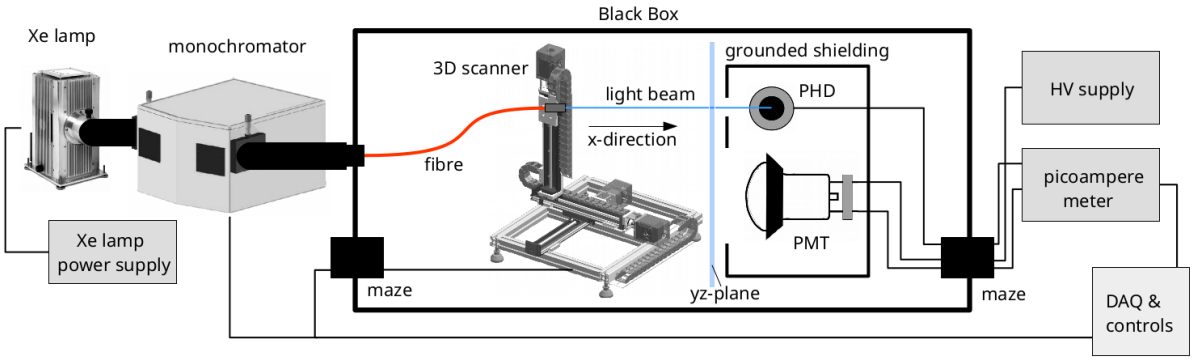

Figure 8.4: Schematic drawing of the wavelength dependence setup. Light from the monochromator is coupled into an optical fibre which is attached to the 3D scanner, so that the coordinates of the output point of the light can be changed to reach both the PMT and the photodiode. In this example, the light is oriented towards the latter which measures the reference photocurrent. Both detectors are surrounded by a grounded aluminium box (with circular openings at the position of the detectors) for electromagnetic shielding. The output currents are acquired with the picoampere meter outside the Blackbox.

This section is about the investigation of the wavelength dependence of the QE conducted with the new QE test stand in Münster. The setup for the corresponding measurements is shown in figure 8.4. Light from the monochromator at 470 nm was fed into the Blackbox and coupled into an optical fibre. The fibre was attached to the lens collimator that was mounted on the 3D scanner, so that it could be moved within the scanner range[38]. The collimator featured a fixed output direction in positive x-direction towards the yz-plane. The PMT and the photodiode (PHD) were placed at defined positions facing the negative x-direction. Both devices were surrounded by a grounded aluminium box for electromagnetic shielding (with circular openings at the positions of the devices) and were connected to the picoampere meter[39] and the HV supply, which were placed outside the Blackbox. The scanner and the monochromator were controlled by the QE test stand Python script.

By means of the scanner, the light beam was directed onto the PMT centre under normal incidence. The spot size was of no significance for this measurement, so the distance between the light output and PMT could be chosen freely to ~ 150 mm (which corresponds to a spot size of ~ 2.7 mm according to formula (7.1)). The wavelength was then successively changed with the monochromator in a range of $300 - 700$ nm with a step size of 5 nm. For every step the PMT current was acquired together with a timestamp. Before and after the measurement, the same was done for the photodiode to obtain reference spectra. Dark current values were obtained by directing the light to a position far away from both detectors, also before and after the PMT current measurement. Both the dark current and reference data were interpolated over measurement time.

The wavelength dependence measurement was conducted for the Hamamatsu R12199-02 PMT[40] with a voltage of +200 V. The QE was calculated using formula (6.2). The pho-

[38] For the setup and functionality of the 3D scanner see section 7.2.
[39] Model 6482 by Keithley.
[40] The Hamamatsu R12199-02 used in the Münster measurements is not the same as the one used in the ECAP

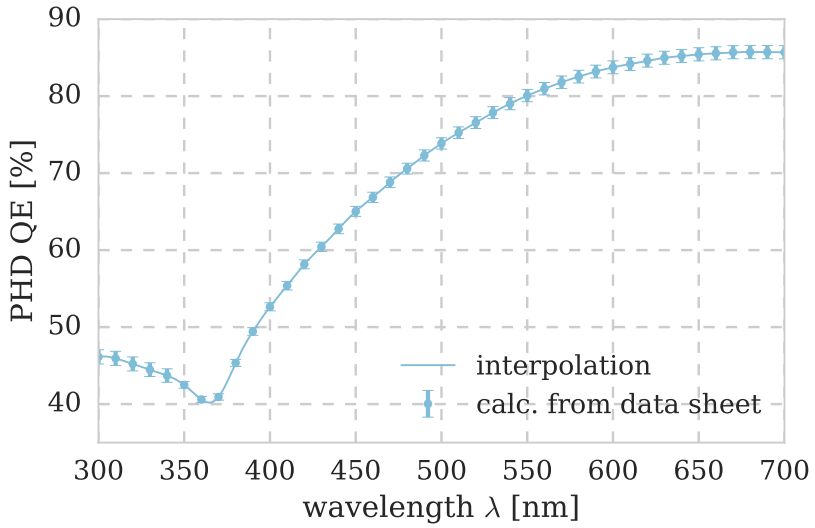

Figure 8.5: Quantum efficiency of the photodiode against the wavelength. The QE values were calculated from responsivity values given on the calibration report [34].

todiode QE values needed for the calculation of the QE were extracted from [34] and are plotted in figure 8.5. The resulting QE plot is shown in figure 8.6.

For wavelengths larger than about 400 nm, the QE shape follows the prediction of section 6.2.3 and is in agreement with the previous ECAP measurements in section 8.1. For smaller wavelengths however, the QE has a peculiar shape and is highly erroneous. The most obvious reason for such a behaviour is a setup component that cuts off high-frequency light, which after some investigation was found to be both the optical fibre and the lens collimator. This has been tested by comparing the output spectrum behind both devices to the spectrum directly behind the monochromator. These spectra, which are shown in figure 8.7, clearly reveal that the PMT does not receive any light below about 320 nm, even though the lamp provides light in that range. Another problem is that the measurement errors themselves are overrated due to an interfering signal that also compromised the angular dependence measurements and is described in more detail in section 8.3. The actual absolute standard errors of the PMT photocurrent are assumed to be about one order of magnitude smaller than the measured ones[41], which would cause a noticeable decrease in the displayed QE errors.

The maximum QE for centre-illumination was stated by the manufacturer to be 25 % at a wavelength of 390 nm in [32]. This is in agreement with the measured data, although despite of the large error bars for this wavelength one could argue that the actual maximum QE might even be slightly higher, as indicated by figure 8.6.

With the theoretical data shown in figure 6.9 and the measured QE, the conversion coefficient $P_{\text{conv}}(\lambda)$ can be calculated according to formula (6.23). The resulting plot is shown in figure 8.8. Due to the hardware and measurement uncertainty issues mentioned above, this plot is not very significant in the low-QE regions at the beginning and end of the spectrum,

measurements. Slight variations in certain characteristics from PMT to PMT, even for the same model, are acknowledged by the manufacturer, which might explain possible QE deviations from the ECAP measurement.

[41] Because the setup and measurement principle is very similar to the position dependence measurements in section 8.4 where significantly smaller errors of the order of $5 \cdot 10^{-13}$ A have been measured, the actual standard errors are assumed to be of the same order of magnitude.

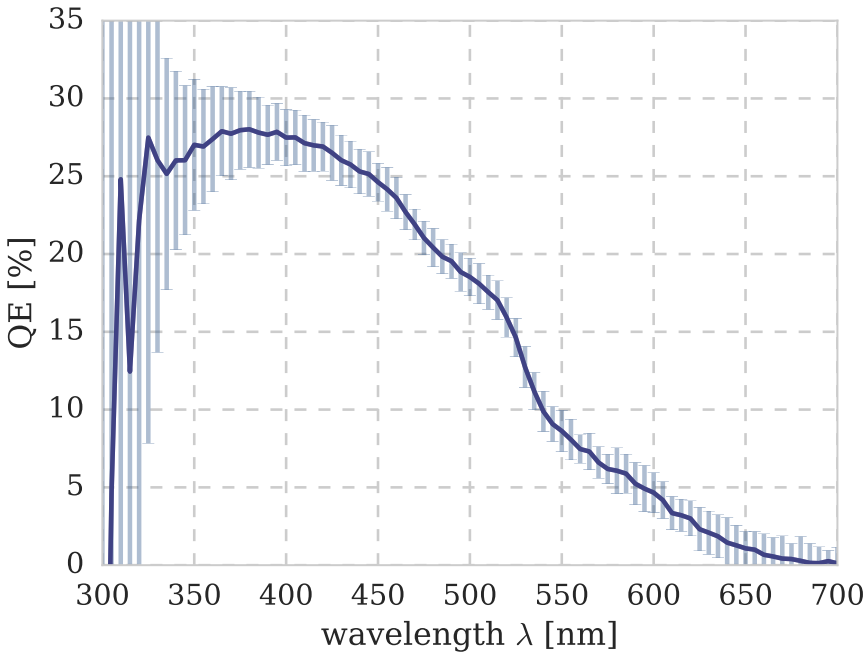

Figure 8.6: Wavelength dependence of the QE for the Hamamatsu R12199-02 PMT, for centre illumination with $\theta = 0°$. The large error bars for small wavelength arise from bad statistics due to an unexpectedly high cutoff wavelength of the optical fibre and the lens collimator.

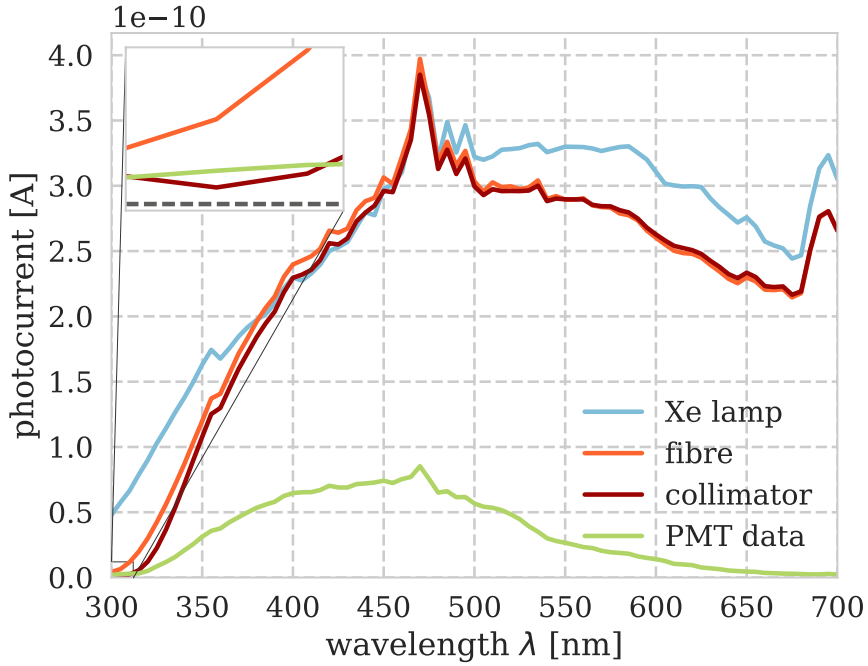

Figure 8.7: Spectra measured with the photodiode directly at the output of the monochromator (blue) which represents the actual lamp spectrum, behind the fibre (orange) and behind the lens collimator (red). The lamp spectrum was scaled up for better visibility. The curves are corrected for the QE of the photodiode (see fig. 8.5). The PMT current (green), also measured behind the collimator, is shown for comparison.

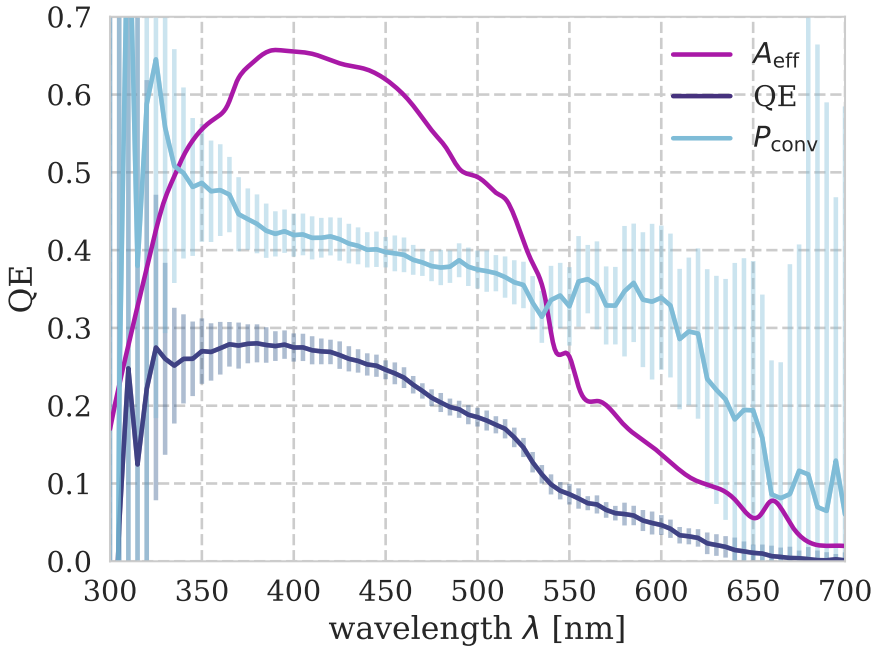

Figure 8.8: The conversion coefficient $P_{\text{conv}}(\lambda)$, calculated with the theoretical absorption from section 6.2.3 (pink) and measured QE (purple) from figure 8.6. The large error bars arise from bad statistics as explained in the text.

which is indicated by the large error bars in the plot. Still, for wavelengths between at least 400 nm and 550 nm the curve of P_{conv} is considered representative. P_{conv} will later be used to compare the results of the angular dependence measurement to the respective prediction; see section 8.3.

Conclusions

Altogether, the wavelength dependence setup seems to suit its purpose in general. With improvements on the setup concerning the shielding from interfering signals, it is assumed to allow the measurement of the wavelength dependence of the QE with even better significance than at the ECAP setup. Another necessary improvement is the installing of another optical fibre, or by finding out why the installed one, which is designated for wavelengths from 250 − 1200 nm, did not work the way we expected it to. Furthermore, a reflective collimator which was available for the measurement but has not been used for several reasons concerning spot size and beam divergence adjustments, could be installed in the setup after some commissioning to hopefully reduce light losses in the problematic high-frequency region.

Another option would be to forego light conduction altogether by placing the PMT directly behind the monochromator coupling like in the ECAP setup, so that neither the scanner nor the fibre and collimator would be part of the setup anymore. A beam splitter in the optical path could direct some of the light onto the photodiode for reference.

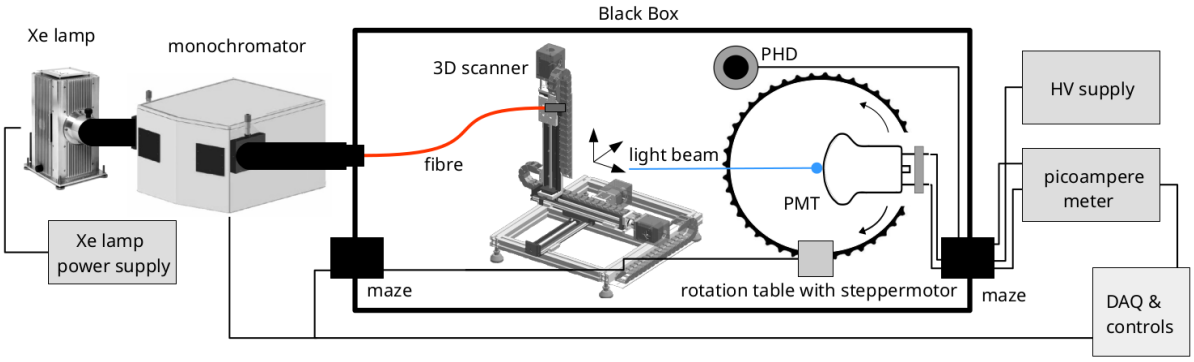

Figure 8.9: Schematic drawing of the angular dependence setup for the QE measurements. Monochromatic light is used to illuminate one point of the photocathode under different angles that can be chosen by means of the rotation table. Both the PMT and the photodiode are surrounded by aluminium boxes for electromagnetic shielding (not in the picture).

8.3 Angular dependence

The measurements for the QE dependence on the incident angle of the light were conducted with a similar setup as for the wavelength dependence measurements, as can be seen in figure 8.9. Light from the monochromator was again coupled into an optical fibre with the lens collimator at its end, which could be moved around with the 3D scanner. The photodiode for reference measurements was set in a fixed position. The PMT, however, was mounted on the rotation table in such a way that the centre of the photocathode coincided with the table's rotation axis[42], like in the ECAP setup. The incident angle of the light could thus be changed by rotating the PMT, whereas the incident point remained the same. The PMT was held by a broad rubber clamp on a mounting post to prevent misalignments. A string with a plummet suspended from the Blackbox's ceiling marked the exact centre of the rotation table, which allowed very precise positioning in contrast to the ECAP setup. Another advantage over the ECAP setup was that the different angles did not have to be set by hand, but by a stepper motor that actuated the rotation table. The motor and scanner controls are part of the QE test stand Python script. Three scan point locations for the scanner had to be defined: The position of the photodiode, the position of the dark current measurements, and the PMT centre. The distance of the light output to all these points was kept constant at $\sim 237\,\text{mm}$ at all times. For this distance, the spot had a diameter of $\sim 5.50\,\text{mm}$ as determined using formula (7.1).[43] The ro-

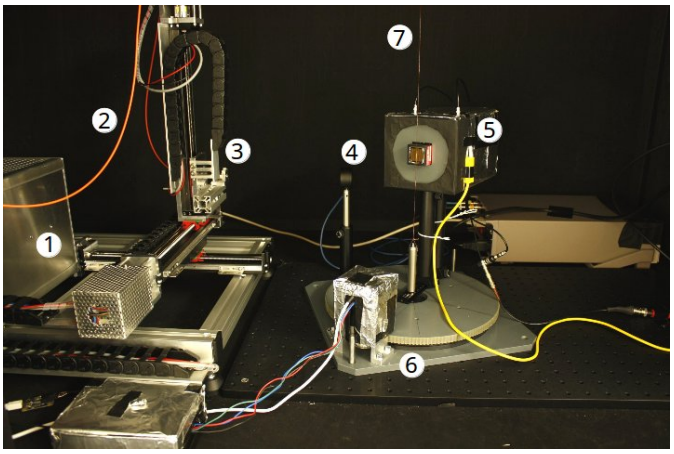

Figure 8.10: Photograph of the angular dependence setup inside the Blackbox, with the scanner (1), the optical fibre (2), the lens collimator (3), the photodiode (5), the Hamamatsu R7600u-200 PMT with base inside a grounded shielding box (5), the rotation table (6), and the plummet that is installed over the centre of the rotation table to ensure exact positioning.

[42] For the functionality of the rotation table see section 7.3.

[43] The dimensions of the rotation table are too big to position it closer to the 3D scanner. But since the spot

Table 8.1: PMTs used for the angular dependence measurements of the QE.

designation	type	applied potential
Hamamatsu R12199-02	hemispherical, ∅3"	+200 V
Hamamatsu R7600U-200	flat square, 1"	+105 V

tation table was rotated so that the photocathode was illuminated under −90°, and then rotated step-wise in the other direction, until the photocathode was illuminated under 90°. This 180° rotation was performed in steps of 1.0°. At every step, the PMT current was recorded for several wavelengths that were selected with the monochromator. Every 15° as well as before and after the measurement, the scanner moved to the photodiode and dark current positions so that reference and dark currents could be acquired, respectively. The wavelengths chosen for this investigation are 400 nm, which is the wavelength of maximum QE[44], as well as 470 nm and 540 nm for comparison.

The angular dependence measurement of the QE was conducted for the hemispherical PMT that was also used in the wavelength dependence measurement, and a flat square PMT which is shown in the setup photo in figure 8.10. Both are listed in table 8.1. The QE was calculated according to formula (6.2) and was plotted against the incident angle of the light, as shown in figure 8.11 for the hemispherical and in figure 8.13 for the flat PMT. Both plots will be discussed in the following.

First of all, the shape of the QEs were expected to be approximately symmetric, because the photocathodes of all tested PMTs are assumed to be symmetric[45]. Both PMTs showed this angular symmetry of the QE for all measured wavelengths[46]. The rather uneven curves for the angular dependence measured at a wavelength of 400 nm were caused by the optical fibre, which was at the lower edge of its transmission in this wavelength. That means that the beam spot had significantly lower intensity and thus worse statistics than for the other two tested wavelengths. Further it is important to note that the measurement errors shown in the plots should be considered overestimated, because the laboratory environment was compromised with a large low-frequency sinusoidal interfering signal on the measurement day which we were not able to suppress or identify the source of. So the PMT, acting as an antenna, captured this interference on top of the actual signal. Every data point is a mean value of 100 individual picoampere current measurements, so that the relatively uniform sinus got averaged out. The standard deviation of each data point, however, is huge due to this interfering, and the standard error ($\sigma/\sqrt{100}$) is also still very large. The standard error

size is not significant for this measurement, larger distances between output and PMT are not a problem. Thus it was sufficient to determine the output-PMT distance only roughly by means of a meter stick.

[44]The wavelength dependency measurements in sections 8.1 and 8.2 revealed a maximum of the QE for about 390 nm (consistent with reference [32]). The statistic gets significantly low towards smaller wavelengths though, due to setup constraints that are explained later in this section. So 400 nm seemed to be a good compromise.

[45]With visual judgement, the entrance window of the hemispherical PMT is rotationally symmetric around its centre, and the entrance window of the flat squared PMT is symmetric along several axes through its centre. For all PMTs, the photocathode is assumed to be evaporated uniformly onto the inside of the window.

[46]Both figures are a combination of two measurements each. In the first run, the curves showed asymmetries on the right-hand edges of the plots for angles larger than about 70°. The cause for this behaviour was found to be a hardware constraint in the form of an electromagnetic shielding box that disrupted the setup in its rotation on one side of the rotation table, which made the PMTs themselves rotate on their mounting posts and distorted the incident angle. In the second run, the box was removed and the range of $60-90°$ was measured again for both PMTs.

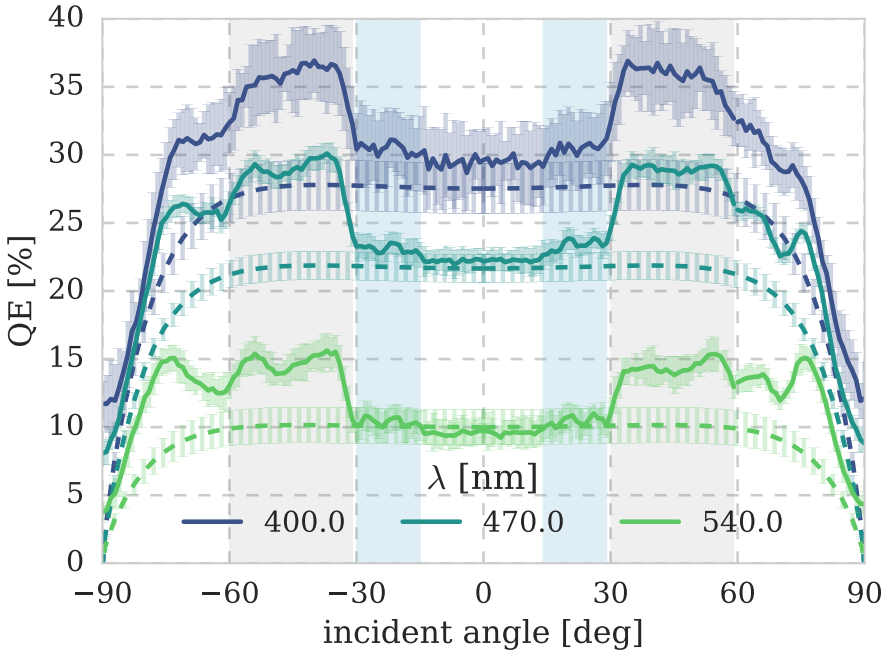

Figure 8.11: Angular dependence of the QE of the hemispherical R12199-02 PMT for three different wavelengths, for centre illumination of the PMT. The Plot shows the measured QE (solid lines) as a function of the incident angle of the light. The grey areas indicate the angles under which incident light that is transmitted into the PMT is assumed to hit the reflective coating on the inner surface. The blue areas highlight features that are assumed to arise from the structure of the focus electrode. The QE prediction (dashed lines) for each wavelength was calculated with the theoretical effective Absorption A_{eff} from section 6.2.4 and the conversion coefficient P_{conv} obtained in section 8.2, using formula (6.1). Error bars are calculated using Gaussian error propagation and shaded for better visibility.

of the dark current is compromised even more, because it only 'consists' of 10 individual picoampere measurements for each point. They have been down-scaled so that the relative standard error would be the same for data and dark current points, before calculating the QE error with Gaussian error propagation. The plotted QE error is thus assumed to be overrated and does not represent the precision of the displayed data correctly.

The measured QE curves for the hemispherical PMT in figure 8.11 are relatively symmetric, however, at first appearance they seem not to follow the predicted angular dependence in figure 6.10 (the dashed curves in the plot represent the prediction corrected with P_{conv}; they will be discussed later in this section). For all three wavelengths, the QE shows 'ears' for both negative and positive angles between about 30 °and 60 ° (indicated with grey areas in the figure), whereas the middle sections are flat. Similar results were obtained in the ECAP measurements, recalling figure 8.3. As stated in section 8.1, a possible explanation for this lies in back-reflection of light that is transmitted into the tube. The prediction in section 6.2.4 considers back-reflection from the inside metal structure of the PMT, but under the assumption that this structure is homogeneous and therefore increases the QE in a uniform way. The insides of the tested hemispherical PMT, however, are more complex. The surfaces of the glass tube feature a highly reflective inner coating that connects the photocathode to the electric potential. If light is incident under a large angle, it may hit the reflective coating

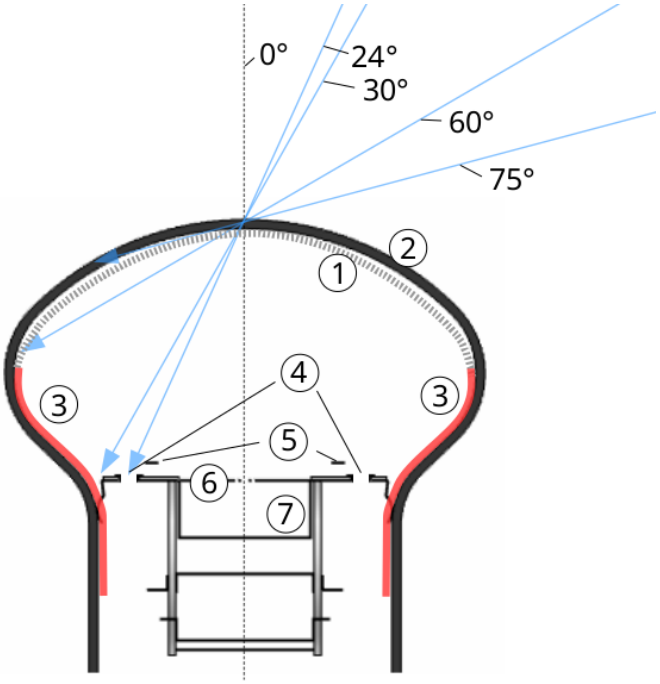

Figure 8.12: An accurate technical drawing of the inside of a Hamamatsu R12199-02 PMT with light that is incident under different angles and thus hits different parts of the PMT's inner structure. Shown are the photocathode (1), the glass tube (2), the reflective coating (3), the connector holes (4), focus electrode wires (5), the focus electrode (6), and the first dynode (7). The reflective coating and the photocathode have been added by visual judgement as indications and probably do not represent the locations perfectly correct, though. Picture courtesy of [35] and modified.

which back-reflects more light than the focus electrode, which could explain the increase of the QE for larger angles. This principle is visualised in figure 8.12. The graphical analysis reveals that the edges of the reflective coating might actually coincide with incident angles of 30 ° and 60 °, which would confirm the assumptions. The edges of the reflective coating and the photocathode are added by visual judgement to the otherwise accurate PMT drawing; a precise knowledge of the actual edges could not be obtained.

A closer look at the plot reveals that the QE is still noticeably higher for even larger positive and negative angles between about 60 ° and 75 °, than in the central section. Light entering under most of these angles does not hit the reflective coating any more, so the reason must be something else. A similar feature can be found in the theoretical PMT absorbance plot in figure 6.8c, where a peak for about the same angle is visible. However, this is not assumed to be caused by the same effect as for the measured feature, since it appears for completely different wavelengths compared to theory. Polarisation could play a role in terms of unwanted birifringence in the optical fibre, which is not assumed to have such a large impact though. It could also have something to do with effective photocathode thickness: Under normal incidence, the light's path through the photocathode material is very short. With larger incident angles, this path increases. That means, on the one hand, that the light is more likely to be absorbed, on the other hand, that electrons have to overcome a longer distance and therefore are less likely to be ejected from the cathode. So there probably is a wavelength-specific effective photocathode thickness range with an ideal ratio of absorbed photons to ejected electrons. Light that is incident under angles between 60 ° and 75 ° might just experience this ideal thickness, which would explain the higher QE for these angles. However, this feature is not completely understood and needs further investigation in future studies.

The middle section in the range of 30 ° around the centre is also not really flat, but shows some interesting features at the very edges (blue background in the figure). These could be explained by having another look at the structure of the focus electrode that is shown in figure 8.12. The angular scan was performed along the axis through the centre and both

connection holes of the focus electrode. The holes may be indicated by small dips in the QE, whereas the broad wires next to them might produce small QE peaks due to scattered back-reflection. This assumption is consistent with the graphical analysis. Slight deviations in symmetry might arise from the fact that the scan axis was not fully aligned with the axis that goes through the two connector holes. The misalignment was in the order of just a few mms.

In section 8.2 the conversion coefficient P_{conv} was obtained from the wavelength dependence measurement. For the three investigated wavelengths in this section, the coefficients are $P_{\text{conv}}(400\,\text{nm}) = (41.9 \pm 2.8)\,\%$, $P_{\text{conv}}(470\,\text{nm}) = (38.4 \pm 1.8)\,\%$ and $P_{\text{conv}}(540\,\text{nm}) = (33.6 \pm 4.4)\,\%$. According to formula (6.1), the individual P_{conv} multiplied with the according angular dependencies of the theoretical effective absorption A_{eff} calculated in section 6.2.4, should provide QE predictions that can directly be compared to the measurements, which allows for quantifying the differences between experimental data and prediction. The according plot is shown in figure 8.11, where the predictions are drawn as dashed and the measurements as solid lines. It can be seen that in the middle region between $-30\,^\circ$ and $30\,^\circ$, the experimental and predicted curves are in very good agreement within uncertainties for all three wavelengths. These observations justify the assumption that the prediction is actually correct for the investigated R12199-02 PMT's centre region, which would indicate a sophisticated choice of parameters like refractive indices and photocathode thickness used for the calculations in theory. The fact that the middle region is consistent with the prediction makes it further unlikely for the 'ears' to be an intrinsic photocathode feature, rather than a result of back-reflection from the inner PMT structure.

The angular dependence of the QE of the flat R7600U-200 PMT is drawn as solid lines in figure 8.13 for the investigated three wavelengths. The size of the error bars is decreasing towards larger positive angles because the interfering signal, that was mentioned earlier and is assumed to be responsible for the large errors in the first place, faded towards the end of the measurement, and has shown such fluctuations before.

All three QE curves show a relatively constant behaviour between $-50\,^\circ$ and $50\,^\circ$, and start to decrease for larger angles until dropping to zero for $90\,^\circ$. In terms of general QE shape, this behaviour is in very good agreement with the theory of section 6.2.4. For quantifying the differences, the QE predictions calculated with P_{conv} are shown as dashed lines in the plot. As can easily be seen, prediction and measurement are not consistent except for the largest wavelength. The reason for the deviations is the simple fact that the flat PMT is equipped with an ultra-bialkali photocathode, whereas the predictions are made for a standard-bialkali photocathode. Since the knowledge of photocathode composition and characteristics is not so easily obtained, as discussed in section 6.2.2, a prediction for ultra-bialkali photocathodes was beyond the scope of this thesis. Nonetheless, the qualitative resemblance between experimental data and prediction is undeniable.

However, the measurement contains a few noticeable features that can not be found in the theoretical curves. There are small local peaks in the QEs at about $85\,^\circ$ for both negative and positive angles. Since the manifestation of these peaks obviously decreases towards smaller wavelengths and is not at all visible for 400 nm, indicates them to be a wavelength-dependent feature. It could have arisen from the phenomenon that for a specific range of angles, the beam could actually run almost horizontally through a large area of the photocathode, which would have resulted in an rapid increase in QE. As the PMT is rotated further, the QE decreases again. Why this effect is wavelength-dependent in such a way is

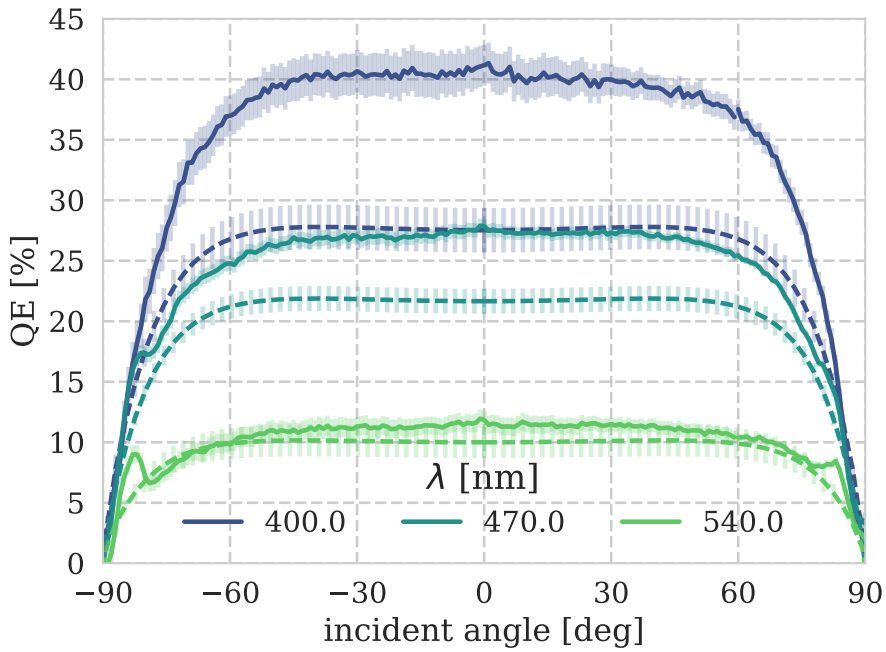

Figure 8.13: Angular dependence of the QE of the flat Hamamatsu R7600U-200 for three different wavelengths, for centre illumination of the PMT. The plot shows the measured QEs (solid lines) as a function of the incident angle of the light, as well as the QE predictions. Error bars are calculated using Gaussian error propagation. They decrease in size towards larger positive angles, which is explained in the text.

not yet completely understood. Another feature are the small peaks at 0° that are visible for all three wavelengths. The curves are also not as flat as their predictions. Both observations are assumed to arise from inner PMT geometry or inhomogeneous photocathode distribution, although visual judgement could not reveal any distinctive anomalies.

The maximum QE for the centre of this PMT is stated by the manufacturer as a little over 40 % for a wavelength of 400 nm [36], which is in agreement with the measurement.

Conclusions

The angular dependence setup of the QE test stand showed good performance and yielded high-precision results far beyond the capabilities of the ECAP setup. Thanks to more sophisticated mounting devices, wrong PMT positioning and other misalignments can almost completely be ruled out as potential sources of error. However, like in the wavelength dependence measurement, the setup is hoped to yield even better results with a proper electromagnetic shielding that has yet to be installed.

The measurements showed the expected reproducibility of the previous ECAP observations; the investigation of the hemispherical R12199-02 resulted in a similarly inhomogeneous QE. A comparison with the prediction from section 6.2.4, however, led to a further confirmation that the inhomogeneities are not caused by the photocathode itself but by the inner structure of the PMT, which seems to play an even larger role than initially expected. The inner structures of the PMT are investigated with more detail in the next section.

8.4 Position dependence

The previously described measurements revealed a large influence of the inhomogeneous inner PMT structure on the QE. Further insights in these observations are assumed to be obtained by investigating the photocathode position dependence of the QE. For this purpose the same setup as for the wavelength dependence investigations was used, which is schematically shown in figure 8.4. A photograph of the setup is shown in figure 8.14. The scanning procedure, which was controlled by a Python routine that is part of the QE test stand Python script, was more complex though. The script- and measurement procedure is explained in the following:

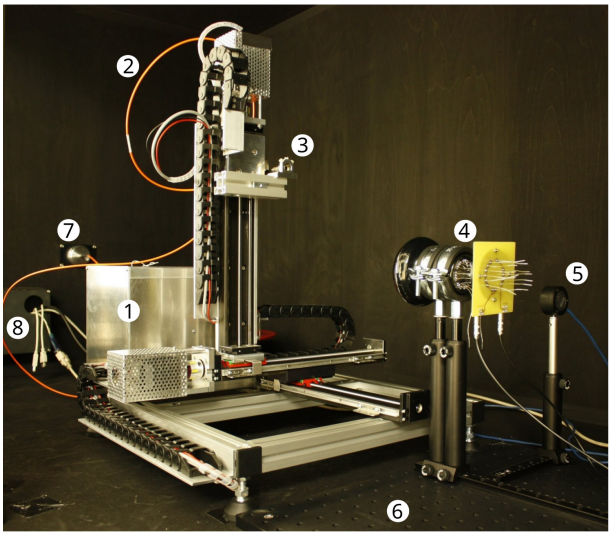

Figure 8.14: Photograph of the position scan setup inside the Blackbox, with the scanner (1), the optical fibre (2), the lens collimator (3), the PMT with base (4), the photodiode (5), the anodised breadboard (6), the monochromator coupling (7), and one of the photon mazes (8). The aluminium shielding box is not shown in this picture.

First, a square area of about $90 \times 90\,\mathrm{mm}^2$ in the yz-plane is defined which covers the whole PMT front. The centre of this area coincides exactly with the PMT centre[47]. This area is filled with grid points, where the distance between these points defines the scan resolution and can be chosen freely. The grid points represent the y- and z-coordinates of the scan relatively to the reference point of the corresponding scanner axis. From these coordinates the height h of the PMT surface relatively to the height at the maximum photocathode radius R_{cath} is calculated for every point using

$$h = \sqrt{R_{\mathrm{bulb}}^2 - (y^2 + z^2)},$$

where R_{bulb} is the PMT surface curvature radius, as visualised in figure 8.15b. The x-coordinate at each grid point is corrected with the corresponding value of h, ensuring the distance f between the PMT surface and the light output to remain constant at $f = (94.45 \pm 1.00)\,\mathrm{mm}$, which corresponds to the focal length of the beam, where the spot has its minimal diameter of $d_{\mathrm{min}} = (0.91 \pm 0.12)\,\mathrm{mm}$. A visualisation of the xyz-coordinates of a scan is shown in figure 8.15a. The light spot is then successively moved from one grid point xyz-coordinate to another, where at every point the PMT current is measured with the picoampere meter. The current is written to a data file together with the scanner position and a timestamp.

At the start and the end of each measurement, and upon the completion of every fifth full grid line, a dark current and reference measurement is performed. For this purpose, the light spot is first moved to a coordinate far away from both the PMT and PHD (so that neither of them 'sees' any light), and the dark current of both devices is recorded. Then it is moved to the centre of the PHD, and the reference current is acquired, much like in the other measurements. This is not only necessary to later calculate the QE, but also to monitor the stability of the light source, which usually decreases over the time of a measurement that can easily last for several days depending on the scan resolution. The dark currents usually are very stable. Together with a timestamp, both the dark currents and the reference current

[47] This is achieved by performing a sparse scan of the PMT first and determining the PMT centre from the data.

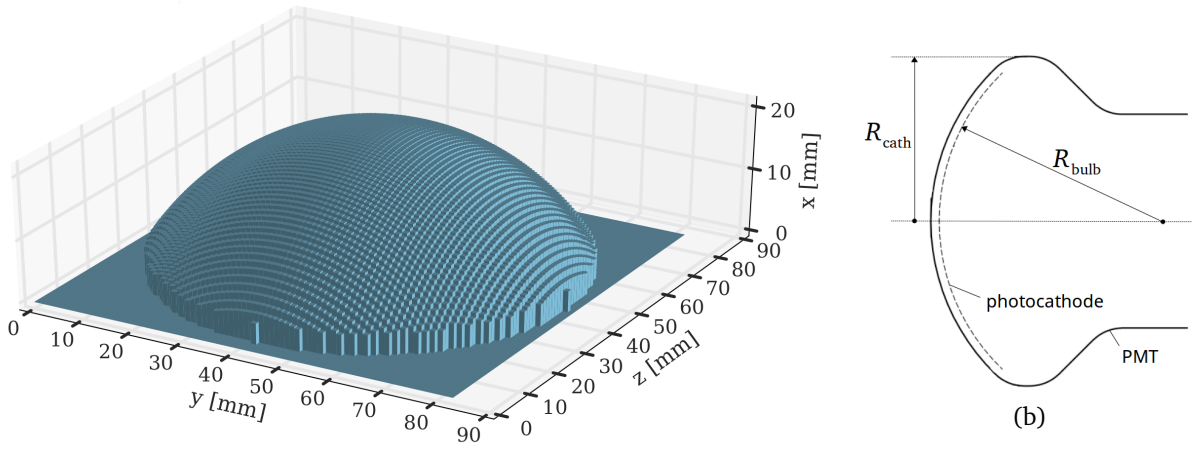

(a) (b)

Figure 8.15: **(a)** Map of the relative scanner position during a 3D scan. The PMT front sticks out of the yz-plane, where $x = 0$ applies to all positions beyond the maximum photocathode radius (by definition). Each bar represents one grid point of the scan, where its height represents the x-coordinate of the scanner to keep a constant distance between the light output and the PMT surface. **(b)** Side view of an hemispherical PMT. The bulb-shaped front has a radius of R_{cath} and a curvature radius of R_{bulb}.

Table 8.2: PMTs used for the position dependence measurements of the QE.

designation	type	applied potential
Hamamatsu R12199-02	hemispherical, ∅3”	+200 V
ET Enterprises Ltd. 9320KFL	hemispherical, ∅3”	+200 V

are written to a reference data file, and are interpolated over measurement time. A code excerpt of the program conducting the above explained procedures can be found in figure 10.2 in the appendix.

A position dependence scan was performed for the PMTs listed in table 8.2 for a wavelength of 470 nm. The QE was calculated from the collected data using formula (6.2), and was plotted as QE-yz-maps that are shown in figure 8.17 and 8.19. Both plots will be discussed in the following.

The Hamamatsu R12199-02 PMT was scanned with a scan resolution of 1 mm. At first glance, the plot resembles a false-colour photograph of the PMT front, whereas it actually shows the QE as a function of the y- and z- coordinates of the scan. The inner surfaces of the bulb-shaped front of the PMT are coated with a highly reflective metal layer that is used to connect the photocathode to the electric potential. In the plot, this coating appears as the yellow ring surrounding the focus electrode in the centre. For comparison see the technical drawing of the PMT front in figure 8.12, and the photograph of the focus electrode in figure 8.16a. The maximum QE values are found on this ring on both the left and right side. The focus electrode is easy to recognise as the light green circle with the rectangular shape in the middle, which is the entrance window to the PMT's dynode system. The material of the electrode is assumed to be less reflective with a more coarse surface, which results a lower effective QE. Even some of the more detailed structures can be found in the plot, for example the two connector holes at the coordinates of about (50, 150) and (87, 143) mm.

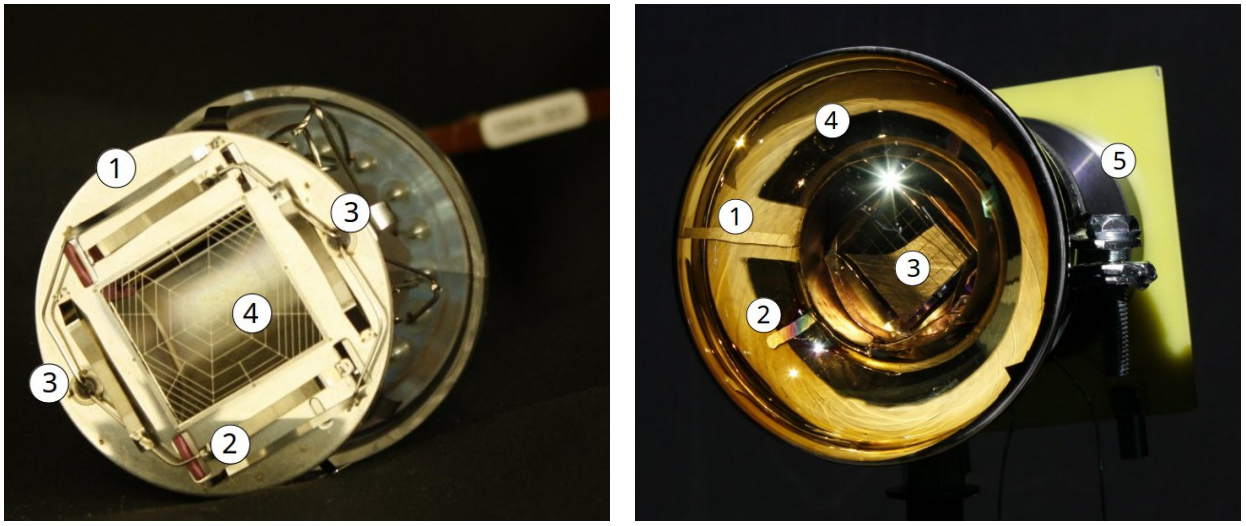

(a) (b)

Figure 8.16: **(a)** The inner life of a Hamamatsu R12199-02 PMT. The circular metal plate is the focus electrode (1) with the rectangular entrance to the first dynode (4) in its centre. The spiderweb-like wire structure is assumed to be for shaping the electric field, as well as the four broader wires (2) around it. These are connected and held by wires that lead through two holes (3) in the electrode and further to the inside of the PMT. **(b)** Front of the ETEL PMT with the photocathode contact strip (1), the focus electrode contact strip (presumably) (2), the first dynode (3) with a similar web-like structure as for the Hamamatsu PMT, the nonuniform reflective coating (4), and the base (5).

Figure 8.18 shows y- and z-profiles of the QE created from the same data used for the QE map in figure 8.17. Where the QE map might be more useful to visualise qualitative features, the profiles provide more insight when it comes to quantitative evaluation of the QE. For instance, it shows the rather large deviation in QE maximums between y and z direction, which is not so obvious in the QE map. This deviation is not explainable with visible features in the inner structure of the PMT, so it might be an actual photocathode feature that arises from inhomogeneous evaporation of the photoemissive material in the manufacturing process. An inhomogeneity of the reflective coating is also possible. The profiles further reveal that the small QE peak in the middle does not really coincide with the physical centre of the PMT, but is slightly shifted in z-direction. The glass at this point has some visible irregularities. To what degree these might be responsible for this little feature has yet to be investigated.

Altogether, the shape of the QE profiles are in agreement with the features observed in the angular dependence measurement that was conducted with the same PMT. In terms of quantity, the QE for centre illumination (averaged over the y- and z-profile values) was found to be $\sim 22.2\,\%$, which is also consistent with the other investigations and [32]. The absolute maximum QE variation is $\sim 10.6\,\%$ for the y-profile and $\sim 7.3\,\%$ for the z-profile.

The QE plot of the ET Enterprises Ltd. (which in the following will be abbreviated by ETEL) PMT, which was also scanned with a 1 mm scan resolution, is shown in figure 8.19. For better visibility it is drawn with a different colour map. Like for the Hamamatsu PMT, the plot reveals the entrance to the dynode system as a rectangular structure in the centre, and the focus electrode as a surrounding circle. The highly reflective conducting layer that connects the photocathode to the potential is divided in two parts for this PMT. For comparison see

the photo of the PMT in figure 8.16b (note that the QE map is back-to-front though). The highest QE value is reached around the wire that is assumed to be the contact strip of the first electrode. In this region, the coating is a bit tarnished, which can also be seen in the photo. If or why this might have such a big effect on the QE is not understood yet. The four spikes at the outermost part are real features where the reflective coating reaches over the edge of the photocathode. Altogether, the inner structures are less straightforward than for the Hamamatsu PMT, which results in the QE map to look a little ragged. This is also true for the QE profiles shown in figure 8.20. Most of the visible features are consistent with the QE map though. There is a little QE peak near the PMT centre just like for the Hamamatsu PMT, but again it can not be explained by visible judgement of the inner PMT structures.

The averaged QE for centre illumination is $\sim 20.3\,\%$ which is consistent with the manufacturers statement in [37]. The absolute maximum QE variations were found to be $\sim 9.39\,\%$ for the y-profile and $\sim 9.55\,\%$ for the z-profile, which makes the ETEL PMT to appear slightly less inhomogeneous than the Hamamatsu PMT.

Conclusions

The position dependence of the QE could be investigated in great detail for both PMTs. The high scanner accuracy and the small light spot size allowed for a scan resolution of 1 mm, which proved to be sufficient to observe even small details in PMT structure.

The results of the measurements are in agreement with the expectations and the other investigations in terms of a qualitative as well as quantitative analysis. A comparison of the measured QE structures with photographs of the actual inner structures provided further confirmation of the large influence of PMT inner structure and geometry on the QE.

Although the QE of the ETEL PMT showed smaller absolute QE deviations which might indicate more homogeneity, the Hamamatsu PMT provides much more symmetry in QE as well as inner structure. The advantages and disadvantages of both PMT's features thus are a matter of application requirements.

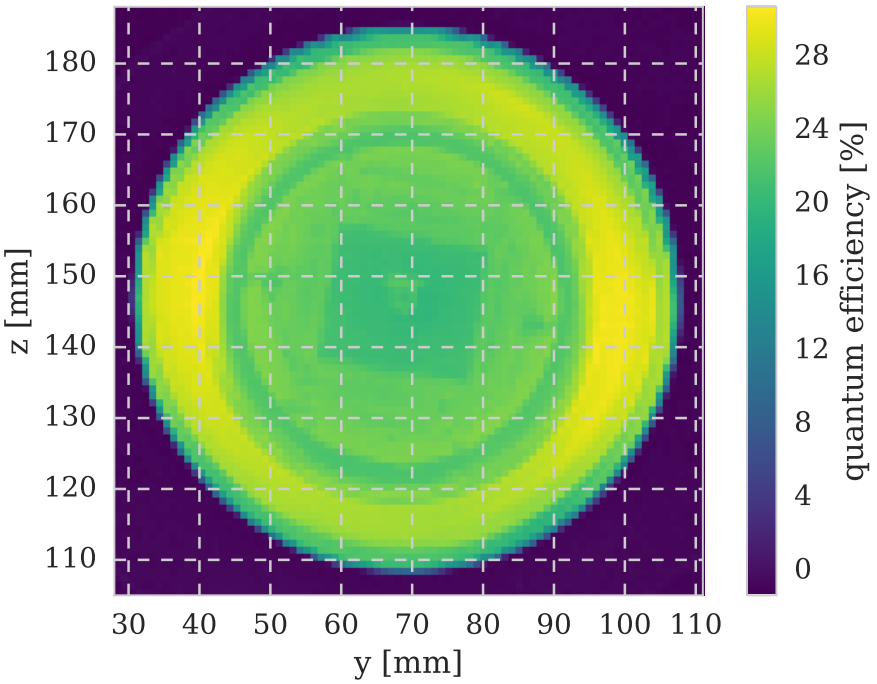

Figure 8.17: Position dependence of the QE for the Hamamatsu R12199-02 PMT. The plot shows the QE as a function of the y- and z- coordinates of the scans. The measurement was conducted with a scan resolution of 1 mm in both y- and z-direction. The QE is colour coded.

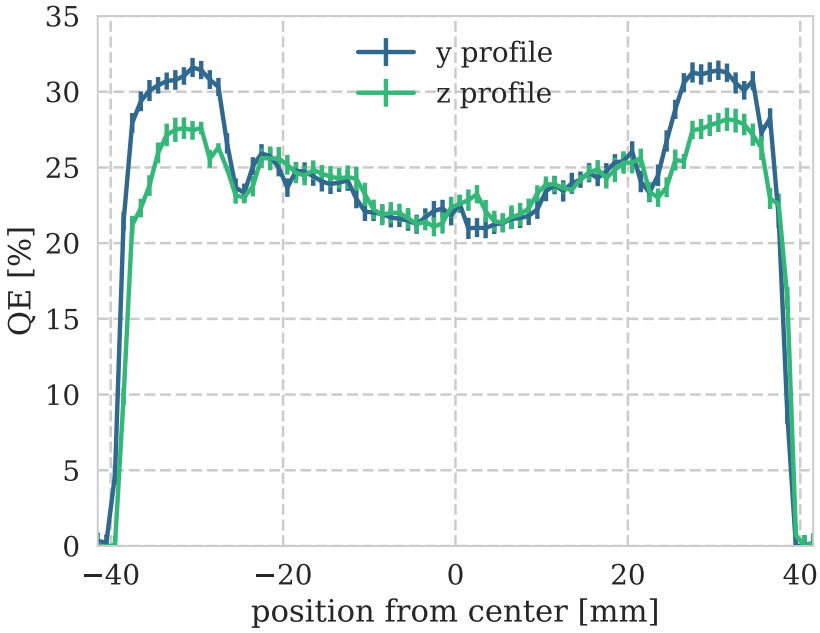

Figure 8.18: y- and z-profiles of the QE. Both profiles were sectioned through the PMT centre. Error bars were calculated with Gaussian error propagation.

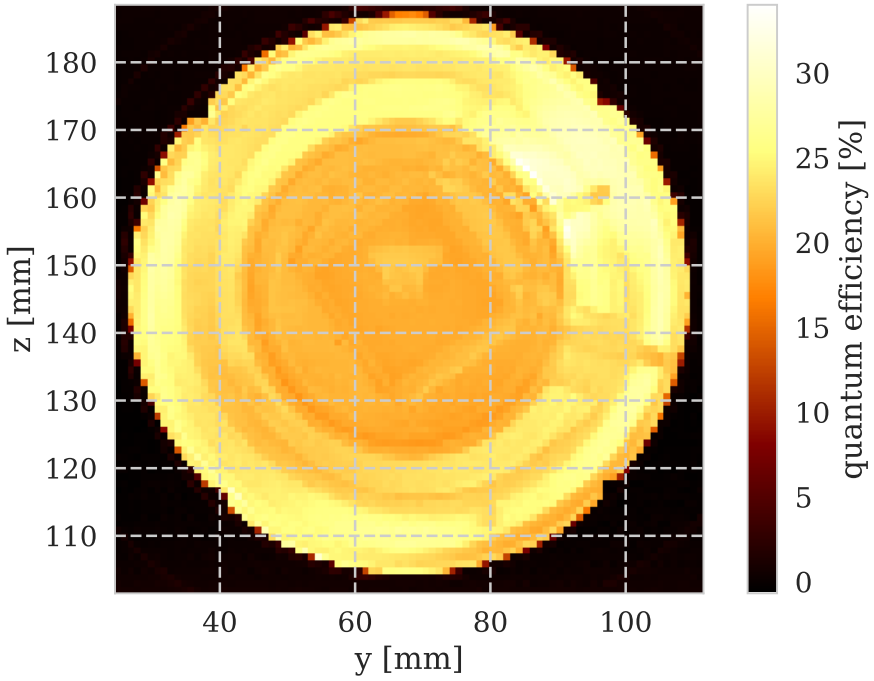

Figure 8.19: Position dependence of the QE for the ETEL 9320KFL PMT. The plot shows the QE as a function of the y- and z- coordinates of the scans. The measurement was conducted with a scan resolution of 1 mm in both y- and z-direction. The QE is colour coded.

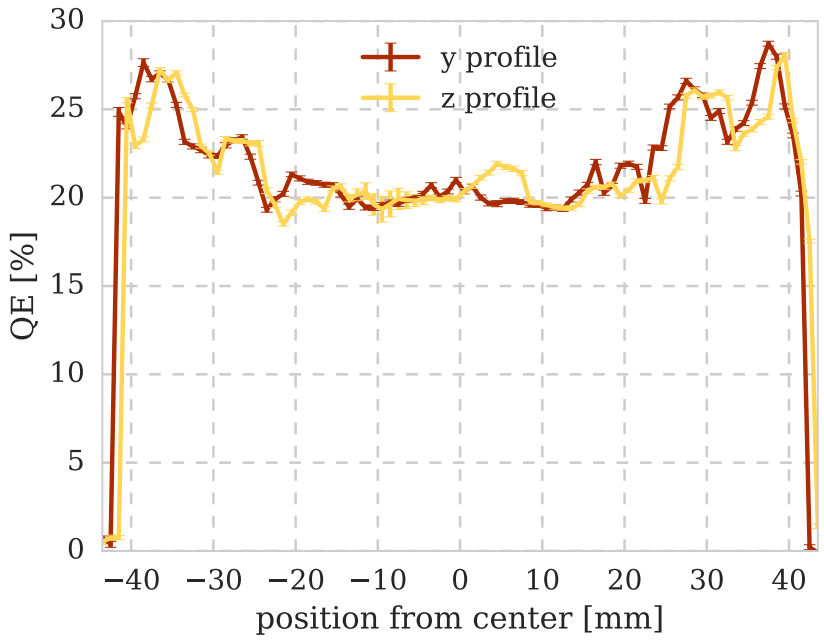

Figure 8.20: y- and z-profiles of the QE. Both profiles were sectioned through the PMT centre. Error bars were calculated with Gaussian error propagation, but are too small to be visible in most parts of the plot.

9 Summary and Outlook

The purpose of this thesis was to design, build and commission a test stand for high-precision quantum efficiency characteristic measurements of photomultiplier tubes that are to be implemented in the Multi-PMT digital optical module, a new optical sensor for IceCube-Gen2. This did not only include the design and setup of completely new hardware components and the programming of suitable software controls, the combination and coordination of a variety of different devices to form an efficient measurement setup, and the thorough testing of the involved hardware, but also a detailed understanding of the working principle of photomultiplier tubes and the physics of photocathodes.

The heart of the quantum efficiency test stand, the 3D scanner, which was designed and build as a part of this thesis for automated optical screening of PMTs, was successfully commissioned and proved itself a reliable and accurate piece of equipment. The ability to perform accurate remote 3D-positionings of the light output is an essential part of all the conducted measurements. The scanner and its control script are fully operational and ready to be used in further quantum efficiency investigations.

Other hardware components still need further optimisations. Some ideas were presented that could be realised in the future, for instance possible accuracy improvements of the rotation table which is used for angular PMT positioning, and light conducting alternatives to the current optical fibre and lens collimator solution, which appeared to be problematic for smaller wavelengths.

To commission the quantum efficiency test stand, but also to contribute first PMT characterisations to the mDOM project, we conducted three different measurements: The quantum efficiency ...

- ... as a function of the wavelength,
- ... as a function of the incident angle of the light,
- ... and as a function of the photocathode position.

The wavelength dependence measurements resulted in expected quantum efficiency curves, although they revealed a weak point of the test stand: Some currently installed optic components cut off small wavelengths, which made it impossible to get significant results in the affected spectral range. As mentioned above, some alterations are planned to fix this problem.

The results of the angular dependence measurement showed a good agreement with the theoretical predictions. Considerations concerning the large impact of reflection from the PMT's inner metal structures are confirmed in these investigations. A general problem with the test stand that occurred especially during these measurements is the presence of interfering signals that compromised the measurement process and decreased the significance of the results. A future improvement could be made by installing a sophisticated electromagnetic shielding for the Blackbox itself, which surrounds the test stand, to protect the highly sensitive PMTs from such interferences and to ensure unobstructed measurement procedures.

The test stand proved very suitable for the photocathode position dependence measurements, which could be conducted with high scan resolution and revealed PMT characteristics in great detail. The results indicate a pronounced impact of the PMT's inner metal

structures on the quantum efficiency which is consistent with the expectations and results of the other measurements.

Altogether, the quantum efficiency test stand will help to conduct PMT characterisation and testing measurements much more thoroughly and efficiently than it was before. This thesis provides the foundation and the knowledge base for future measurements, as well as for further improvements and extensions to the current test stand. One followup project will be a gyroscopic PMT mounting that will allow for the PMT to be rotated and tilted in all directions.

Further studies of PMT characteristics based upon this thesis could include photocathode thickness and homogeneity measurements to investigate the impact of these factors on the quantum efficiency. Such investigations could be conducted by means of ellipsometry, which is a procedure for optical investigations of thin layers by means of light polarisation. It is not clear though whether it is possible to include the rather complex experimental setup as a part of the QE test stand.

The experiments conducted in the scope of this thesis all had air as the PMT-surrounding medium, for obvious setup-constraining reasons. It would be an interesting aspect though to repeat the investigations in more IceCube-relevant media like water or ice. To realise this could be a major project of further QE test stand improvements.

10 Appendix

10.1 Refractive indices of the KCsSb photocathode

Table 10.1: Refractive indices of the BK7 glass window and the KCsSb photocathode for several wavelengths. Displayed are the real and imaginary components of the complex refractive indices $N = n + i\kappa$. n_2 has been calculated with the Sellmeier equation (6.5) with the coefficients taken from [27], the data for κ_2 has been also taken from [27] and interpolated. Both n_3 and κ_3 have been taken from [28] and also interpolated.

λ [nm]	BK7		KCsSb			λ [nm]	BK7		KCsSb	
	n_2	κ_2	n_3	κ_3			n_2	κ_2	n_3	κ_3
300	1.55	2.86E-006	1.14	0.16		510	1.52	9.00E-009	3.04	0.79
310	1.55	1.37E-006	1.18	0.29		520	1.52	8.23E-009	3.15	0.73
320	1.55	6.66E-007	1.23	0.43		530	1.52	7.51E-009	3.26	0.59
330	1.54	3.40E-007	1.30	0.61		540	1.52	7.03E-009	3.24	0.40
340	1.54	1.80E-007	1.39	0.74		550	1.52	7.03E-009	3.17	0.33
350	1.54	9.29E-008	1.49	0.82		560	1.52	7.54E-009	3.12	0.24
360	1.54	4.65E-008	1.61	0.87		570	1.52	8.35E-009	3.08	0.23
370	1.54	2.74E-008	1.75	1.08		580	1.52	9.25E-009	3.04	0.19
380	1.53	2.07E-008	1.92	1.26		590	1.52	1.01E-008	3.01	0.17
390	1.53	1.37E-008	2.10	1.45		600	1.52	1.08E-008	2.99	0.15
400	1.53	1.02E-008	2.25	1.52		610	1.52	1.14E-008	2.97	0.12
410	1.53	8.61E-009	2.38	1.62		620	1.52	1.19E-008	2.96	0.11
420	1.53	9.39E-009	2.54	1.67		630	1.52	1.23E-008	2.95	0.10
430	1.53	1.07E-008	2.65	1.67		640	1.51	1.26E-008	2.95	0.08
440	1.53	1.12E-008	2.70	1.62		650	1.51	1.27E-008	2.95	0.06
450	1.53	1.09E-008	2.81	1.54		660	1.51	1.26E-008	2.95	0.08
460	1.52	1.03E-008	2.93	1.42		670	1.51	1.23E-008	2.95	0.05
470	1.52	9.97E-009	3.00	1.22		680	1.51	1.16E-008	2.96	0.02
480	1.52	9.89E-009	3.01	1.05		690	1.51	1.05E-008	2.98	0.02
490	1.52	9.83E-009	2.99	0.88		700	1.51	8.93E-009	3.02	0.02
500	1.52	9.58E-009	3.00	0.85						

10.2 Further calculations on reflection and transmission in thin films

As explained in section 6.2.2, each traverse of light through the conductive layer (photocathode) of a PMT results in a factor of $e^{i\rho}$ in the reflection and transmission coefficients r_{CL} (6.13) and t_{CL} (6.14) with

$$\begin{aligned}\rho &= \frac{2\pi d}{\lambda} N_3 \cos(\theta_3) \\ &= \eta\,(u_3 + i v_3)\end{aligned}$$

where λ is the wavelengths of the incident light in vacuum, d is the thickness of the layer, and $\eta = \frac{2\pi d}{\lambda}$. Later we will see that it is useful to divide ρ in a real and imaginary part u_3 and v_3 as it is done above, where (following [21] pp. 628-632)[48]:

$$\begin{aligned}2u_3^2 &= n_3^2 - \kappa_3^2 - n_2^2 \sin^2(\theta_2) + \sqrt{\left(n_3^2 - \kappa_3^2 - n_2^2 \sin^2(\theta_2)\right)^2 + 4\kappa_3^2} \\ 2v_3^2 &= -\left(n_3^2 - \kappa_3^2 - n_2^2 \sin^2(\theta_2)\right) + \sqrt{\left(n_3^2 - \kappa_3^2 - n_2^2 \sin^2(\theta_2)\right)^2 + 4\kappa_3^2}\,.\end{aligned}$$

Each coefficient in r_{CL} and t_{CL} can now be expressed with its phase to $r_{ij} = p_{ij} e^{i\phi_{ij}}$ and $t_{ij} = q_{ij} e^{i\chi_{ij}}$. The exact expression of the ϕ_{ij} and χ_{ij} is not important at this point. For the reflectance R_{CL} one has with (6.13):

$$\begin{aligned}R_{\mathrm{CL}} = |r_{\mathrm{CL}}|^2 &= \frac{\left|p_{23} e^{i\phi_{23}} + p_{34} e^{i\phi_{34}} e^{2i\eta(u_3+iv_3)}\right|^2}{\left|1 + p_{23} e^{i\phi_{23}} p_{34} e^{i\phi_{34}} e^{2i\eta(u_3+iv_3)}\right|^2} = \frac{\left|p_{23} e^{i\phi_{23}} + p_{34} e^{-2\eta v_3} e^{i(\phi_{34}+2\eta u_3)}\right|^2}{\left|1 + p_{23} e^{i\phi_{23}} p_{34} e^{-2\eta v_3} e^{i(\phi_{34}+2\eta u_3)}\right|^2} \\ &= \frac{p_{23}^2 + p_{34}^2 e^{-4\eta v_3} + 2 p_{23} p_{34} e^{-2\eta v_3} \cos\left(\phi_{23} - \phi_{34} - 2\eta u_3\right)}{1 + p_{23}^2 p_{34}^2 e^{-4\eta v_3} + 2 p_{23} p_{34} e^{-2\eta v_3} \cos\left(\phi_{23} + \phi_{34} + 2\eta u_3\right)} \\ &= \frac{|r_{23}|^2 + \left|r_{34}\right|^2 e^{-4\eta v_3} + 2 p_{23} p_{34} e^{-2\eta v_3} \cos\left(\phi_{23} - \phi_{34} - 2\eta u_3\right)}{1 + |r_{23}|^2 \left|r_{34}\right|^2 e^{-4\eta v_3} + 2 p_{23} p_{34} e^{-2\eta v_3} \cos\left(\phi_{23} + \phi_{34} + 2\eta u_3\right)}\end{aligned} \tag{10.1}$$

with the relations $p_{ij}^2 = \left|r_{ij}\right|^2$ and $\left|e^{2i\eta(u_3+iv_3)}\right|^2 = e^{-4\eta v_3}$. Analogous for the transmittance T_{CL} with (6.14):

$$\begin{aligned}T_{\mathrm{CL}} &= \frac{n_4 \cos\theta_4}{n_2 \cos\theta_2} |t_{\mathrm{CL}}|^2 \\ &= \frac{n_4 \cos\theta_4}{n_2 \cos\theta_2} \frac{|t_{23}|^2 \left|t_{34}\right|^2 e^{2\eta v_3}}{1 + |r_{23}|^2 \left|r_{34}\right|^2 e^{-4\eta v_3} + 2 p_{23} p_{34} e^{-2\eta v_3} \cos\left(\phi_{23} + \phi_{34} + 2\eta u_3\right)}\end{aligned} \tag{10.2}$$

Note that either r_{CL} and t_{CL} as well as R_{CL} and T_{CL} hold for each polarisation of light separately.

The photocathode is a thin film[49]. On thin film scales, the light waves can be assumed to be monochromatic and coherent plane waves, so that the individual reflected waves that correspond to the components of $r_{\mathrm{CL}} = r + r' + ...$ interfere with one another, and the same is true for the transmitted waves, which is indicated by formulas (10.1) and (10.2) with the cosine interference terms. Whether the interference is constructive or destructive depends

[48] Note that here the relation $N = n + i\kappa$ is used, whereas [21] uses $N' = n(1 + i\kappa')$.

[49] For a definition of thin films see 'Optical functions of the photocathode' in section 6.2.2.

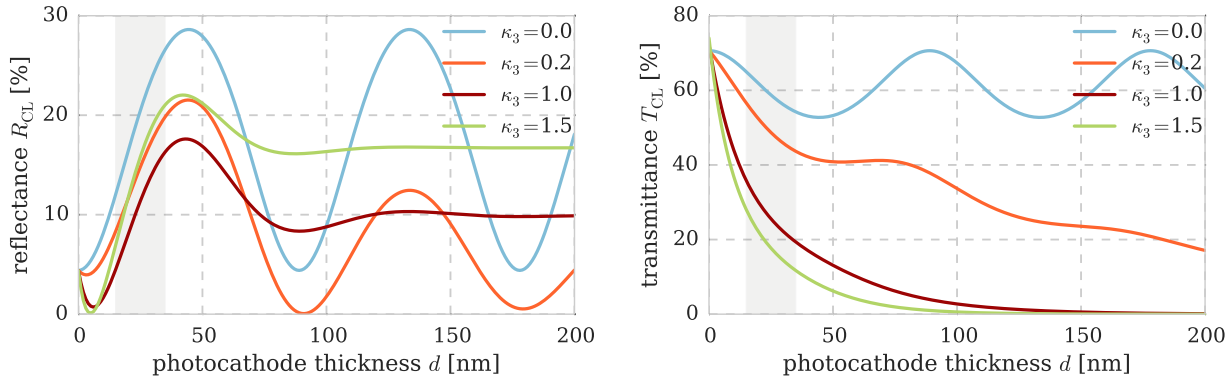

(a) (b)

Figure 10.1: Reflectance R_{CL} **(a)** and transmittance T_{CL} **(b)** of the photocathode plotted against the photocathode thickness d, assuming the following parametrisation: $n_2 = 1.53$, $n_3 = 2.25$, $\lambda = 400\,\text{nm}$, $\theta_2 = 0°$. The different colours indicate different values of the extinction coefficient κ_3. Realistic values for the thickness of the photocathode lie within the grey areas.

on the phase shift and therefore on ρ with the parameters d, λ, θ and N_3. To visualise these dependencies, the optical functions are plotted against d in figures 10.1a and 10.1b. Considering only the case without attenuation in the material (blue curves), it can be seen that the optical functions oscillate, with their maximum and minimum points corresponding to $\frac{m\lambda}{4n_3}$ with $m \epsilon \mathbb{N}$. For R_{CL}, the interference is constructive if m is odd, and destructive if m is even. For T_{CL}, it is the other way around as can easily be seen from the different exponents $e^{2i\rho}$ and $e^{i\rho}$ in the formulas for r_{CL} and t_{CL}, respectively. This periodicity would continue until the layer thickness reaches values where interference does no longer occur. However, the other curves represent more realistic cases with different degrees of absorption in the material. As can be seen, for $\kappa_3 \neq 0$ the reflectance eventually levels at a value that equals the reflectance at the very first bounding surface, so that $R_{CL} \sim R_{23}$, whereas the transmittance decreases exponentially with the increase of d. That means that the internal reflection as well as the transmission is negligible for thick layers with attenuation. This is not the case for the relatively thin photocathode though, whose dimensions are indicated by the grey areas in the plot.

One important takeaway of these plots is that a relatively small deviation in d would have quite an impact on the optical functions. Since the process of evaporating the photocathode onto the glass is not completely exact in reality, d is assumed to not be constant throughout the entire area. For the predictions however, a uniform value of $d = 20\,\text{nm}$ was set as suggested in reference [20]. The real thickness of the PMTs used in our measurements can easily deviate by several nm; unfortunately we are not able to measure it (yet). This should be kept in mind for the evaluation of the QE predictions in sections 6.2.3 and 6.2.4.

10.3 Code excerpts

```
50      # set fixed values and coordinates:
51      wavelength  = 470.0
52      offset      = PMT['radius_bulb'] - PMT['depth']
53      scan_radius = PMT['radius_cathode'] + 3
54      stepsize    = 1.0
55      stepref     = 5
56      x0          = 190.45
57      phd_pos     = (x0, 202., 205.)
58      dc_pos      = (x0, 202., 105.)
59      pmt_cen     = (x0, 68.5, 145.5)
60
61      # creating y- and z-coordinate arrays:
62      distance_i = (pmt_cen[1] - scan_radius, pmt_cen[2] - scan_radius)
63      distance_f = (pmt_cen[1] + scan_radius, pmt_cen[2] + scan_radius)
64      y_distances = np.arange(distance_i[0], distance_f[0], stepsize)
65      z_distances = np.arange(distance_i[1], distance_f[1], stepsize)
66
67      realwave = mnc.Go_wave(wavelength)
68      time.sleep(1)
69      Take_dc_ref()
70      # scanning...
71      for i, z in enumerate(z_distances):
72          if (i != 0) and (i % stepref == 0):
73              Take_dc_ref()
74          moc.Move_to_distance_1d(2, 0, z)
75          for j, y in enumerate(y_distances):
76              r = np.sqrt(abs(y-pmt_cen[1])**2 + abs(z-pmt_cen[2])**2)
77              if (r <= PMT['radius_cathode']):
78                  x_shift = abs(np.sqrt(PMT['radius_bulb']**2 - r**2) - PMT['radius_bulb']) - PMT['depth']
79              else:
80                  x_shift = 0
81              moc.Move_abs_distance_3d((x0 + x_shift, y, z))
82              pointx = moc.Get_distance(0, moc.Get_parameter(0, 1))
83              pointy = moc.Get_distance(1, moc.Get_parameter(1, 1))
84              pointz = moc.Get_distance(2, moc.Get_parameter(2, 1))
85              current = pic.Get_currents(num_pmt)[1]
86              time.sleep(1)
87              # writing to data file:
88              seconds = time.time() - starttime
89              with open(datafile, 'a') as d:
90                  d.write(str('%.2f' % seconds)    + '\t' + str('%.2f' % pointx)    + '\t' +
91                          str('%.2f' % pointy)     + '\t' + str('%.2f' % pointz)    + '\t' +
92                          str('%.5e' % current[0]) + '\t' + str('%.5e' % current[1]) + '\n')
93              print('point ' + str('%.2f' % pointx) + ', ' + str('%.2f' % pointy) + ', ' +
94                    str('%.2f' % pointz) + ' taken')
95
96      Take_dc_ref()
97      print('\nscan finished.')
```

Figure 10.2: Code excerpt of the position dependence scan routine from the QE test stand Python script. The routine coordinates all instruments necessary to perform the scan. The important variables are set in lines 51-59, including the wavelength and step size of the scan, the position of the PMT and photodiode in scanner coordinates, as well as information about the investigated PMT necessary to calculate the position map (see figure 8.15a). The actual scanning process is found in line 71-88. Methods controlling the scanner begin with `moc.`, the picoampere meter with `pic.` and the monochromator with `mnc.` Gathered data is written to a file in lines 89-94. The implementation of the function `Take_dc_ref()`, which performs a dark current and reference data recording, is not shown in this excerpt.

References

[1] M. Aartsen, et al. (IceCube Collaboration), *Neutrino Observatory: Instrumentation and Online Systems*, Preprint arXiv:1612.05093 (2016).

[2] M. Aartsen, et al. (IceCube Collaboration), *IceCube-Gen2: A Vision for the Future of Neutrino Astronomy in Antarctica*, Preprint arXiv:1412.5106 (2014).

[3] L. Classen, A. Kappes, *Multi-PMT optical modules for IceCube-Gen2*, Proceedings of Science ICRC2015 (2015) 1147.

[4] A. Kappes, *Multi-PMT Optical Module Designs for IceCube-Gen2*, EPJ Web Conf. 116 (2016) 01001.

[5] C. Grupen, Astroparticle physics, Springer-Verlag, Berlin Heidelberg, 2010.

[6] P. Higgs, *Broken Symmetries and the Masses of Gauge Bosons*, Phys. Rev. Lett. 13 (1964) 508–509. URL http://link.aps.org/doi/10.1103/PhysRevLett.13.508

[7] E. Fermi, *Versuch einer Theorie der beta-Strahlen*, Zeitschrift für Physik 88 (1934) 3–4. URL http://dx.doi.org/10.1007/BF01351864

[8] E. K. Akhmedov, A. Dighe, P. Lipari, A. Y. Smirnov, *Atmospheric neutrinos at Super-Kamiokande and parametric resonance in neutrino oscillations*, Nucl. Phys. B542 (1999) 3–30, Preprint arXiv:hep-ph/9808270.

[9] G. Drexlin, et al., *Current Direct Neutrino Mass Experiments*, Advances in High Energy Physics 2013 (2013) 293986, Preprint arXiv:1307.0101.

[10] L. Classen, *Prototyping a novel optical module for the IceCube-Gen2 neutrino telescope*, PhD thesis, Friedrich-Alexander-Universität Erlangen-Nürnberg, to be published.

[11] U. Katz, C. Spiering, *High-energy neutrino astrophysics: Status and perspectives*, Progress in Particle and Nuclear Physics 67 (3) (2012) 651–704. URL http://www.sciencedirect.com/science/article/pii/S0146641011001189

[12] P. A. Cerenkov, *Visible Radiation Produced by Electrons Moving in a Medium with Velocities Exceeding that of Light*, Phys. Rev. Lett. 52 (1937) 378–379. URL http://www.sciencedirect.com/science/article/pii/S0146641011001189

[13] R. C. Weast (Ed.), CRC Handbook of Chemistry and Physics, 62nd Edition, CRC Press Inc., Boca Raton, Florida, 1991.

[14] R. Abbasi, et al. (IceCube Collaboration), *The Design and Performance of IceCube DeepCore*, Astroparticle Physics 35 (2012) 615–624, Preprint arXiv:1109.6096.

[15] T. Waldemeier, *IceTop - Cosmic Ray Physics with IceCube*, Nucl. Inst. Meth. A588 (2008) 130–134, Preprint arXiv:0802.2540.

[16] M. Aartsen, et al. (IceCube Collaboration), *Observation of High-Energy Astrophysical Neutrinos in Three Years of IceCube Data*, Phys. Rev. Lett. 113 (2014) 101101, Preprint arXiv:1405.5303.

[17] M. G. Aartsen, et al. (IceCube PINGU Collaboration), *Letter of Intent: The Precision IceCube Next Generation Upgrade (PINGU)*, Preprint arXiv:1401.2046 (2014).

[18] Photomultiplier Tubes Basics and Applications, 3rd Edition, Hamamatsu Photonics K.K., 2007. URL https://www.hamamatsu.com/resources/pdf/etd/PMT_handbook_v3aE.pdf

[19] S.-O. Flyckt, C. Marmonier, Photomultiplier Tubes Principles and Applications, 2002. URL http://www2.pv.infn.it/~debari/doc/Flyckt_Marmonier.pdf

[20] D. Motta and S. Schönert, *Optical properties of bialkali photocathodes*, Nucl. Inst. Meth. A539 (2005) 217–235, Preprint arXiv:physics/0408075.

[21] M. Born, E. Wolf, Principles of Optics, 5th Edition, Pergamon Press, Oxford, 1975.

[22] O. S. Heavens, Optical Properties of Thin Solid Films, Dover Publications Inc., New York, 1991.

[23] D. Meschede, Optik, Licht und Laser, Vieweg und Teubner, Wiesbaden, 2008.

[24] B. E. A. Saleh, M. C. Teich, Fundamentals of Photonics, John Wiley & Sons Inc., 1991.

[25] M. H. Stockett, *Optical Properties of Thin Transparent Conducting Oxide Films on Glass for Photovoltaic Applications*, Honors thesis, Oberlin College USA (2006).

[26] S. Nevas, F. Manoocheri, E. Ikonen, *Determination of thin-film parameters from high accuracy measurements of spectral regular transmittance*, Metrologia 40 (2003) 200–203. URL http://iopscience.iop.org/0026-1394/40/1/346

[27] *Refractive index database*. URL http://refractiveindex.info

[28] C. Hugon, personal communication.

[29] H.Stöcker, Taschenbuch der Physik, 5th Edition, Verlag Harri Deutsch, 1975.

[30] PDL 800-B Picosecond Pulsed Diode Laser, PicoQuant GmbH (Mar 2012).

[31] Monochromator MSH-300 with variable slit, LOT-QuantumDesign GmbH. URL https://lot-qd.de/fileadmin/Mediapool/products/monochromators/en/LQ_Monochromator_MSH_300_with_variable_slit_en.pdf

[32] Photomultiplier Tube R12199, Hamamatsu Photonics K.K. (Feb 2017). URL https://www.hamamatsu.com/resources/pdf/etd/R12199_TPMH1356E.pdf

[33] O. Kalekin, B. Herold, J. Reubelt, *PMT characterisation for the KM3Net project*, Nucl. Inst. Meth. A639 (2011) 70–72.

[34] Detector Calibration Report 818-UV24-Jun-20163557, Newport Corporation, calibration sheet (Jun 2016).

[35] S. Schmiemann, personal communication.

[36] Photomultiplier Tubes R7600U Series, Hamamatsu Photonics K.K. (2016). URL https://www.hamamatsu.com/resources/pdf/etd/R7600U_TPMH1317E.pdf

[37] Photomultiplier 9320KFL datasheet, ET Enterprises Ltd (Aug 2015).

List of Figures

List of Tables

Acknowledgements

Ich danke:

Prof. Dr. Alexander Kappes für meinen Platz in dieser großartigen Arbeitsgruppe und die Chance, meine Masterarbeit zum IceCube-Gen2 Experiment beizutragen.

Prof. Dr. Christian Weinheimer für die großzügige Unterstützung und Förderung, sowie für die Zweitkorrektur dieser Arbeit.

Lew Classen für Alles.

Der Arbeitsgruppe Kappes für produktive Zusammenarbeit und für starken Tobak.

Der Arbeitsgruppe Weinheimer für zahlreiche unterhaltsame Kaffeepausen, für das großzügige Verleihen von Laborequipment und ungefähr 10 m Alufolie.

Christian Huhmann für die technische Realisierung meiner Messgeräte.

Georg Bourichter und der feinmechanischen Werkstatt für diverse schwarze Kisten und ne Menge Geduld.

Roland Berendes und der Elektronikwerkstatt für Spannung im Labor.

Florian Schepers für Licht im Dunkeln.

Michael Holl für Mathe.

Axel Buß für... Axel Buß.

Martin Antonio Unland Elorrieta fürs Korrekturlesen dieser Arbeit.

Meiner Familie, die immer an mich glaubt.

Und

Simon-Nis Peters für den Teppich, auf den ich gelegentlich zurückgeholt werden musste.

Declaration of Academic Integrity

I hereby confirm that this thesis “Setup and commissioning of a test stand for detailed investigations of quantum efficiency characteristics of photomultiplier tubes, and initial studies for IceCube-Gen2” is solely my own work and that I have used no sources or aids other than the ones stated. All passages in my thesis for which other sources, including electronic media, have been used, be it direct quotes or content references, have been acknowledged as such and the sources cited.

I agree to have my thesis checked in order to rule out potential similarities with other works and to have my thesis stored in a database for this purpose.

_____